LOW-TEMPERATURE SCANNING MAGNETIC PROBE MICROSCOPY
OF EXOTIC SUPERCONDUCTORS

A DISSERTATION
SUBMITTED TO THE DEPARTMENT OF APPLIED PHYSICS
AND THE COMMITTEE ON GRADUATE STUDIES
OF STANFORD UNIVERSITY
IN PARTIAL FULFILLMENT OF THE REQUIREMENTS
FOR THE DEGREE OF
DOCTOR OF PHILOSOPHY

Per G. Björnsson

September 2005

I certify that I have read this dissertation and that, in my opinion, it is fully adequate in scope and quality as a dissertation for the degree of Doctor of Philosophy.

_____

Kathryn A. Moler   Principal Adviser

I certify that I have read this dissertation and that, in my opinion, it is fully adequate in scope and quality as a dissertation for the degree of Doctor of Philosophy.

_____

Ian R. Fisher

I certify that I have read this dissertation and that, in my opinion, it is fully adequate in scope and quality as a dissertation for the degree of Doctor of Philosophy.

_____

Steven A. Kivelson

Approved for the University Committee on Graduate Studies.

Abstract

Scanning magnetic probe microscopy is one of the many scanning probe microscopy (SPM) techniques that have been developed in the last two decades. The basic idea of the technique is conceptually simple: a micro- or nano-scale magnetic sensor is rastered over a sample and measures the magnetic field locally, giving an image of the magnetic fields at the surface. This thesis details the construction of a scanning magnetic microscope which utilizes SQUID (Superconducting QUantum Interference Device) or Hall probe sensors in a dilution refrigerator, extending the temperature range for this measurement technique down to the millikelvin range; the development of the probes used in the microscope; and the measurements for which it has been used.

The primary experiment which I report is searching for signs of time reversal symmetry breaking in the unconventional superconductor strontium ruthenate (Sr_2RuO_4). There is strong published evidence that this material is a spin-triplet superconductor. In addition, there is experimental evidence from μSR (muon spin resonance) and small-angle neutron scattering experiments that the wavefunction is a two-component Ginzburg-Landau wavefunction which exhibits time reversal symmetry breaking (TRSB) properties.

A direct consequence of TRSB is that there should be spontaneously generated magnetic fields locally at sample edges. I have searched for this signature of TRSB in single-crystal samples of Sr_2RuO_4, including samples that have been patterned with an array of dimples in order to generate artificial edges which should enhance the effect. No signatures of TRSB have been found in these experiments. This contradicts theoretical estimates, and the discrepancy indicates that either Sr_2RuO_4 does not have TRSB properties, or the theoretical estimates are insufficient in that they do not take factors such as domain formation into account.

In a related experiment, I have studied the local susceptibility of the "3 K phase" of

Sr_2RuO_4. This is a phase of the material that contains inclusions of metallic Ru. The measurements reported in this thesis show that the diamagnetism of the inclusions is strongly enhanced at temperatures below the T_c of Ru, indicating that the inclusions are not homogeneously integrated into the surrounding superconducting material.

Acknowledgments

The work I report in this thesis would never have been possible without the support of a great number of people who have supported me intellectually as well as personally throughout the journey.

First, I would like to thank my adviser, Kathryn (Kam) Moler. She has always a helpful and friendly guide and inspiration. Her combination of expertise and enthusiasm makes her a great role model as a scientist.

Throughout my time at Stanford I have worked with several outside collaborators, who have all contributed greatly to my work. John Kirtley has build a large part of the foundation on which my scanning SQUID and Hall probe microscopy work is built, and he has also been very helpful in understanding the ins and outs of the early SQUIDs. Martin Huber has worked with us on a new generation of scanning SQUIDs and has helped us understand SQUID performance and noise issues, worked with us on implementing a new SQUID readout system and has always been very helpful and a very fun person to work with. Yoshi Maeno has not only supplied us with the samples for my main set of experiments, but has also been a great source of experimental ideas and understanding of the various issues related to the intricacies of Sr_2RuO_4.

I would like to thank my reading committee, consiting of Kam, Ian Fisher and Steve Kivelson, for their suggestions and help with this thesis, and my two other defense committe members, Mac Beasley and Stig Hagström, for their time, interest and interesting questions.

I was part of the first generation of Moler group students, sharing that status with Janice Wynn Guikema, Brian Gardner and Eric Straver. Working together with them was a great experience, and without their help in everything from putting on the sliding seal on the dilution fridge sometime after midnight to discussing the intricacies of SQUIDs and superconductors. Of course, occasionally we just shut down the lab and

all went camping together too.

Luckily, Kam has good taste in students, so the great atmosphere in the group didn't end with the more recent additions. Working with Clifford Hicks, Hendrik Bluhm, Nick Koshnick, Rafael Dinner, Zhifeng Deng and Lan Luan has been a great pleasure. The friendly and collaborative atmosphere in the group doesn't end with the graduate students either; the post-docs in the group – Mark Topinka, Jenny Hoffman and Ophir Auslaender – have, in addition to being great people to work with, brought in an outside perspective to the group and have not hesitated to get their hands dirty in helping out wherever necessary.

Looking beyond the walls of the Moler lab, I also owe a lot to the rest of the McCullough basement dweller community. The students in the KGB and DGG labs, and Marcus lab before the DGG lab existed never-ending resource of hands, ideas, tools and knowledge. I would especially like to mention the generous sould who helped me figure out how to keep the beast that an Oxford fridge can be running: Nadya Mason, Sara Cronenwett and Josh Folk were excellent sources of low-temperature knowledge early on, and when they moved on their mantle has been picked up mainly by Myles Steiner and Ron Potok.

The work I have done has also depended heavily on the technical and adminstrative skills of many others. Mike Hennessy was instrumental in the design and deployment of the dilution fridge peripherals, welding vacuum lines, building tables and making concrete blocks; Karlheinz Merkle and his co-workers at the Physics machine shop always managed to understand my sometimes cryptic drawings and making my urgently needed microscope pieces and other items quickly; Mark Gibson often goes well beyond the call of duty to help out when help is needed; our admininstrative assistants, Judy Clark, Cyndi Mata and Mary Williams have helped keep me and the rest of the group running, and Paula Perron is always on top of the academic administrative issues.

On a more personal level, my time here at Stanford has been dramatically enriched by all the new friends I have met, and I have had a lot of fun with clubs such as the Scandinavians at Stanford.

I would also like to thank my family for their never-ending love and encouragement.

My parents have always supported my endeavors with great enthusiasm, and I can't see getting where I am without their support. Finally, during the last few years, my girlfriend Anna has been my pillar of loving, trusting support and joy outside the lab. Thank you!

<div align="right">

Per Bjornsson

Stanford University

September 2005

</div>

x

Contents

List of Tables

List of Figures

Chapter 1

Introduction

This thesis is divided into three major sections. The first, in Chapter 2, covers the technical design and construction of a scanning microscope in a dilution refrigerator. The second part, comprised of Chapters 3 and 4 describes the function of and development work done on two different kinds of magnetic sensors, SQUID susceptometers and Hall probes, for use in the microscope. Finally, the remaining chapters describe experiments performed, with the focal point being the magnetic imaging of the unconventional superconductor strontium ruthenate (Sr_2RuO_4) in search of signatures of time-reversal symmetry breaking.

Before embarking on the main body of work, in this introductory chapter I will present a general overview of and motivation for the work, putting it in the context of earlier scanning microscopy work. I will give short overview of different magnetic imaging techniques and attempt to explain under what circumstances they are useful, and will also attempt to briefly discuss why one would be interested in magnetic imaging in the first place.

1.1   Scanning microscopy

Since the invention of the scanning tunneling microscope (STM) by Binnig and Rohrer in the early 1980s [Binnig and Rohrer, 1982], many types of scanning probe microscopes have been developed. The common feature of this class of microscopes is that they measure a physical property locally at a surface using a microscopic sensor, and create an image by moving the sensor over a point grid on the surface.

Perhaps the best-known scanning microscopy techniques are STM and atomic force microscopy (AFM), invented by Binnig, Quate and Gerber in 1986 [Binnig *et al.*, 1986]. Both can be used to create a topographic image of a surface; the STM works by scanning an atomically sharp metallic tip above the surface, biasing it at a small voltage and registering the tunnel current between the tip and the sample, while the AFM detects the deflection of a cantilever with a sharp tip by atomic forces when essentially either dragging the tip along the surface or tapping the cantilever on the surface.

By using a magnetic field sensor instead of (or in addition to) a topography sensor, one can map the magnetic fields at the surface of the sample. This is the basis for scanning magnetic probe microscopy. One way to do this is to coat an AFM cantilever with a ferromagnetic material. This makes the cantilever sensitive to long-range magnetic forces from the sample, in addition to the short-range atomic forces. Because of the different range characteristics, the atomic forces will dominate the collected images at low scan heights, while the magnetic forces will dominate at larger heights. Another class of scanning magnetic probe microscope uses a small magnetic field sensor which is scanned over the surface; this is the type of microscope that has been used for the work described in this thesis.

1.2   Applications of Magnetic Imaging

There are several situation in which magnetic imaging is interesting. First, and probably most obvious, is imaging magnetic materials: high-resolution imaging can be used to study phenomena such as domain structure in ferromagnets. Another set of materials with a strong magnetic signature is superconductors, where magnetic vortices carry important information about the characteristics of the superconductivity, and where local susceptibility measurements could be used to find trace diamagnetism indicating local superconductivity in novel materials.

Perhaps less obvious is the possibility of using magnetic measurements as low-invasiveness current probes, especially for mesoscopic systems. The idea is that it is impossible to measure spontaneous currents in isolated systems using transport techniques since the system would no longer be isolated with the transport measurement leads attached. This type of currents may instead be probed by locally measuring the magnetic field generated by the currents.

1.3   Overview of Magnetic Imaging Techniques

Studying the spatial variation of magnetic fields is a field with a relatively long history and many different available experimental techniques, including bitter decoration, scanning probe microscopy techniques, magneto-optics and Lorentz microscopy.

Since there are many different magnetic imaging techniques available, it is essential to start by carefully considering what imaging technique is most suitable to the issue at hand. Below I will discuss the trade-offs inherent to the various imaging techniques.

A few of the main issue to take into account when choosing imaging techniques are:

- Spatial resolution

- Magnetic field sensitivity

- Possibility of quantitative measurements

- Possibility of measuring other parameters than magnetic field (such as magnetic susceptibility)

- Measurement speed

- Invasiveness

The different techniques all have specific strengths and weaknesses. In the following I will highlight some of the features of the different techniques.

1.3.1   Scanning SQUID Microscopy

Superconducting QUantum Interference Devices, SQUIDs, are magnetic sensors which consist of a superconducting loop with two Josephson junctions. Since SQUIDs are one of the main sensors I have been using, there is a more detailed description of how SQUIDs work and of the particulars of the SQUID sensors which I have used in Chap. 3.

SQUIDs measure the magnetic flux ($\int B \cdot dA$) threading the loop, no matter how it is distributed. They are insensitive to other environmental factors, so it is simple to interpret a SQUID measurement and to quantify the measurement results. Their flux sensitivity is unrivaled by other sensors, with flux noise levels as low as 0.3 $\mu\Phi_0/\sqrt{\text{Hz}}$ [Ketchen *et al.*, 1991], and if the sensor is large this gives them excellent magnetic field sensitivity. However, the design is complex enough that it is difficult to make very small

SQUIDs; the smallest sensors I have used have had a pickup area shaped like a circle with a 4 μm radius [Huber *et al.*]. Smaller designs have been reported by Hasselbach *et al.* [2000]; however, these devices are simpler designs with higher readout noise, and because of the sensor characteristics they need a more complex readout scheme than traditional SQUIDs.

The fundamental limit on the size of a SQUID is set by the magnetic penetration depth (λ) of the superconductor material it is made of. When the line width approaches λ, the SQUID loses sensitivity [Tesche and Clarke, 1977]. A typical value for lambda in thin-film Nb (which is the most commonly used material for superconducting electronics) is 90 nm [Hypres, Inc., As available online in June 2005]. This likely limits the effective size of SQUID pickup loops to at least several hundred nm. Using other materials such as aluminum could allow smaller SQUIDs to be made; however, aluminum has a T_c of only 1 K and is thus in many cases impractical to use as in a SQUID sensor.

The environmental limitations for SQUIDs are that they only work when they are superconducting, and they only work sanely in low magnetic field environments since flux trapping and motion in the superconductor will change the SQUID properties. In some cases it is possible to separate the sample and the sensor - either just by making the thermal link very bad or by actually introducing a window between the sample and the sensor - but especially the latter solution increases the sensor-sample distance and thus limits the possible spatial resolution and sensitivity to small features.

Given the complexity of fabricating a high-quality SQUID in the first place, it adds very little difficulty to use relatively complicated SQUID shapes, and it is also reasonable to put additional functionality on the sensor chip. In the SQUIDs used for the measurements reported in this thesis, the pickup loops are surrounded by superconducting current lines which act as field coils and allow local measurements of magnetic susceptibility in addition to magnetometry.

Scanning SQUID microscopy is a fairly non-invasive technique. The SQUID does have some back-action on the sample caused by the currents in the SQUID, but this is generally a small effect. In terms of sample preparation, the demands on the sample are also quite low: as with all scanning probe microscopy a relatively flat surface is necessary, but since the spatial resolution is limited and the technique is not particularly surface-sensitive the demands are lower than for other types of scanning probe microscopy.

1.3.2 Scanning Hall Probe Microscopy

Hall probes are magnetic field sensors based on the Hall effect: when a current is run through a conductor in a magnetic field, a voltage is induced perpendicular to the current direction. This voltage is proportional to the applied field, so Hall probes are very easy to use as direct and quantitative magnetic field sensors. This is the second type of sensor which I have used for experiments; the specifics are described in detail in Chap. 4.

Hall probes are typically fabricated on a semiconductor 2DEG structure. Since the design is simpler than that of a SQUID, it is technically easier to make a smaller sensor. Fundamental size limits may be related to quenching of the Hall effect deep in the ballistic transport regime; however, for typical Hall probe fabrication parameters this should not affect the performance until well into the the sub-100 nm range.

The magnetic field sensitivity of Hall probes is in general significantly worse than that of SQUIDs, with a typical white noise floor on the order of 1 mG/$\sqrt{\text{Hz}}$ and a significant $1/f$ contribution; a discussion of Hall probe noise can be found in Chap. 4. Unlike SQUIDs, Hall probes can be used in background fields up to several T; the fundamental limits to where a Hall probe is useful is set by when the quantum Hall regime is entered.

While Hall probes mainly measure magnetic fields, they may also measure some stray signals. In particular, 2DEG Hall probes tend to have piezoresistive effects which makes them sensitive to pressure. While SQUIDs can often be scanned while touching the surface, there is a risk of spurious topography-related signals if this is done with a Hall probe.

1.3.3 Magnetic Force Microscopy

A third type of magnetic scanning probe microscopy is magnetic force microscopy, MFM. In this case an AFM tip coated with a magnetic material is used. This makes the tip sensitive to magnetic forces from the sample in addition to the short-range atomic force probed by AFM.

MFM offers significantly better spatial resolution than SQUIDs or Hall probes, with a resolution around 25 nm demonstrated, and potential for getting down to around 10 nm [Straver, 2004].

The magnetic force sensed by the tip is proportional to the magnetic field gradient, not the field itself. In the most common measurement modes, the measured signal is actually proportional to the force gradient, and thus the second derivative of the magnetic field. This makes it more difficult to interpret MFM images quantitatively than SQUID or Hall probe images. It is also difficult to directly compare the sensitivity to the direct field measurements; MFM sensitivity is more commonly quoted in terms of magnetic forces. Force sensitivity in the few-aN (10^{-18} N) range have been demonstrated by [Stowe *et al.*, 1997]. In the same article the authors note that the magnetic force from a single spin on a 500 Å radius cobalt particle (which could be the magnetic material on an MFM tip) at a height of 130 Åis approximately 100 aN, well within the detection range of the cantilever.

Since MFM is sensitive to field gradients and not the magnetic field itself, it is possible to measure in any background field that can be applied in the instrument.

1.3.4   Spin-Polarized Scanning Tunneling Microscopy

A different approach to performing magnetic measurements using scanning probe microscopy is spin-polarized STM, in which a magnetized tip is used in an STM [Johnson and Clarke, 1990]. This allows the measurement to give information about the local spin polarization of the sample. The potential spatial resolution for this measurement is excellent as this is an STM measurement, but it measures something quite different from the other SPM techniques discussed: instead of measuring the magnetic field at the sample, it measures the polarization properties of the sample. In some cases this may be exactly the property of interest (this may e.g. be very relevant for studying ferromagnetic domains), in other cases it is not.

1.3.5   Magneto-Optical Imaging

The magneto-optical (MO) Faraday effect can be used to create magnetic contrast from a sample by covering the sample with a thin MO-active film; currently the most common material used is a garnet film. Polarized light is shone on the sample through the film onto the sample. The polarization of the light is rotated by the MO film, with the rotation angle proportional to the magnetic field at the film, and using crossed polarizers the rotation angle can be detected. This technique can give quantitative

information about the magnetic field at the surface of a sample. An overview of the technique is given by [Habermeier, 2004].

While fast imaging of individual vortices in superconductors has been demonstrated using the technique [Goa *et al.*, 2001], it suffers from the need to compromise between spatial resolution and magnetic sensitivity: a thicker MO film gives a larger rotation of the polarization and thus a larger signal, but the spatial resolution is limited by the thickness of the film. However, the optical detection method can be very fast; video-rate or faster imaging is possible.

1.3.6 Lorentz microscopy

Because of the Lorentz force, electron beams are deflected by magnetic fields. This effect can be used to achieve magnetic contrast in a transmission electron microscope (TEM): the technique is known as Lorentz microscopy. This technique has been applied to real-time imaging of vortex motion using a custom-built 1 MeV TEM by Tonomura et al. at Hitachi [Tonomura, 1995].

Unlike scanning probe microscopy techniques, Lorentz microscopy probes the magnetic fields penetrating the bulk material instead of the field at the surface.

One of the major features of this technique is that it makes it possible to image vortices at video frame rates, collecting tens of images per second. However, this capability comes at a cost in sample preparation: The sample must be thinned to the extent that it is electron transparent. This typically means polishing a through-hole in a sample and studying the thin area close to the edge of the hole.

The magnetic contrast is achieved when the TEM is defocused somewhat from the sample. While this means that the ultimate spatial resolution for studying magnetic fields is lower than when imaging the physical sample structure, it allows for correlating e.g. defects in the sample with the behavior of vortices. This has been used by Tonomura et al. to study vortex motion in a high-T_c superconductor sample which had been ion beam irradiated in order to introduce columnar defects [Tonomura *et al.*, 2001].

1.3.7 Bitter Decoration

Bitter decoration involves depositing ferromagnetic or superconducting particles on the sample to form patterns along magnetic field lines. The pattern is then imaged

using optical microscopy or, for higher resolution, SEM. The method has been used to study e.g. magnetic flux penetration in superconductors since the 1950s [Schawlow, 1956]. For static magnetic fields, sub-μm spatial resolution is possible using small particles; however, the relatively complicated two-step process makes studying dynamics impossible.

1.3.8   Summary

Clearly all the different magnetic imaging techniques have different strengths and weaknesses; which one is most suitable depends greatly on the subject of interest. There are a great number of situations where the flexibility of being able to use a SQUID sensor when it is needed for magnetic field sensitivity or the possibility of susceptibility measurements is needed, or a Hall probe when higher spatial resolution is needed, is of great value. This flexibility is available using the scanning microscope presented in this thesis, which is easily adapted to both types of sensors.

Chapter 2

The Scanning Magnetic Probe Microscope

The experiments described in this thesis have been made possible by the construction of a scanning magnetic probe microscope in a dilution refrigerator, which allows sensitive local magnetic measurements in a temperature regime where such measurements have not previously been possible. In this chapter, I describe the design of the microscope and the technical considerations that have weighed in on the design.

I have described this microscope in its first iteration in an earlier paper [Björnsson *et al.*, 2001], and have described some of the later improvements in the conference proceedings for the LT23 conference [Björnsson *et al.*, 2003].

2.1 Microscope Design

2.1.1 A Scanning Chip-Sensor Microscope

The microscope is designed as a scanning chip-sensor microscope, meaning that it is built for using sensors fabricated on top of a chip. The sensors used are SQUIDs and Hall probes. The general trade-offs between the different sensor types was discussed in the introductory chapter, and details regarding the performance of the SQUIDs are discussed in Chapter 3 and a similar treatment of the Hall probes is found in Chapter 4. In principle some other sensor placed in the corner of a chip could also be used with this microscope, either a different magnetic field sensor or a sensor for some other physical
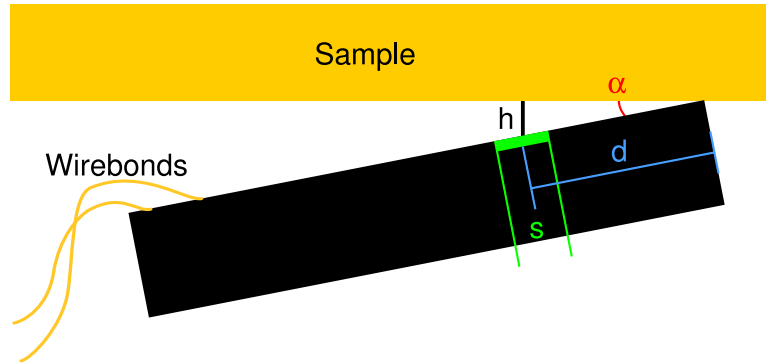
Figure 2.1: The sensor in a scanning chip-sensor microscope is aligned at a shallow angle with respect to the sample in order to minimize the sensor height. The spatial resolution of the microscope is determined by both the sensor active area size (s) and the height (h). Since wirebonds can be the limiting factor for the probe angle, it is important that the probe is designed with the wirebonds as far back as possible on the probe chip.

quantity.

Since the sensitive area is on top of a chip, the chip must be scanned at a shallow angle over the surface in order to get the sensor as close as possible to the sample. This setup is illustrated in Fig. 2.1. Getting the sample close to the surface is important since the effective resolution is determined both by the size of the probe active area and by the height of the probe above the surface. Scanning the probe at a small angle is better than attempting to align the probe flat just above the surface, since it gives a determined touchdown point and perfectly flat alignment is not actually practically possible between two macroscopic surfaces. The sensor chip is also connected to the readout apparatus with wirebonds, which often limit the possible scan angle; when using a small sample (or working close to the edge of a sample) the probe can be aligned in such a way that the wirebond connections are outside the sample in order to achieve a smaller alignment angle.

Typically an alignment angle of $1° - 2°$ is possible; if the wirebonds can be kept outside the sample an alignment angle as shallow as $0.5°$ is possible.
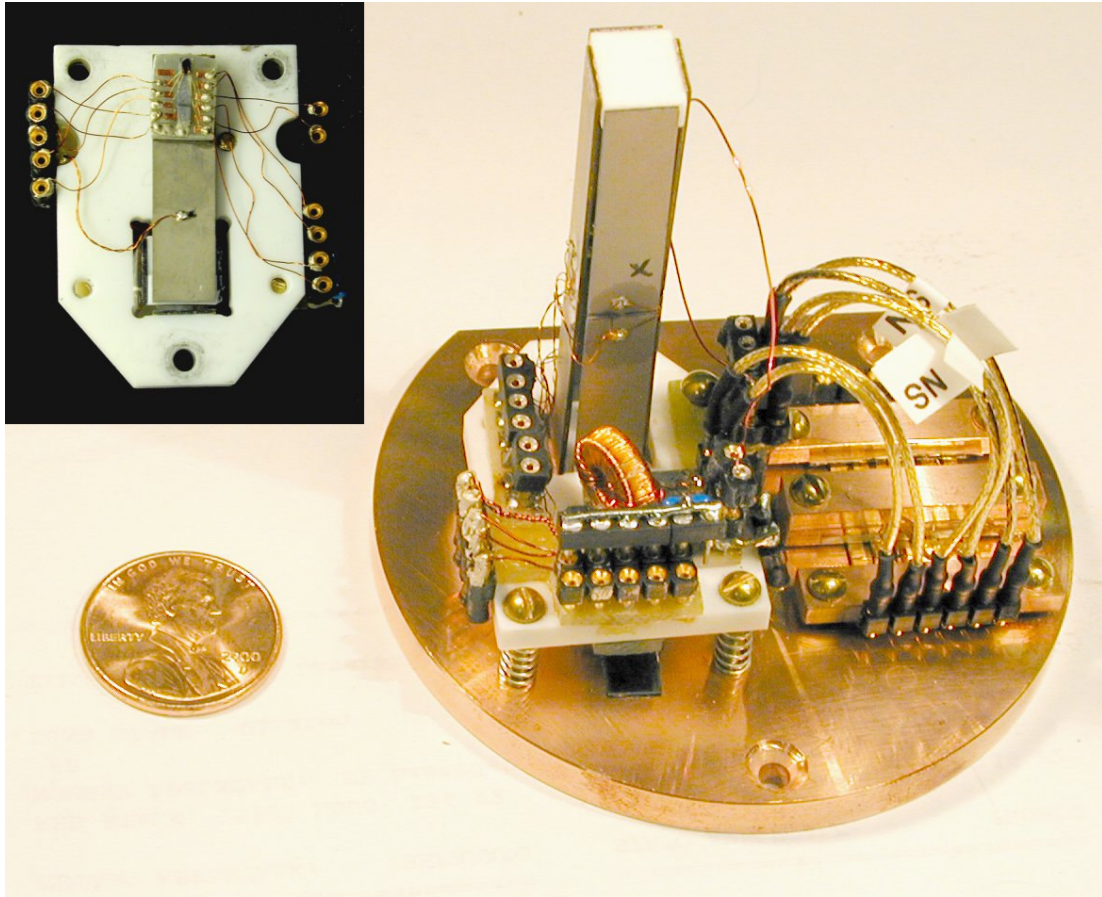
Figure 2.2: Photo of the scanning microscope mounted on the copper baseplate. The sample is mounted directly on the baseplate. Wiring is heatsunk either using the sapphire stripline heatsink on the right-hand-side of the baseplate, or by wrapping around copper bobbins such as the one visible in the back of the figure. Inset: Bottom view of the scanner with the probe mount mounted on the Z axis bender.
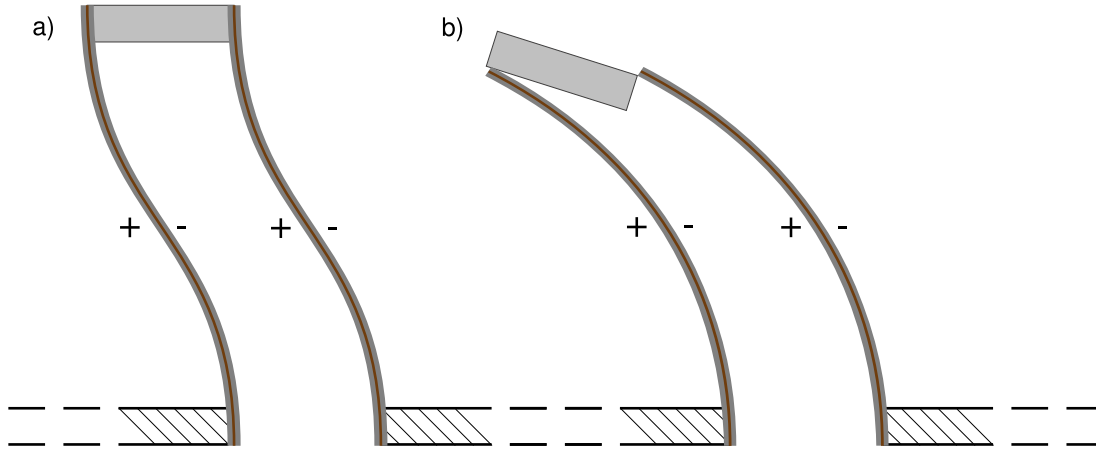
Figure 2.3: The bimorphs used bend in an S shape in order to allow for parallel uniaxial motion of the scan head relative to the base. a) Illustration of the scan stage movement (the range of motion is greatly exaggerated for clarity). (b) Ordinary "cantilever" bimorphs are not suitable for this type of scanner, since they would not allow a square connection with two parallel benders to move.

2.1.2   The Scanner

The scanner, depicted in Figure 2.2, is designed to provide a large scan range at low temperatures, while still being compact and providing precise control over the positioning. These objectives are achieved by using pairs of piezoelectric bimorphs which bend in an S shape for the movement in the scan plane, and a separate bimorph for adjusting the height. The basic S-bender scanner design was developed by Stuart Fields and coworkers [Siegel *et al.*, 1995].

The body elements of the scanner are made of MACOR, a machinable ceramic manufactured by Corning Inc. The thermal contraction of the MACOR approximately matches that of the piezo elements, and thus the stresses on the structure are small enough that the bimorphs can be fastened with a cyanoacrylate-based adhesive (super glue).

The scanner is mounted on a baseplate of OFHC copper, which is bolted directly onto the bottom of the mixing chamber of the dilution refrigerator for thermal contact. The sample is mounted directly on the copper baseplate.

The piezo bimorphs used for the scanner bend in an S shape, as shown in Fig. 2.3.
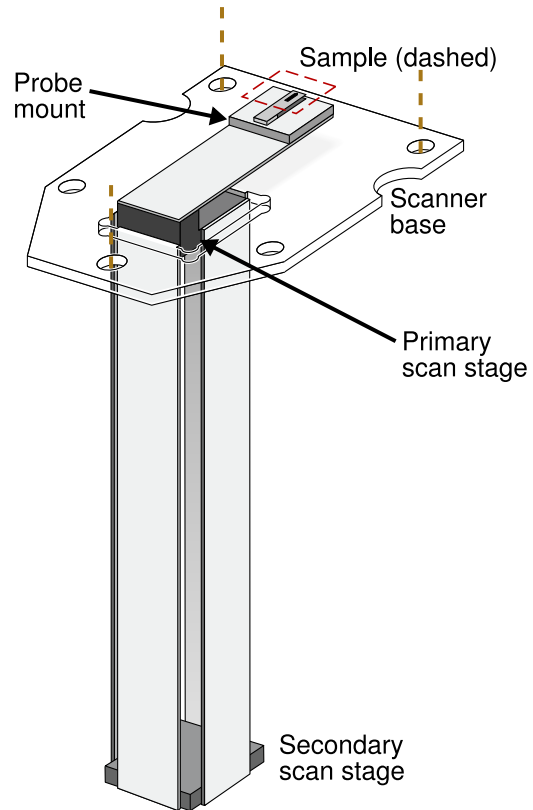
Figure 2.4: Sketch of the scanner. One pair of 2" long S-bender piezoelectric bimorphs connect the scanner base to the secondary scan stage and provide motion in the Y direction; a second pair connect the secondary and primary scan stages provide the X axis motion. A standard 1" cantilever bimorph provides the Z axis motion; the probe mount is attached at the end of this bimorph. The scanner is mounted using three spring-loaded screws to a copper baseplate.

This can be accomplished using ordinary cantilever bimorphs, but segmenting the electrodes in two pieces (typically by simply filing off a section of the electrodes at the center of the bender) and applying opposite voltages on the top and bottom segments of the piezo. More recently some manufacturers of piezo bimorphs have started manufacturing S-benders by poling the piezoelectric material in the two halves of the bender in opposite directions.

The scanner, illustrated in Fig. 2.4 is constructed using two pairs of S-bender bimorphs. The first (Y) connects the scanner base to the secondary stage, and the second pair (X) connects the secondary stage to the primary stage. A cantilever bimorph (Z) is mounted on the primary stage to provide height adjustment, and the sensor is mounted at the end of this bimorph.

The S-bender scanner design intrinsically compensates for thermal contraction of the piezos since the X and Y bimorph pairs are nominally identical; contraction of the pair connected between the main scanner base and the secondary scan stage will decrease the distance between the probe and the sample, while contraction of the bender pair connecting the secondary and primary scan stages will increase that distance equally. Thus any movement of the scanner because of thermal effects will mainly be caused by the MACOR plates and the three mounting screws. The effect of this thermal contraction is small, with the total contraction estimated to be about 25 μm, and consistent enough between cooldowns that the Z adjustment range of around 25 μm at low temperatures is large enough that the touchdown point consistently ends up well within the piezo adjustment range after room temperature adjustment of the touchdown point. This has allowed us to avoid any kind of low-temperature coarse approach method, vastly simplifying the design.

While there is thermal compensation of the height, there is no such compensation of motion in the X-Y plane, which may be caused by thermal contraction of the Z bender. In addition, alignment of the sample with the sensor is done simply by moving the sample around before fixing it in place with silver paint; typically a small dot of thermal grease is used to hold the sample in place temporarily during the alignment procedure. Because of these two significant limits on alignment accuracy, the scanner is mainly useful for samples which do not demand precise alignment of the magnetic probe with any particular point on the sample. Empirically we have found that the interesting area should preferably be several hundred μm on a side in order to be easy

to align to at room temperature.

Since the flexibility of the scanner itself allowed us to avoid the complexity of any low-temperature coarse motion, the scanner is mounted to the copper baseplate with three screws surrounded by BeCu springs. This design allows for simple adjustment of the height and the angle of the SQUID with respect to the sample, which is mounted directly on the copper baseplate using silver paint as an adhesive in order to maximize the thermal contact between the mixing chamber and the sample.

2.1.3   Sensor Mounting and Height Detection

In addition to being able to align the sensor with the sample, in order to scan the sensor close to the surface it is essential to be able to determine when the SQUID is touching the sample surface. In this microscope we have used a capacitive method of determining when the sensor tip is touching the sample.

The sensor is mounted on a metal foil cantilever which in turn is mounted above a Cu ground plane on a piece of circuit board, using a glass spacer (cut from a thin-grade microscope coverslip) at the rear end of the cantilever. The capacitance depends on the distance between the foil cantilever and the ground plane; modeling this as a parallel-plate capacitor, the capacitance is inversely proportional to this distance. Thus we can measure when the tip of the sensor touches the sample since the capacitor is compressed. Alternatively, when scanning with the sensor touching the sample lightly, the capacitance measurement gives a rough topographic map of the sample.

The noise level of the capacitance measurement is equivalent to movements of approximately 5 nm rms, and this sets the detection limit for which topographic features can be detected while scanning in touching mode. However, when accurate detection of the touchdown point is required other factors may be of importance, such as the type of interaction between the tip of the sensor and the sample; e.g. a repulsive interaction may smear out the touchdown point in the plot, while an attractive interaction may cause the sensor to snap onto the surface.

The smallest possible sensor height is reached by scanning the sensor with the tip touching the surface. This is not possible in all cases: some samples and/or sensors are not robust enough for this (e.g. Hall probes are quite fragile); there may be a concern that the sensor cannot be cooled to the same temperature as the sample and heating must be avoided; or the sensor might produce spurious signals from touching
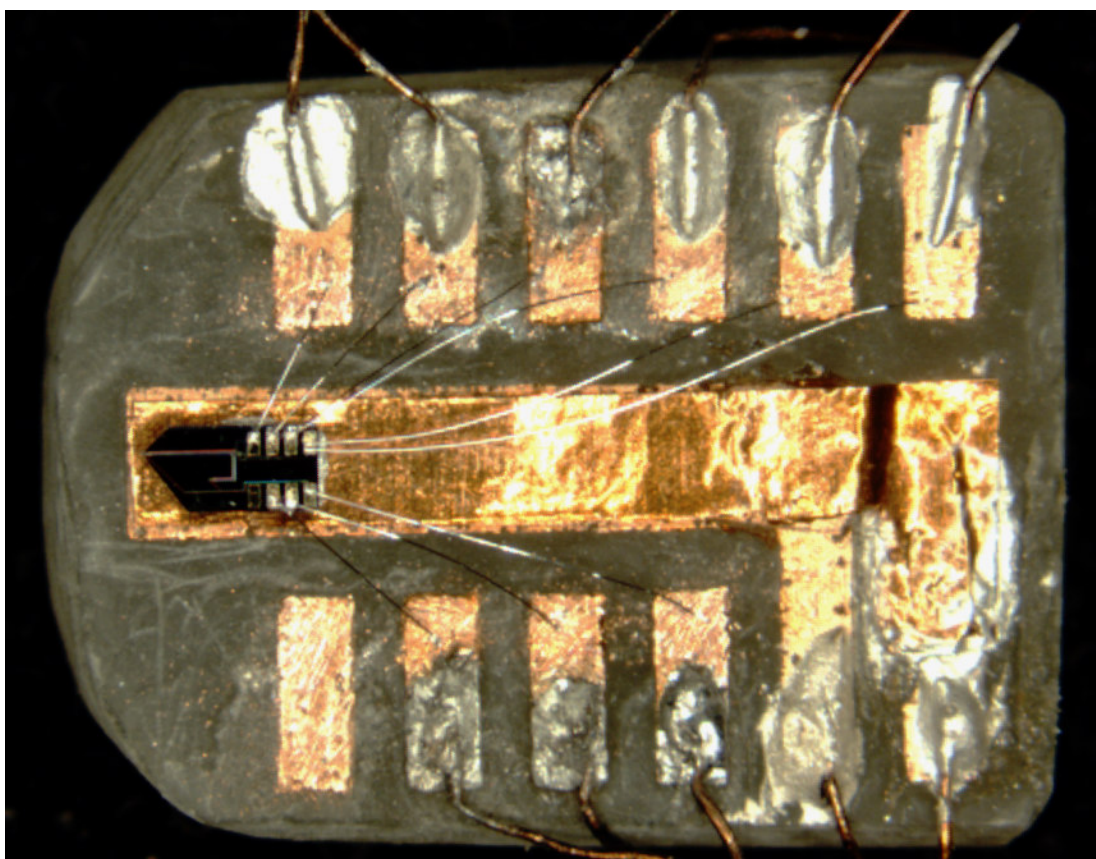
Figure 2.5: Photo of a mount with a SQUID; similar mounts are used for Hall probes.

the surface (in particular, Hall probes are typically somewhat piezoresistive, and this effect can cause a local signal that is difficult to separate from a magnetic signal). In this case, the sensor can be scanned in a plane above the sample, which is fitted by doing touchdown measurements at the corners of the scan area. The height achieved in this non-touching mode depends on how precisely the touchdown can be detected and the smoothness of the surface; typically a height of less than 100 nm more than the touching mode should be possible. The limit to touchdown detection is ideally the noise level in the capacitance measurement. However, if there are interactions between the probe and the sample, the probe may snap into the sample from some distance: in order to achieve separation, the probe must be kept at a larger distance than this. The snap-in also makes it more difficult to determine the exact touchdown point.

The metal foil used must be flexible enough that it allows the probe to deflect without applying large forces at the tip of the probe, since hitting the surface too hard might damage either the probe or the sample. The flexibility is determined by the foil thickness and the elasticity of the foil material. We have found that in most cases, if thin grades of metal foil are used (with a typical thickness of less than 25 μm), the stiffness of the foil cantilever is smaller than that of the wirebonds between the mount and the probe. Originally we used thin Al foil for the mounts; however, since Al is superconducting below 1 K it is not suitable for use in a dilution refrigerator, as it might disturb the magnetic fields and also has very low thermal conductivity when it is superconducting. We anticipate that in some situations the probe is in fact cooled mainly though the foil cantilever; this is especially likely if it is necessary to use superconducting aluminum wirebonds, which have better adhesion properties than gold wirebonds for some pad materials. In that case, it is of course of utmost importance that the cantilever itself has high thermal conductivity. The obvious candidate material from a thermal point of view is high-purity copper; however, copper is very easy to deform plastically, leaving the cantilever crooked. Thin brass foil is a much easier material to work with and appears to be a reasonable compromise.

2.1.4 Tunneling for Surface Detection and Topography Measurements

We have found that with the smallest Hall probes that we have made, where the active area is less than 2 μm from the touching tip, the probes can easily be physically damaged from touching down to use the capacitive touchdown measurement. In order to find
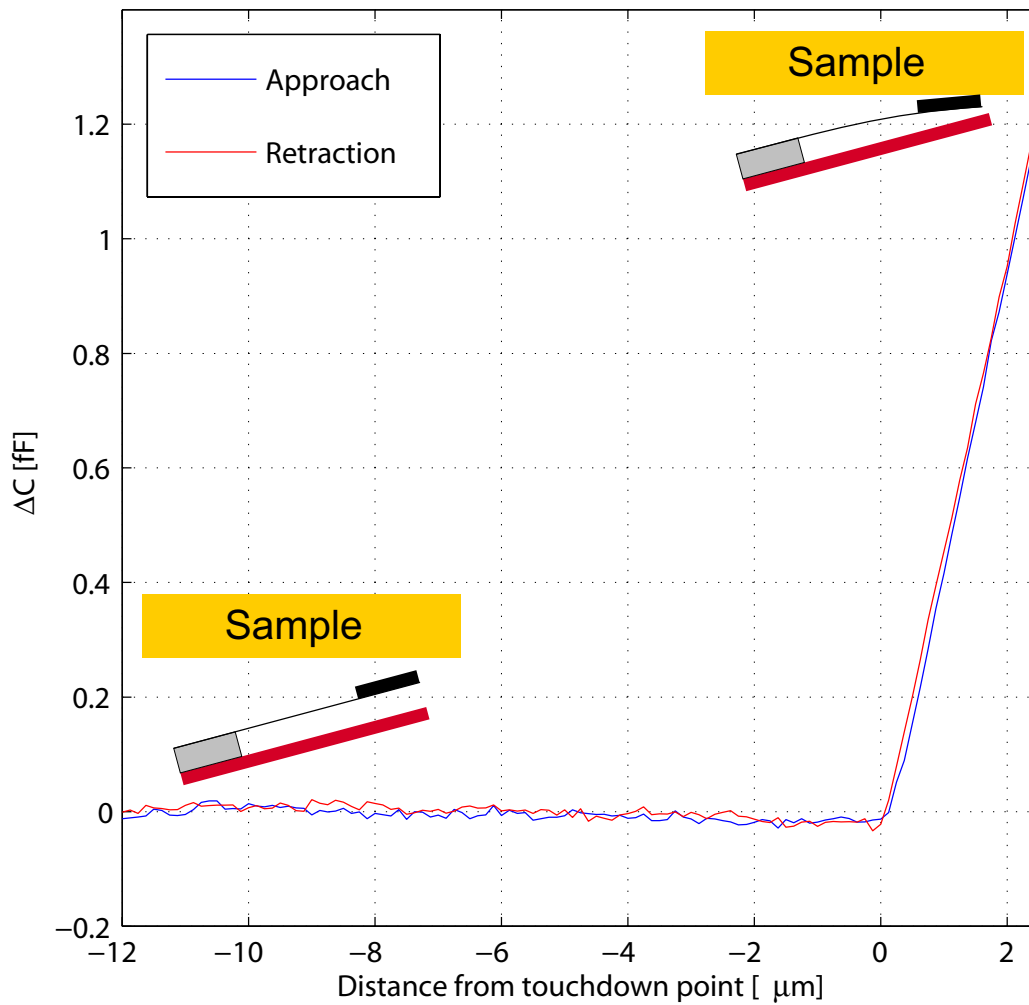
Figure 2.6: Capacitance measurement ramping the Z piezo voltage. At the touchdown point the capacitance starts changing rapidly. Only the deviation in capacitance from the non-touching value is measured.

the sample surface in a less harsh way we have attempted to use electrical tunneling to detect the surface. Using this model, the voltage across the Z piezo is controlled by a feedback circuit. For convenience we have used one of our SQUID controllers as feedback circuit; in practice any PI regulating controller could be used for this purpose. Ideally, one would be able to use this system in pure "STM mode", constantly tunneling from the Hall probe gate and following the surface topography by holding the tunnel current constant. In practice this has turned out to be challenging since it appears that the vibration level of the Z piezo is great enough that it is difficult to stay in tunneling mode while scanning; often the probe ends up oscillating between touching the sample and being far enough from the sample that the tunnel current is completely suppressed.

The main hurdle left in getting "STM mode" to work reliably is that the Z axis vibration level must be improved. The situation was improved significantly when the length of the Z bender was halved, but the improvement was not great enough to make this detection system workable. It is possible that using a stiffer Z bender would be sufficient; however, from the preliminary attempts involving a shorter piezo it appears that the stiffness needs to be increased significantly. In an improved microscope with coarse motion capabilities it may be feasible to rather drastically reduce the Z range since it no longer needs to compensate for thermal drift during the cooldown.

2.2 General Instrumentation Considerations

2.2.1 Refrigeration

The dilution refrigerator used is a commercial Oxford Instruments Kelvinox 100, with a base temperature specified to be below 15 mK. The cooling power is specified to be at least 100 μW at 100 mK. The temperature is measured using a calibrated ruthenium oxide resistance thermometer, measuring the resistance using the "Femtopower" control unit built into the gas handling system. On installation, the thermometer was calibrated against a ^{60}Co nuclear orientation primary thermometer. The factory calibration of the ruthenium oxide thermometer was determined to be accurate to within 1 mK down to base temperature. The base temperature reached with no heat load was found to be 11 mK.

2.2.2   Magnetic and RF Shielding

To reduce stray magnetic fields, the refrigerator dewar is surrounded by a three-layer cylindrical mu-metal shield with a triple-layer bottom. The shielding is designed to reduce a lateral field by 81dB. The shielding specifications did not include a definite specification of vertical field reduction. However, an order-of-magnitude reduction similar to the lateral field shielding is reasonable. The residual magnetic fields that we have seen in the microscope are inhomogeneous and large enough that they appear to be caused by sources inside the refrigerator: typically the actual field at the sample position with no field applied is a few tens of mG.

In order to avoid heating of the sample by radio frequency interference (RFI/EMI) the entire system is enclosed in an RF shielded enclosure. The signal lines are passed into the enclosure through a pass-through panel, where they are filtered using standard low-pass π filters soldered into metal boxes.

2.2.3   Vibration Isolation

For any scanning microscope system, vibrations are an essential issue. The vibrations of the probe must be significantly smaller than the resolution of the images taken. Since the smallest sensor length scale that we are planning for is around 100 nm, vibrations which are only a small fraction of that length scale, probably about 10 nm or less, will not affect the measurements significantly. In order to achieve vibrational noise below this level, the dewar hangs from a wooden tabletop which can be floated on optical table legs. Vibrations entering through pumping lines are reduced by using flexible bellows-style tubing and anchoring all the pumping lines rigidly at the wall of the RF shielded enclosure and passing them through a concrete block.

We have characterized the vibrations at room temperature by using the piezo bimorphs as sensors, connecting a oscilloscope or spectrum analyzer to the electrodes; this was done without actually floating the table, which is the mode in which the setup has normally been used. The rms deviations measured in this way were approximately 0.75 nm in the X direction, 7.5 nm in Y, and 0.125 nm in Z. Turning on the pumps increased the vibrational noise by less than a factor of 2. The lowest resonances of the scanner are at 24 and 30 Hz in X, 26 and 30 Hz in Y, and 22 Hz in Z. While these resonant frequencies are very low compared to smaller-range scanning microscopes, we

have in practice found the performance to be adequate for our sensors – we have never been able to see any enhanced noise that could be traced to vibrations. In actual measurements we have never found vibrations to be a limiting factor for the magnetic sensitivity; as mentioned in Section 2.1.4, improved vibration levels are needed for running the instrument in STM mode for topography measurements.

There are several reasons why STM measurements are so much more sensitive to vibrations than the magnetic probe measurements for which this microscope is designed. First, the STM simply probes a much smaller length scale; since the magnetic sensors used in this microscope average the signal over a much larger area, they are not very sensitive to motion on a length scale which is small compared to the sensor size. Second (but related) the working height of these sensors is large compared to that of an STM tip; when scanning a sensor at an angle above a surface it is impossible to get it as close as a tip pointing toward a surface (as an STM or AFM tip is). Since the fields at the surface spread approximately as the distance from the surface, vibrations which are small compared to the sensor height will not be problematic. Taken together, these effects mean that vibrations of several nm are unlikely to cause any trouble for this microscope, while an STM needs sub-Åvibration levels for good (atomic-resolution) results. Also, an STM intrinsically needs to operate at a low height even if the ultimate resolution is not of interest, since the tunnel current is suppressed exponentially with the tip-sample distance; this is essentially what gives STM its high-resolution properties as well as its sensitivity to vibrations.

2.2.4 High-voltage amplifiers

The piezo benders are connected to high-voltage amplifiers. With piezo benders there is no reason to keep one electrode at ground potential, so we apply symmetric voltages with respect to ground to the two sides of the piezo benders. Using ± 200 V (with regard to ground) high-voltage amplifiers, we can thus apply up to ± 400 V across the piezo benders. This is not advisable at room temperature as the benders that we use are specified for ± 120 V at room temperature in order to prevent depoling. However, at 4K and below the benders do not appear to suffer any damage from the application of significantly higher voltages. The cold dilution refrigerator environment also provides a good vacuum which is important to avoid arcing when applying high voltages.
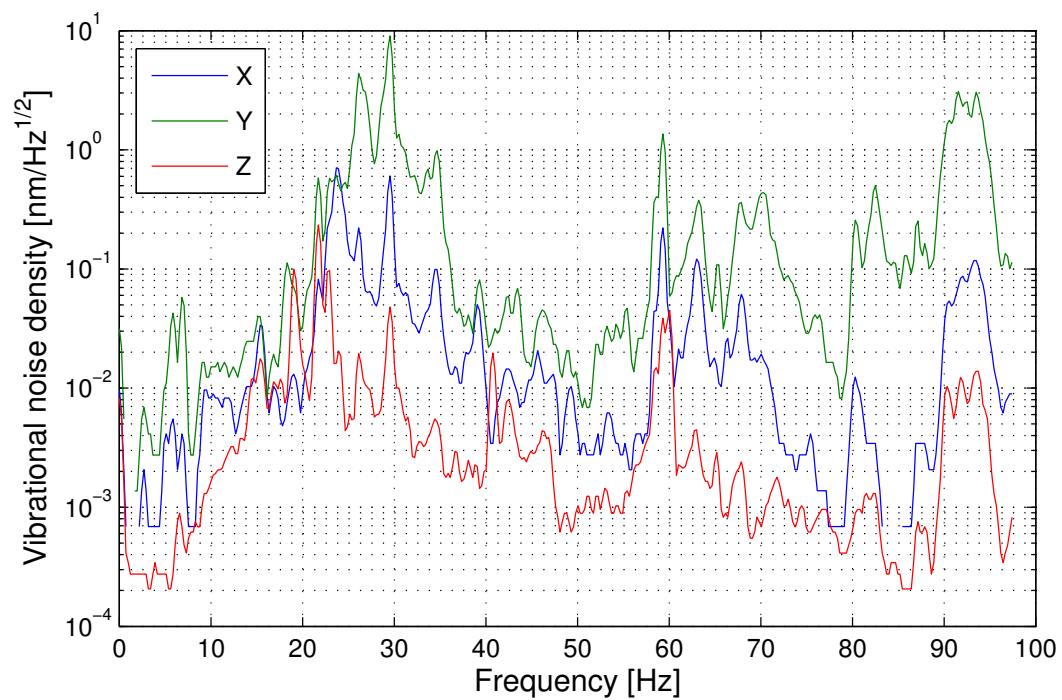
Figure 2.7: Vibration spectra measured at room temperature by connecting the piezo driver lines to a spectrum analyzer. The Y piezo has larger vibrations than the others, presumably because the driven mass includes the mass of the X piezo bender pair.

2.2.5 Scan control system

The motion of the scanner is computer controlled, using 16-bit analog output boards connected to the high-voltage amplifiers. The rastering does not need any feedback, so no real-time computer control is necessary; however, for fast scanning hardware triggering is used to synchronize the single-line voltage output and data readout. When using tunneling touchdowns and feedback control, the feedback is done in a separate analog feedback loop, with the tunneling output feeding back on the Z piezo voltage. For these measurements the Z channel of the high-voltage amplifier was modified to sum the inputs from the analog output board and the feedback control loop, so that an offset plane can be applied in addition to using feedback for height control.

2.3 Experimental Possibilities

The experiments described in this thesis are mainly focused on superconductors, either in thin-film or single-crystal form. However, the utility of this instrument is of course in no way limited to superconductors. Given the materials focus of the rest of the thesis, perhaps the most obvious extension is that there are materials other than superconductors which have an interesting magnetic structure on a length scale that we can access using this instrument. Studying domain structure in magnetic materials is one example that may be pursued.

Another category of measurements for which the instrument is suitable is studies of mesoscopic systems, where electronic coherence effects are in some cases best studied by non-invasive means such as measuring the magnetic field generated by currents in the system. In this case, the scanner is used to position the probe over the sample, not for imaging *per se*. One mesoscopic system which has seen extensive theoretical interest and some experimental effort is persistent currents. The main interest in persistent currents is that they offer a unique way of studying quantum coherence in an isolated system: most other measurements related to quantum coherence effects, such as transport measurements studying weak localization in metallic wires, must be performed with the sample electrically connected to the outside world.

Persistent currents, periodic in the magnetic flux threading a phase coherent normal-metal ring with a periodicity of $\frac{hc}{e}$, were originally predicted by Büttiker, Imry and Landauer in 1983 [Büttiker *et al.*, 1983]. In the simplest possible model – a metallic

loop without impurity scattering at $T = 0$ – the expected approximate magnitude of the current is $\frac{ev_F}{L}$, where v_F is the Fermi velocity and L is the circumference of the loop. However, in a diffusive metallic loop, the expected current is reduced by a factor of $\frac{l}{L}$ where l is the elastic mean free path. Thermal effects may further reduce the expected currents [Chandrasekhar *et al.*, 1991].

The first experiments on this subject were performed by Levy *et al.* on arrays of copper rings [Levy *et al.*, 1990]. The results somewhat surprisingly indicated that there were persistent currents with a periodicity of $\frac{hc}{2e}$, half of the expected period. This was explained by averaging canceling out the $\frac{hc}{e}$ component, which is expected to be random in sign, but not the frequency-doubled component.

Chandrasekhar *et al.* measured the magnetic response of gold rings using SQUIDs, with the rings fabricated directly on the SQUID. They found an $\frac{hc}{e}$ response with an apparent current magnitude that was significantly greater than the expected magnitude: the predicted currents for the experimental parameters were well below 1 nA while the measured peak currents had a magnitude of several nA [Chandrasekhar *et al.*, 1991]. Later, Mailly *et al.* have studied ballistic GaAs/AlGaAs 2DEG rings in a similar way, and found currents in good agreement with simple theories [Mailly *et al.*, 1993]. Finally, Jariwala *et al.* have measured the response of an array of 30 Au rings fabricated in a SQUID pickup loop. These measurements appear to show $\frac{h}{e}$-periodic currents that are significantly smaller than those measured in the earlier experiments [Jariwala *et al.*, 2001].

In the case of diffusive metallic rings, it appears that the experimental results are somewhat contradictory, with question marks specifically because of the limited amount of data available and the question of possible background signals. Both of these problems can be addressed by using a scanning probe microscope for measurements instead of co-fabricating the samples and sensors. Being able to move between many samples in a single cooldown allows many more samples to be used, and the ability to simply back off from the sample and do a null measurement in order to test for background signals is a much better background check than what could be performed for the metallic samples fabricated in the SQUID pickup loops. Furthermore, separating the sensor and the sample allows for a much broader range of samples to be fabricated and measured since the fabrication process does not need to be designed with not damaging the SQUID in mind.

Since the rings that are typically discussed for these measurements have diameters on a μm length scale, it is possible to use SQUIDs that are well matched to the sample size in order to get maximal signal pickup. The magnetic flux from a 2 μm ring with a 4 μm SQUID pickup loop placed 0.5 μm above the sample is approximately 0.6 $\mu\Phi_0/nA$. A typical flux sensitivity for our SQUIDs is around 0.5 $\mu\Phi_0/\sqrt{\text{Hz}}$ at temperatures below 1 K, giving a current sensitivity below 1 nA/$\sqrt{\text{Hz}}$. SQUID noise is discussed in more detail in Chap. 3. With this signal level, measuring currents on the level of those reported by Chandrasekhar *et al.* should be relatively easy, and the theoretical expectations of significantly sub-nA currents should be measurable with reasonable amounts of averaging.

Chapter 3

SQUID sensors

As discussed in earlier chapters, many of the measurements reported in this thesis were performed using Superconducting QUantum Interference Device (SQUID) sensors. This chapter aims to first introduce SQUIDs as magnetic sensors, and then go into more detail regarding the characteristics of the SQUIDs that we have used and participated in developing.

We have used two different generations of SQUIDs. The first is a susceptometer based heavily on Mark Ketchen's original SQUID microsusceptometer [Ketchen *et al.*, 1984], which he and John R. Kirtley (both at IBM T.J. Watson Research Center) modified for use in a scanning configuration [Kirtley *et al.*, 1995; Gardner *et al.*, 2001].

Aiming to improve on the characteristics of these SQUIDs as scanning sensors, we have collaborated with Martin E. Huber on developing a new generation of SQUIDs which have better noise characteristics and improved symmetry and shielding. We have also started using a new high-bandwidth DC feedback system developed at NIST which utilizes a SQUID series array as a low-temperature preamplifier, instead of the traditional AC-coupled flux-locked loop control system.

3.1   SQUID Basics

SQUIDs are the most sensitive magnetic-field probes available, with flux sensitivities as low as $0.1\ \mu\Phi_0/\sqrt{\text{Hz}}$ reported for experimental devices [Ketchen *et al.*, 1991], where the superconducting flux quantum $\Phi_0 = \frac{hc}{2e} = 20.7\text{G}\mu\text{m}^2$.

Conceptually the SQUID consists of a superconducting ring with two Josephson

junctions, which are breaks or weak links in the superconducting material. Cooper pair tunneling is possible across this junction, but the critical current is much lower than for the loop material. When a current larger than the junction critical current is run through the SQUID, a voltage develops across the junctions. The voltage varies periodically with the magnetic flux threading the loop.

The phase difference across a Josephson junction is governed by the Josephson equations [Josephson, 1962],

$$I_s = I_c \sin \gamma \quad \text{and} \tag{3.1}$$

$$\frac{d(\gamma)}{dt} = \frac{2eV}{\hbar} \tag{3.2}$$

where γ is the gauge-invariant phase difference

$$\gamma = \Delta\phi - (2\pi/\Phi_0) \int \mathbf{A} \cdot d\mathbf{s} \tag{3.3}$$

A real Josephson junction can be modeled by the "RCSJ model" - a Resistively and Capacitively Shunted Junction [Tinkham, 1996]. The real junction is modeled as an ideal Josephson junction in parallel with a resistor and a capacitor. Thus the current – voltage relation for an RCSJ-model junction can be written as

$$I = I_{c0} \sin(\gamma) + V/R + C\frac{dV}{dt} \tag{3.4}$$

A DC SQUID is simply a superconducting ring with two Josephson junctions in parallel, illustrated in Fig. 3.1. For simplicity, we will consider a symmetric SQUID, meaning that the two junctions are identical. With zero magnetic flux threading the SQUID, there is equal current through both arms of the SQUID in this case. Thus the phase difference across both junctions is identical and thus the condition that the wavefunction is single-valued is satisfied.

When magnetic flux threads the loop, the wavefunction picks up a non-zero phase from encircling the flux. In order to satisfy the condition that the wavefunction is single-valued (and thus the phase change when encircling the loop is a multiple of 2π), there must be an additional circulating current component which causes a phase difference across the junctions. This causes a change in the voltage across the junctions. Since a
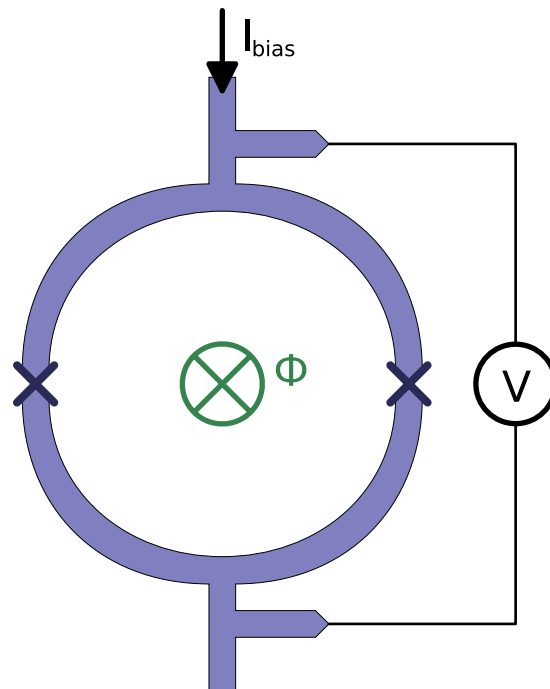
Figure 3.1: A DC SQUID is basically a superconducting loop with two Josephson junctions. At a given bias current (above the junction critical current) the voltage across the SQUID is periodic in the flux threading the loop.

superconducting flux quantum through the SQUID gives exactly a phase contribution of 2π, the voltage is periodic in the flux with a period of the flux quantum.

In order to linearize the signal, a feedback mechanism is used to always keep the flux threading the SQUID at a specific value. Sample-caused changes in the flux threading the SQUID are compensated by running a current through a modulation coil coupled to the SQUID. The actual measured signal is the current through the modulation coil; the deviation of this current from the base point value is proportional to the excess flux though the SQUID. This description is only valid at low fields: at higher fields, flux penetration into the superconductor diminishes the response.

A more in-depth description of the fundamental function of a SQUID can be found in Tinkham's "Introduction to Superconductivity" [Tinkham, 1996]. More technical discussion of SQUIDs and superconducting electronics can be found in "Superconducting Devices and Circuits" by van Duzer and Turner [Van Duzer and Turner, 1998].

3.1.1   First-Generation Scanning SQUIDs: IBM Design

Our first generation of SQUID sensors were based on a design by Mark Ketchen [Ketchen *et al.*, 1984]. The initial design had two counterwound pickup loops connected symmetrically to the SQUID body, and lithographically patterned field coils surrounding the pickup loops which could be used to apply a field locally to a small sample placed in one of the pickup loops. When a field is applied by running a current through the field coils when there is no sample, equal amounts of magnetic flux are passed through each pickup loop. Since the loops are counterwound, i.e. oriented in opposite senses, the net magnetic flux through the SQUID is zero if the SQUID is lithographically perfect. Since this is never truly the case, there is a center tap between the field coils that allows unequal currents to be run through the two coils; this capability is used to trim out the imbalance. Thus any measured signal from applying a magnetic field with the field coils will be caused by the magnetic response of a sample placed in one of the pickup loops. The general design concepts for the SQUID susceptometers are illustrated in Figure 3.2.

The design was modified for use in a scanning probe microscope by Mark Ketchen and John Kirtley [Ketchen and Kirtley, 1995; Kirtley *et al.*, 1995]. The major modification of the original susceptometer design was to move one of the pickup loops far from the main body of the SQUID, in such a way that the chip it was fabricated on could
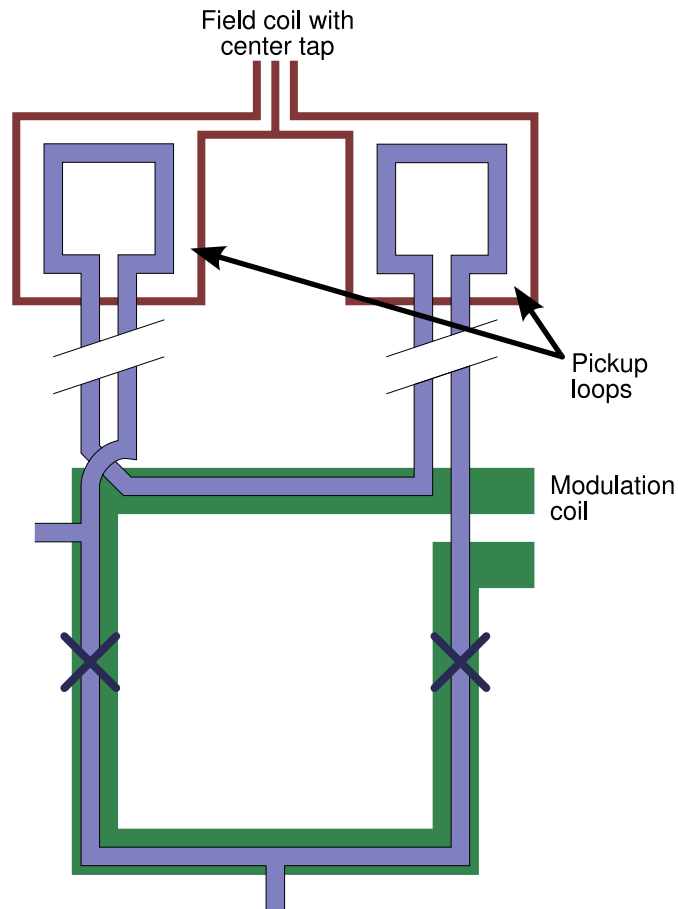
Figure 3.2: Sketch illustrating the fundamentals of Ketchen's SQUID susceptometer. The two pickup counterwound pickup loops with surrounding field coils allow a magnetic field to be applied locally, only measuring the magnetic response of a sample placed in one of the pickup loops.

be polished to a point close to that loop. In addition, the leads to the pickup loops are fabricated as coaxial striplines in order to minimize the stray pickup area. This can be done in a three-metal-layer lithography process.

The pickup loops in our first-generation SQUIDs were squares with a side of 8 μm, and the field coils were octagons which are 21 microns across. The devices that we have used were fabricated at the commercial superconducting electronics foundry HYPRES based on our design files.

The tip could be polished to around 30 μm from the center of the pick-up loop; the practical height of the pickup loop above the surface is thus generally limited to around 2 μm: the height of the SQUID chip at the position of the pickup loop is $\sin 3° \times 30 \quad \mu$m $\approx 1.6\mu$m and the pickup loop is covered by close to 0.5 μm of SiO$_2$. However, given the size of the pickup loop, this height generally does not limit the resolution.

These SQUIDs have generally been run in a traditional AC flux-locked loop feedback system, using a low-temperature transformer circuit to connect the SQUID to the room-temperature electronics. This has the disadvantage of limiting the possible bandwidth to a fraction of the lock-in frequency used; the frequency used in our IBM-designed SQUID controller is 100 kHz, and this SQUID controller limits the bandwidth to around 400 Hz.

The first-generation SQUIDs we used were fabricated by HYPRES, a commercial superconducting electronics foundry. The design files were provided by John Kirtley, in some cases with minor modifications by us. The normal HYPRES process [Hypres, Inc., As available online in June 2005] uses molybdenum (Mo) shunt resistors; this is not suitable for use at dilution refrigerator temperatures since Mo is superconducting with a T$_c$ of 900 mK. This is obviously unfortunate since the "resistors" would then short out the Josephson junctions at the temperatures which we are interested in working at. For this reason, HYPRES did occasional runs with a different process using Pd/Au shunt resistors which are non-superconducting. This process, for reasons entirely unrelated to the shunt resistors, also used a lower critical current density in the junctions. This is entirely unrelated to the change in shunt resistor material: it appears that some major customers of the foundry needed a process with In order to accommodate for this we increased the junction area for this set of SQUIDs; however it was kept small enough to avoid issues related to the increased junction capacitance.
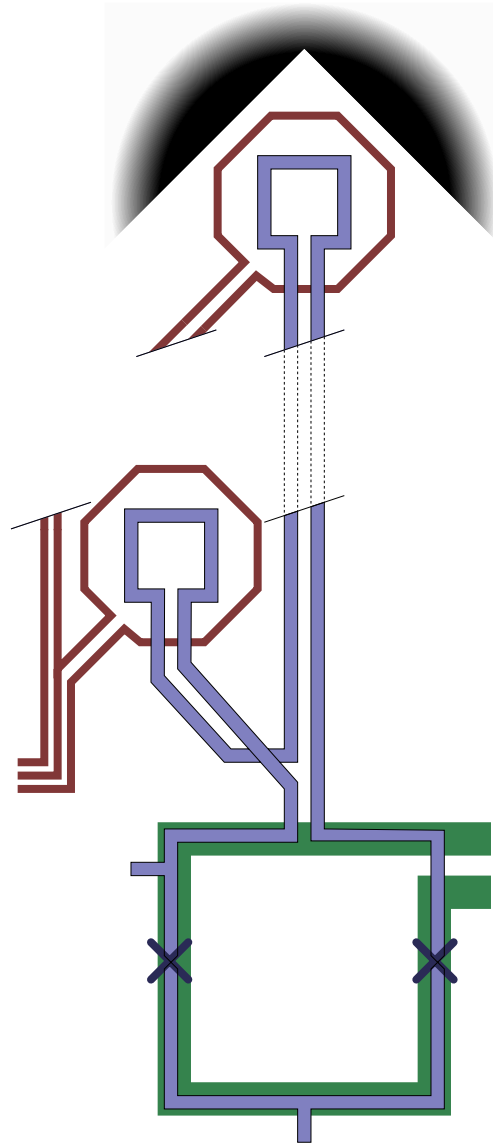
Figure 3.3: a) A sketch of the design of our "first-generation" scanning SQUID design. b) Micrograph of the square front SQUID pickup loop, with a tip polished to a distance of around 30 μm from the center of the pickup loop. The polishing distance is limited by the octagonal field coil.
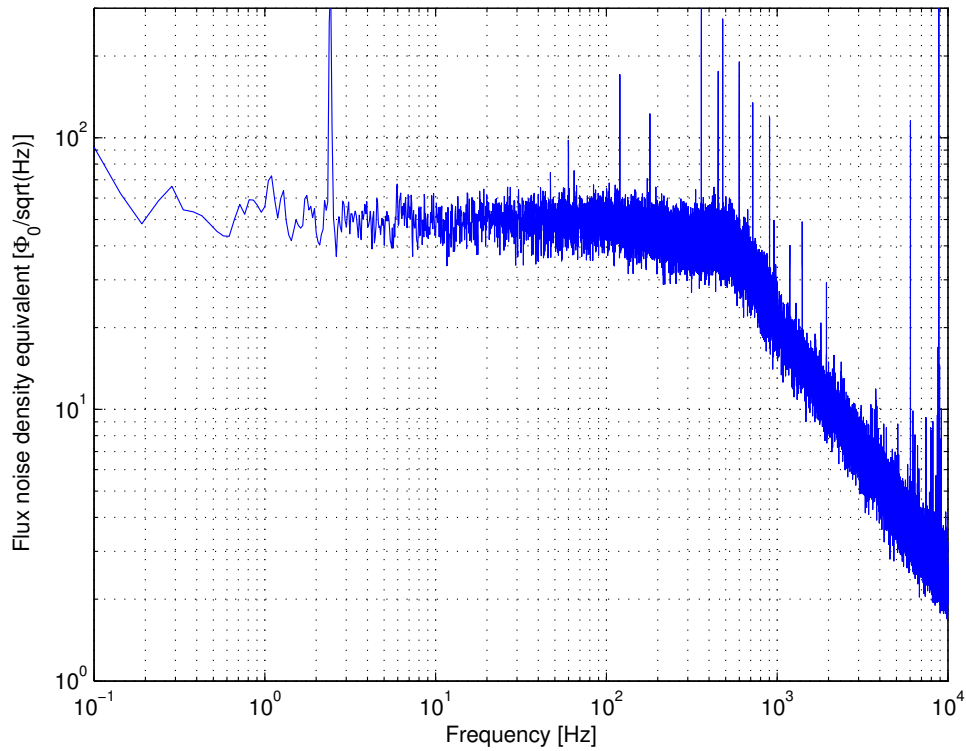
Figure 3.4: Typical noise of the first-generation scanning SQUIDs in an AC feedback loop, with a white noise level around 50 $\mu\Phi_0/\sqrt{\text{Hz}}$. The knee around 500 Hz is due to bandwidth limitations in the system. This noise is significantly higher than the intrinsic noise of the SQUIDs as measured directly in a setup without the feedback loop.

The sensitivity (noise floor) of the first-generation SQUIDs using the AC feedback electronics is about $50\ \mu\Phi_0/\sqrt{\text{Hz}}$ with the aforementioned bandwidth of less than 1 kHz (varying with different measuring setups). A typical noise curve using this setup is shown in Fig. 3.4. This relatively high noise level is an artifact of the measurement setup: in other (non-scanning) setups we have measured the intrinsic noise of the SQUIDs to be about $7\ \mu\Phi_0/\sqrt{\text{Hz}}$.

3.1.2 Attempts to minimize the pickup loop area

Attempting to improve the spatial resolution of the first-generation SQUIDs, I modified the design fabricated by HYPRES so that the pickup loop was replaced by a tab, as illustrated in Fig. 3.5. The plan was to process the SQUIDs further at the Stanford Nanofabrication Facility using e-beam lithography to pattern the tab into a sub-micron pickup loop. The plan was ultimately unsuccessful and was abandoned for several reasons, but several useful lessons were learned and the fabrication processes which were developed may be useful for future developments.

The main reasons for abandoning the project were:

- Patterning the pickup loops turned out to be very challenging using the equipment available at SNF. In particular, the e-beam writer available at the time, a Hitachi HL-700, was not able to consistently reach the necessary feature sizes to be useful. In addition, the machine was optimized for high-throughput processing on wafers; unfortunately this impaired its functionality for processing small chips significantly, in particular with respect to layer alignment - the machine often did not detect the alignment marks on small samples and there was no good system for manually aiding the alignment. Since this is a purely technical limitation it can be overcome by using a different e-beam writer, such as the Raith 150 which has now been installed at the SNF.

- The limits on the SQUID design set by the HYPRES fabrication process necessarily forces a pickup loop with well-shielded leads to be fabricated close to a large Nb area. This makes it practically impossible to avoid large amounts of flux focusing into the pickup loop, giving a pickup area which is difficult to characterize and much larger than the lithographically defined size [Ketchen and Kirtley, 1995]. This would severely reduce the value of these probes for scanning
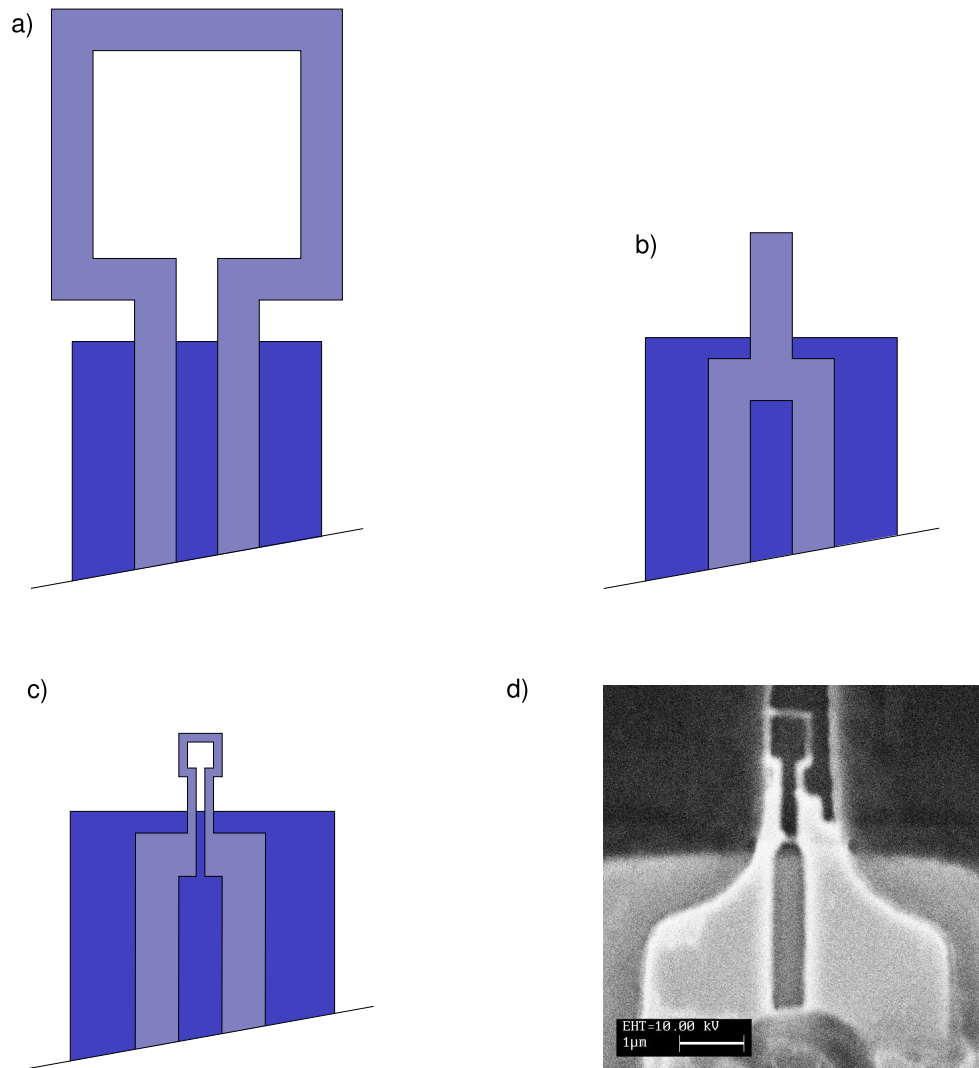
Figure 3.5: Attempts to modify specially designed 1st-generation SQUIDs using e-beam lithography in order to produce submicron pickup loops. a) The regular 1st-generation SQUIDs have pickup loops fabricated using the HYPRES photolithographic process. Lithography limits set a practical lower bound on the pickup loop size of 8 μm. b) The pickup loop was replaced by a tab in order to make e-beam lithography modifications possible. c) Sketch of one attempted pickup loop geometry. d) Electron micrograph of one of the attempts to fabricate the geometry in (c) that was closest to succeeding.

microscopy. Similar SQUIDs could still be useful e.g. for studying individual mesoscopic samples placed in the pickup loop.

- A further problem with integrating the HYPRES process with e-beam post-processing is that there is no flexibility in the layer structure. Because of shielding and other considerations, the pickup loop layer had to be fabricated in a layer buried under around 0.5 μm of SiO_2 This limits the attainable distance from the sample surface to the pickup loop and diminishes the benefits of a small pickup loop.

Given these problems we found it more fruitful to continue the work on smaller SQUIDs in another direction: a different SQUID design, immediately developed with scanning and small pickup loops in mind, which we have pursued in collaboration with Martin Huber at CU Denver.

3.2 Second-Generation SQUIDs

In order to enable more sensitive SQUID measurements we have worked in collaboration with Martin Huber at University of Colorado at Denver on a new generation of SQUIDs with superior characteristics for scanning. The improvements are both in an improved geometry, laying the groundwork for SQUIDs with significantly improved spatial resolution, and in an improved flux noise level.

It is worthwhile to note that the size of the pickup loop is a very significant factor not only for the spatial resolution but also for the spin sensitivity of the SQUID: if the field is dipole-like, a large pickup loop will enclose very little net flux [Ketchen *et al.*, 1989].

While the experience from using the IBM-designed SQUIDs was important in guiding the design of the new generation of SQUIDs, the design was done entirely from scratch. The main design goals can be summarized as follows:

- *Optimized for scanning.* This implies, among other things, that there is a large separation between the two field coils so that the rear pickup loop will be affected as little as possible by the sample, and the wire bonds are placed at the rear end of the SQUID so that they do not unnecessarily limit the angle at which the probe can be scanned.

- *High symmetry.* A symmetric design will tend to reduce spurious resonances in the SQUID; this should reduce the noise level and make it much easier to work with, since the SQUID is much less sensitive to small deviations from the ideal operating point. A design that is symmetric with good precision also eliminates or reduces the need for manual balancing of the current through the field coils. This is very convenient in case the resistance of the wiring is not known to be constant: in case the balancing is accomplished with a passive resistor network, it is naturally sensitive to the wiring resistance. If no balancing is needed this problem is overcome entirely, eliminating one possible source of measurement errors. In addition, if the main body of the SQUID is "twisted" such that it has equal pickup in opposite flux directions, a uniform background field will have little effect on the SQUID, under some circumstances allowing operation in an applied moderate background field.

- *Possibility of integrating e-beam lithography steps.* In order to achieve the goal of small pickup loops, higher-resolution lithography than what is possible using small-scale optical lithography techniques is essential; line widths of around 100 nm would be necessary to reach the ultimate design goals. In order to do this while keeping the fabrication process feasible it is essential to design the SQUID in such a way that all the small features can be done in a few (preferably one) electron-beam lithography step which can be integrated into the process flow.

Our current SQUIDs have been produced in a process using only optical lithography. The smallest pickup loops fabricated in this process have had a diameter of 4 μm. The NIST optical lithography process has design rules specifying line widths close to 1 μm; in order to define well-formed pickup loops with a significantly smaller pickup area, continuing work on integrating e-beam lithography (or some other higher-resolution processing method) in the process will be necessary.

3.3 DC control loop for SQUIDs

Together with the second generation of SQUIDs we have used a new DC feedback system originated by John Martinis and coworkers at NIST [Welty and Martinis, 1991]. Using a DC feedback system allows operation at much higher frequencies, since one is no longer
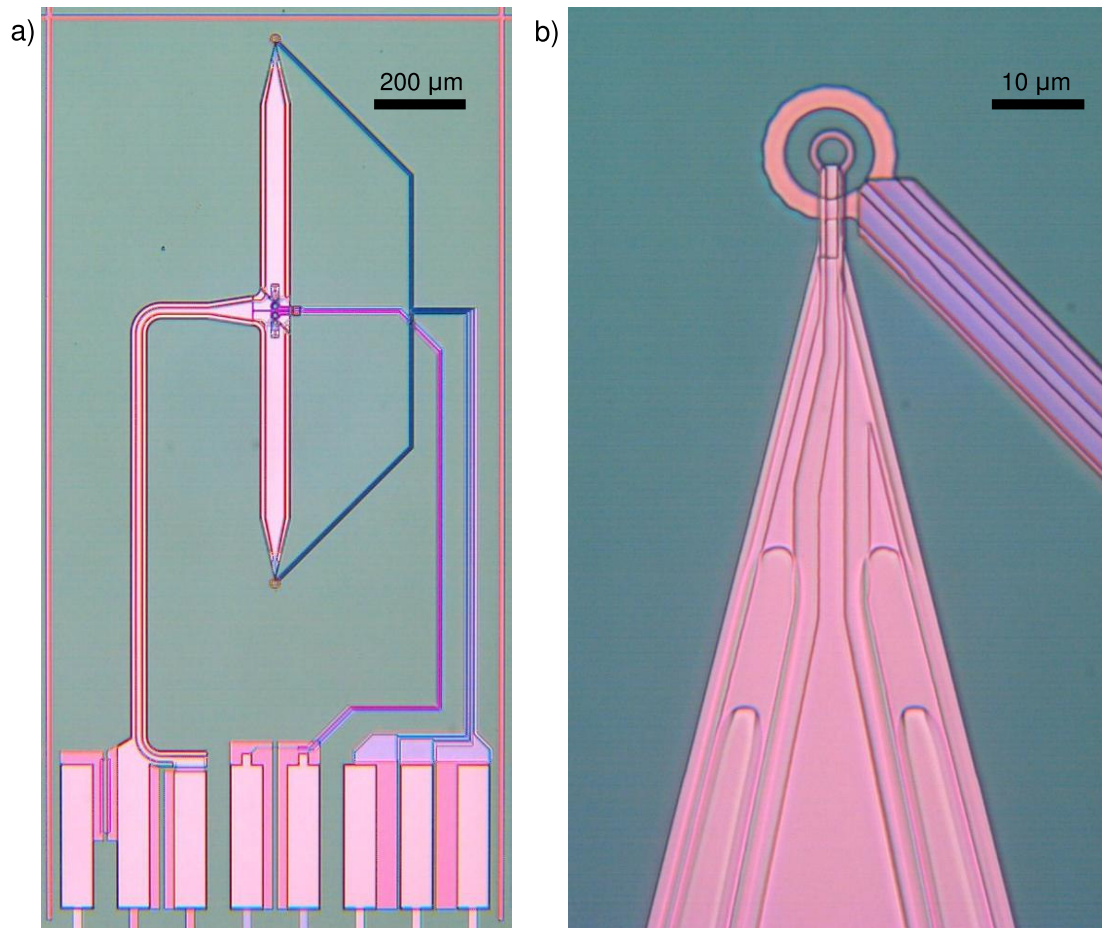
Figure 3.6: The 2$^{\text{nd}}$ generation scanning SQUID design. (a) A full SQUID chip with a 4 μm pickup loop. (b) Close-up of the pickup loop area.
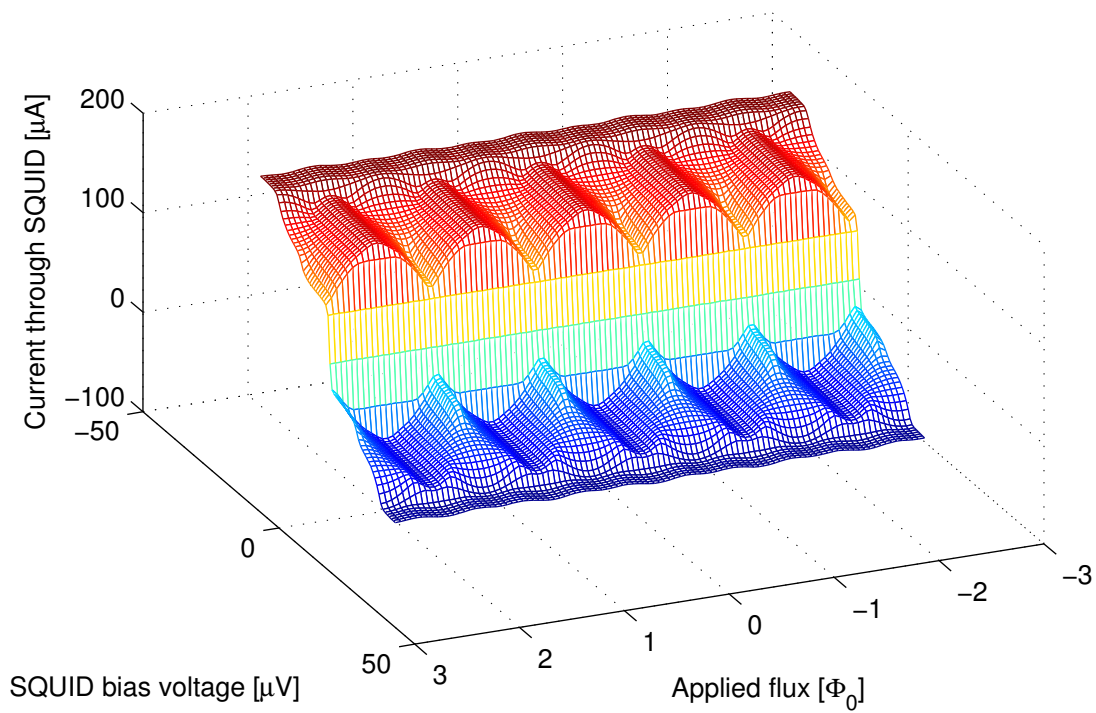
Figure 3.7: Measured flux-voltage-current landscape for a second-generation SQUID at 4K.

bandwidth limited to a fraction of the AC chopping frequency of a traditional flux-locked loop. A system bandwidth of 120 MHz has been experimentally demonstrated using this type of feedback system [Huber *et al.*, 2001].

In order to make DC feedback possible, low-temperature preamplification is necessary; otherwise the impedance mismatch between the wiring and the SQUID would make room-temperature readout impossible. The solution employed by Martinis *et al.* is to use a series array of SQUIDs as a low-temperature current-to-voltage preamplifier. The modulation amplitude of the arrays is as large as several mV, and the output impedance of a 100-SQUID array is reasonably well matched to standard coaxial transmission lines: the typical output impedance is on the order of 1 Ω per SQUID in the array and coaxial cables for cryogenic use are generally in the $50 - 100$ Ω impedance range. This minimizes problems with connecting the signal to the room-temperature part of the feedback loop and allows for higher bandwidth.

The standard way to use the arrays is as a current preamplifier, using a room temperature feedback circuit to linearize the signal. The feedback current, which is applied to the array feedback coil, is proportional to the input current. Using this feedback system means that the array is always operated at a constant flux bias point.

When using the arrays with a front end SQUID such as our scanning susceptometers, the feedback current is instead fed into the feedback coil of the susceptometer SQUID, as illustrated in Fig. 3.8. A constant current is applied to the SQUID array feedback coil to bias it at a suitable fixed point.

In order to get a current signal from the front-end SQUID, it is operated in voltage-biased mode instead of the current-biased mode that is commonly used with AC feedback mechanisms. The voltage biasing is accomplished by connecting a small resistor in parallel with the SQUID and applying a bias current. The effective SQUID resistance is typically limited by the shunt resistors to around 1 Ω, so the resistance of the parallel resistor is much smaller than the SQUID resistance. Thus, when running a current greater than the Josephson critical current through the SQUID, the voltage will be held close to constant. Since the SQUID is also operated at a constant operating point thanks to the flux feedback, the voltage biasing does not actually have to be perfect; moderate non-linear effects will be compensated by the feedback, and thus the setup is fairly insensitive to the precise value of the bias resistor or the relative resistance of the bias resistor and the effective SQUID resistance.

Figure 3.8: The DC feedback loop with a SQUID array used as a low-temperature preamplifier. The susceptometer SQUID (at the bottom) is voltage biased using a small resistor. A SQUID array is used to measure the current though the susceptometer. Linearization is achieved by feeding back flux into the susceptometer, while the array is DC flux biased at a suitable operating point.
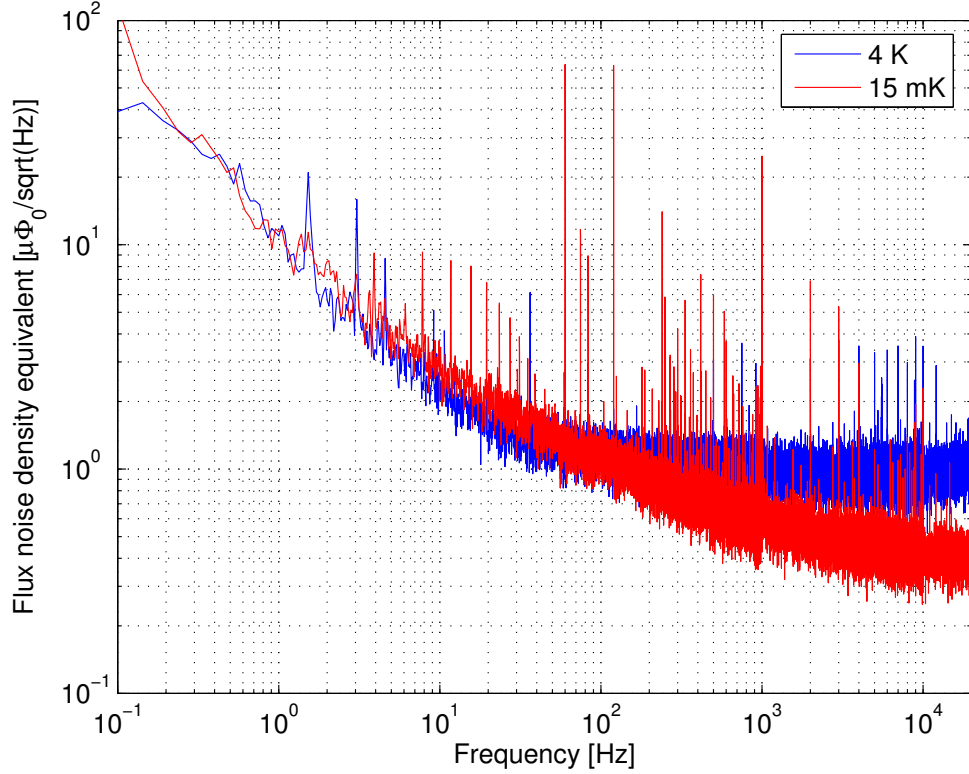
Figure 3.9: Comparison of the SQUID noise at 4 K and at the dilution refrigerator mixing chamber temperature of 15 mK.

3.4 SQUID Noise and Bandwidth

Two of the most important figures of merit for sensors (at least given a particular pickup loop shape) are the noise level and the available measurement bandwidth. Since the response of the DC feedback system is not limited to a fraction of any chopping frequency (like the AC flux-locked loop is), it allows much higher bandwidth, at the cost of possibly having less favorable low-frequency properties, since the AC system allows measuring in a narrow bandwidth at a frequency above the $1/f$ knee, while the DC system is limited to averaging at low frequencies. In practice in our systems, while the white noise corner frequency is certainly higher for the DC feedback system than for the traditional AC feedback loop (where we generally cannot see any low-frequency

roll-off at all; a typical noise curve is shown in Fig. 3.4), the absolute magnitude of the noise at frequencies important to measurements is lower. For the most sensitive low frequency measurements it may be necessary to replace the amplifiers in the room-temperature preamplifier and feedback system with components optimized for low-frequency noise at the expense of bandwidth; however, we have not yet reached a system noise level motivating this type of modification. We have measured a white noise level of 1 $\mu\Phi_0/\sqrt{\text{Hz}}$ at 4 K and about 0.5 $\mu\Phi_0/\sqrt{\text{Hz}}$ at temperatures below 1 K, as seen in Fig. 3.9. However, in our measurements we have not found any temperature dependence of the noise level below 1 K.

Since SQUIDs measure magnetic flux, the simplest figure of merit for the performance is simply the flux noise. However, this is not always the most interesting parameter for measurements. In some cases the ultimate magnetic field sensitivity might be important, no matter what the spatial resolution is. In this case, a large SQUID will give extremely low field noise levels, since the flux is divided by a large area. For scanning microscopy, the most interesting parameter can often be magnetic dipole sensitivity, often quoted as spin sensitivity in units of $\mu_B/\sqrt{\text{Hz}}$. For a circular pickup loop of diameter d, the relation between the spin sensitivity $S_s^{1/2}$ and the flux sensitivity $S_\Phi^{1/2}$ in units of $\mu\Phi_0/\sqrt{\text{Hz}}$ is

$$S_s^{1/2} = \frac{d}{2r_e} S_\Phi^{1/2} \tag{3.5}$$

where r_e is the classical electron radius (2.8×10^{-15} m) [Ketchen *et al.*, 1989]. For our low-temperature flux sensitivity of 0.5 $\mu\Phi_0/\sqrt{\text{Hz}}$, this gives a white noise floor for the spin sensitivity around 360 $\mu_B/\sqrt{\text{Hz}}$.

For extended samples, such as the mesoscopic rings discussed in Section 2.3, the magnetic coupling in most cases must be calculated numerically. Experimentally reasonable parameters for our current SQUIDs are a ring with a diameter of 2 μm and the 4 μm diameter SQUID loop held 1 μm above the ring. Using these parameters, the flux through the SQUID is approximately 0.32 Φ_0/nA with the SQUID centered above the ring; this is reduced by less than 0.4 % when the ring is off-center by 100 nm, indicating that the measurement is relatively insensitive to vibrations. This gives us a low-temperature current sensitivity of 1.6 nA/$\sqrt{\text{Hz}}$. A plot of the calculated signal for the SQUID and ring geometries discussed here as a function of off-center position is shown in Fig. 3.10.
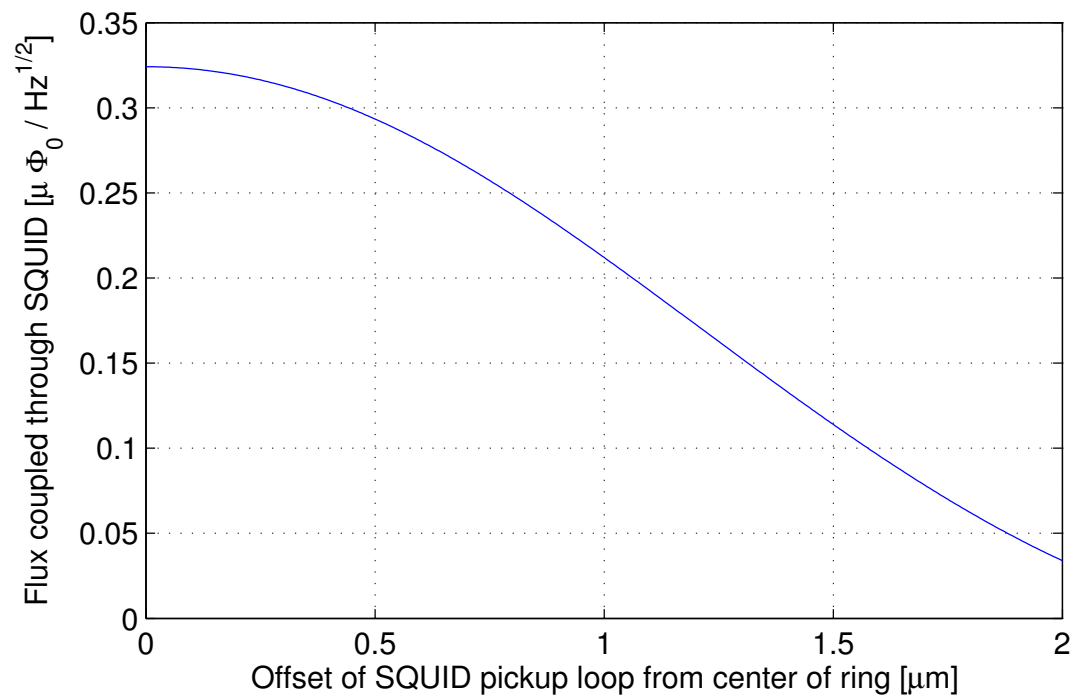
Figure 3.10: Calculated magnetic coupling of ring of diameter 2 μm to a 4 μm diameter SQUID pickup loop 1 μm above the ring, as a function of the offset of the ring center from the center of the pickup loop.

The bandwidth of the SQUIDs in the dilution refrigerator setup is limited by the wiring, not by the SQUIDs or the feedback system. The greatest limitation is in fact not in the measurement system at all, but is caused by feeding the on-chip field coils through twisted pair wiring, which limits the bandwidth for susceptibility measurements to around 10 kHz. Improving the bandwidth to a few MHz should easily be accomplished by only using coaxial wiring and making sure that there are no significant impedance mismatches for all connections that need a broad frequency response. For the measurements reported in this thesis this has not been necessary.

Chapter 4

Hall Probes

In addition to the SQUIDs described in the previous chapter, I have used Hall probes as sensors for magnetic imaging. In this chapter I discuss Hall probe functionality and the issues, primarily regarding noise and spatial resolution, to consider when using Hall probes for scanning microscopy. In particular I discuss the noise properties of the Hall probes used in the Moler lab.

Hall probes are magnetic field sensors based on the Hall effect. This effect is the generation of a transverse voltage across a conductor, proportional to the current through the conductor, when it is subjected to a magnetic field.

The technique of using micro-Hall probes for microscopy was developed in the early 1990s, with significant contributions by the research groups of Chang and Hess [Chang *et al.*, 1992], Fields [Siegel *et al.*, 1995] and Bending [Oral *et al.*, 1996].

In the research reported in this thesis, four generations of Hall probes have been used, generally with improved spatial resolution for each successive generation. The first generation was fabricated by Kathryn Moler, the second generation by Janice Wynn Guikema [Guikema, 2004], and the third and fourth generations by Clifford Hicks.

4.1   The Hall Effect

The basics of the Hall effect can be understood in terms of the Lorentz force. A moving charged particle is subjected to a Lorentz force

$$\vec{F} = q(\vec{E} + \vec{v} \times \vec{B}) \tag{4.1}$$
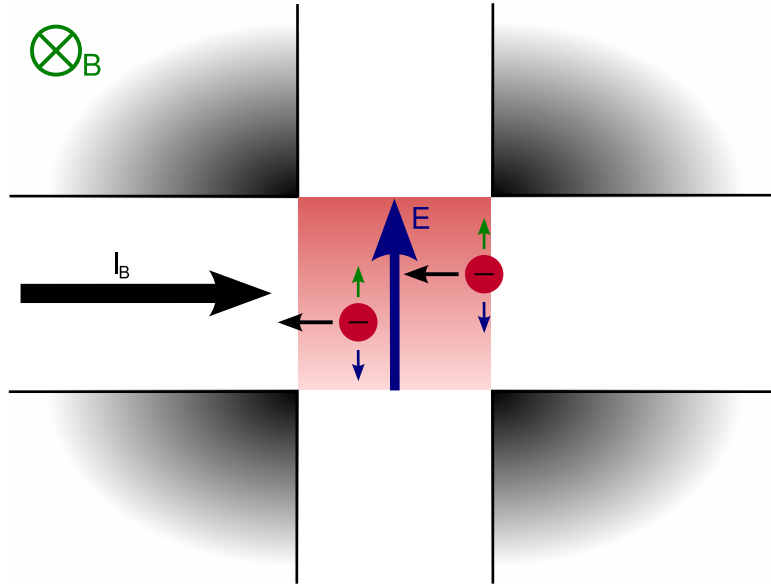
Figure 4.1: A Hall sensor in a magnetic field $\vec{B}$. The Lorentz force caused by the motion of the charge carriers in a B field is balanced by the force from the E field originating in the charge gradient across the sensor.

where $\vec{E}$ is the electric field and $\vec{B}$ is the magnetic field in which the particle is moving; the component caused by the magnetic field is perpendicular to the direction of motion. Since a current is composed of moving charged particles, this affects the charge carriers in a conductor as well. However, since the particles are confined to the conductor they do not change direction. Instead, the force caused by the magnetic field causes a charge imbalance between the sides of the conductor which exactly counteracts the force caused by the magnetic field, so that the net force on the particles is zero:

$$q\vec{E} = -q\vec{v} \times \vec{B}. \tag{4.2}$$

The $\vec{E}$ field is perpendicular to the current direction and can also be written as V_H/w where V_H is the generated transverse voltage and w is the width of the conductor.

In a conductor it is also more convenient to characterize the motion in terms of the current I, as opposed to looking at individual charged particles. The current is simply the charge passing through a cross section of the conductor per unit time (assuming a

rectangular slab conductor for convenience):

$$I = -n_V qvtw \qquad (4.3)$$

where n_V is the volume density of charges, t is the conductor thickness and w is the conductor width. Thus for a thin flat slab Equation 4.2 turns into

$$n_V t q V_H = I B_\perp \qquad (4.4)$$

where $B_\perp$ is the component of the magnetic field perpendicular to the conductor. Expressing the Hall voltage as a function of the magnetic field this is

$$V_H = \frac{1}{n_V t q} I B_\perp. \qquad (4.5)$$

This equation shows that in order to achieve an appreciable Hall response, it is important that the carrier density in the conductor is low, and ideally confined to as thin a layer as possible in order to minimize the sheet carrier density $n_v t$. In order to achieve this, Hall probes are often fabricated in GaAs/AlGaAs heterostructures which have a conduction layer of electrons confined to one of the GaAs/AlGaAs interfaces, known as a "2-dimensional electron gas" (2DEG). At low temperatures the electronic wavefunctions are confined to a single mode in the vertical direction. In this kind of structure the volume density of electron is not a sensible parameter, instead the sheet density (n) is the correct measure so the formula for the Hall effect turns into

$$V_H = \frac{1}{ne} I B_\perp. \qquad (4.6)$$

There are also other factors beyond the Hall response that affect the signal to noise ratio of a Hall probe. I will discuss Hall probe noise later in this chapter.

4.2 Hall probe fabrication

Our Hall probes are fabricated on GaAs/AlGaAs heterostructures, in which a 2DEG forms at one of the GaAs/AlGaAs interfaces. The probes are defined by lithographic patterning (using e-beam lithography for the probe areas of the sub-micron probes) and reactive ion etching; the 2DEG is depleted and left non-conducting in the areas where

the surface is etched.

The fabrication process is done in several steps. The probe area is defined first, with e-beam and/or optical lithography and a shallow etch. The shallow etch is kept just deep enough to deplete the 2DEG - a deeper etch would not allow as high resolution, since there is a depletion region surrounding the physically etched area and a deeper etch will cause a larger depleted 2DEG area. Contacts are made to the 2DEG using a standard recipe using an annealed stack of AuGe/Ni/Au. The AuGe forms a eutectic alloy which penetrates into the substrate and makes contact with the 2DEG through the annealing process.

4.2.1   Scanning Hall probes

There are several special factors that need to be taken into consideration when Hall probes are to be used for scanning probe microscopy. First, the probe is actually sensitive to electric as well as magnetic external fields, since an electric field will have a gating effect and cause a change in the electron density in the probe. In order to avoid stray signal from e.g. charges on the surface, the sensor area can be protected with a metallic gate that can be grounded in order to screen out external electric fields. However, in this case care must be taken that the voltage between the gate and the active area is small since otherwise the Hall probe may be depleted, and since there may be current leakage between the gate and the probe if the voltage is too large.

A second concern is that the probes must be fabricated in such a way that they can be brought close to the sample. Just as for the SQUIDs discussed in the previous chapter, one necessary condition is that a tip can be polished on the Hall probe chip such that the active area is very close to the corner. In general, this means fabricating the Hall probes so that they can be polished to a tip close to the active area. However, manual polishing is a difficult way to get the edge very close to the active area for two reasons: First, it is simply difficult to polish the probes with micron-scale precision, and second there is a risk of physical damage or introduction of defects that may cause unpredictable depletion regions, possibly cutting off the active area entirely. Thus we define a tip using a deep mesa etch, with a depth of several microns, using lithography and etching techniques. The first-generation probes had a tip defined by wet etching; this technique turned out not to be successful for the finer geometries attempted for the later generations, e.g. due to undercutting of the resist when etching. In order to

Generation	Min. Size	Lithography	2DEG Origin
1	2 μm	K. Moler	D. Kisker (IBM)
2	0.5 μm	J. W. Guikema	D. Kisker
3	130 nm	C. W. Hicks	H. Shtrikman (WIS)
4	85 nm	C. W. Hicks	H. Shtrikman

Table 4.1: Hall probe generations used in the Moler lab. The third generation of probes is not suitable for scanning microscopy since no deep etch has been applied.

get around this problem, the process was changed to reactive ion etching, which allows better control over the etch profile.

4.3 Resolution and sensitivity

There are several reasons to attempt to improve the spatial resolution of Hall probes to the greatest extent possible. The most obvious is simply that features can be resolved on a smaller length scale. Only features that have spatial variations on length scales no smaller than the size of the active area can be resolved.

As discussed in the context of SQUIDs in Sec. 3.4, for dipole (and higher-order multipole) fields there may also a large sensitivity gain from decreasing the size of the sensor; whether this is true or not depends on how the field sensitivity changes with size. This can easily be understood by considering a large sensor: much of the magnetic flux from the sample will pass both up and down through the sample and thus the average magnetic field will be low. With a smaller sensor less of the field lines have a return path through the probe, so the total signal contribution is greater. Considering Eq. 3.5, we have a relationship between the sensor size s and the spin sensitivity

$$S_s^{1/2} \propto s^3 S_B^{1/2}. \tag{4.7}$$

where $S_B^{1/2}$ is the rms field noise density of the Hall probe. Thus, unless $S_B^{1/2}$ increases faster than $1/s^3$, a smaller sensor will have better spin sensitivity.

Most of our Hall probes have been size limited by fabrication concerns; it is technically difficult to fabricate deep-submicron structures. However, the difficulty extends beyond just better lithography: as the lithographic feature size is decreased, the fact
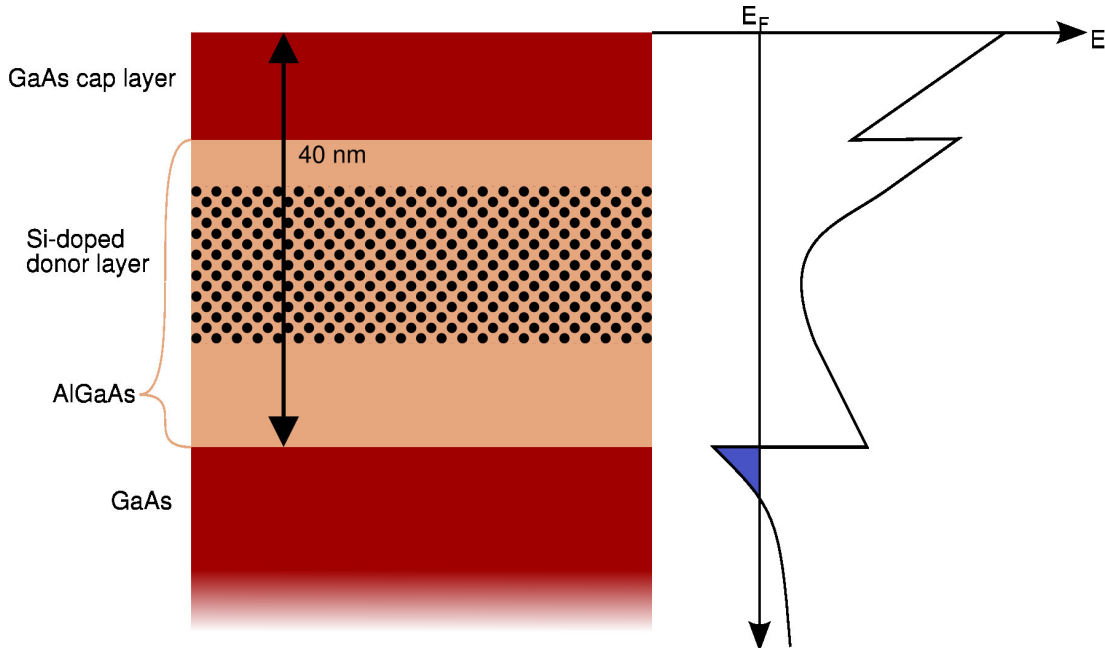
Figure 4.2: Illustration of the 2DEG structure used for the generation 3 and 4 Hall probes. The energy level diagram, based on calculations by C. W. Hicks, is shown on the right-hand side. The 2DEG forms at the GaAs/AlGaAs interface.

that the depletion area is larger than the physically etched area becomes increasingly important, since the fraction of the lithographically defined active area that is depleted is increased. This effect becomes more significant with increasing 2DEG depth. Also, the resolution is not only limited by the size of the active area but also by the height of the sensor above the surface. For both of these reasons it is essential to have a 2DEG that is relatively close to the surface of the heterostructure. Our early probes (1st and 2nd generation) were fabricated on heterostructures grown by David Kisker at IBM; these has a depth of 140 nm, while the later generations were fabricated on 2DEG only 50 nm deep, grown by Hadas Shtrikman at the Weizmann Institute of Science in Israel. The structure of the Weizmann 2DEG is illustrated in Fig. 4.2.

4.3.1   Hall probe noise characteristics

The dominant low frequency noise in large Hall probes is typically $1/f$ noise, while the smaller probes often mainly exhibit random telegraph noise (also known as switching

noise). This is not contradictory: When the telegraph noise from many sources with distinct switching rates and amplitudes is averaged, the resulting spectrum has a $1/f$ characteristic. Similar behavior is seen in the $1/f$ noise found in devices such as silicon FETs [Uren *et al.*, 1985]. The source of the switching noise is believed to be changes in the electronic configuration in the donor layer, which locally changes the potential in the conduction layer.

The switching noise changes the *resistance* properties of the Hall probe. Thus it is difficult to separate from the measured magnetic signal. The only possible way to avoid the low-frequency noise when scanning is to scan quickly, process the averages to reduce low-frequency noise (e.g. with line averaging, if that can be motivated - this depends on the type of signal seen) and average many of the fast scans. This is quite different from SQUIDs where the low-frequency noise is often less problematic and it is possible to average for a long time in a single scan.

4.3.2 Noise data on our Hall probes

We have tested a range of Hall probes primarily designed for scanning applications. The probe sizes have ranged from 80 nm to 10 μm. We have focused on characterizing the size and temperature dependence of the Hall probe noise.

Since our main interest in Hall probes is using them in low-temperature systems, we have focused on their low-temperature noise properties as well. In general, at low frequencies our Hall probes have either a $1/f$-like or somewhat bumpy noise profile. At higher frequencies, the white noise floor has always been set by room-temperature amplifier noise; our measurements have never been limited by intrinsic Johnson thermal noise in a Hall probe at low temperatures. The voltage noise of our preamplifier is 4 $nV/\sqrt{\text{Hz}}$, while at 4 K the Johnson noise of a Hall probe with a resistance of 1 kΩ has a voltage noise density $S_e^{1/2} = \sqrt{4k_B T R} \approx 0.5\text{nV}/\sqrt{\text{Hz}}$.

At temperatures below 4 K there is very little temperature dependence of the noise. However, the noise profile is quite sensitive to the bias current; this appears to indicate that the noise typically is excited by the current, not by temperature. A comparison of the noise measured at 4 K and at the dilution refrigerator base temperature in a 0.39 μm Hall probe is shown in Fig. 4.3.

The noise level is also completely insensitive to applied fields up to 100 G, as seen in Fig. 4.4. This covers the field range generally used in our dilution refrigerator.

Assuming that noise sources in the 2DEG are localized and independent, the voltage noise density from the switching sites should add in quadrature and the total noise density should be proportional to $\sqrt{n}$, where n is the number of noise sources. If the sources are distributed evenly in the active area of the probe, n should scale linearly with the probe area, i.e. as s^2 where s is the linear size of the Hall probe. If the switching site is localized, the strength should be inversely related to the Hall probe area. Thus the hall probe field noise in this model is expected to scale as $1/s$.

A summary of the 10 Hz noise level for 11 Hall probes as a function of probe size is shown in Figure 4.5. The noise was measured at the most favorable current for each individual. The variation between individual probes is substantial, even between probes of identical size. Since individual switching centers (as seen by characteristic switching frequencies and amplitudes) are clearly identifiable in the time traces and spectra from many of the smaller probes, some random variation even between nominally identical probes is to be expected.

While the number of tested Hall probes is still too limited to draw any strong conclusions. However, the general trend appears to be that the magnetic field noise equivalent scales roughly as $s^{-1.5}$. This is in disagreement with the $1/s$ agreement argued for above; one possible explanation of the disagreement is that the switching centers are concentrated at the edges of the probe active area, possibly caused by the effects of the confining shallow etch. The size dependence in such a model may be more complicated than the simple $1/s$ dependence of the pure area model; if only the corner areas of the probes are considered, they need not scale at all with the size of the probe, thus potentially giving a constant contribution to the number of noise sources. This would give a $1/s^2$ contribution to the total noise level.

The Hall probes fabricated on the deeper IBM 2DEG (the "generation 2" probes) appear to have significantly lower field noise for equivalent size than the generation 3 and 4 probes. This is consistent with the theory that the primary noise source is state switching of two-level systems in the donor layer, since the greater distance means that a change in the electronic configuration of the donor layer will cause a smaller potential change in the deeper 2DEG. However, since a small size is essential both for spatial resolution and spin sensitivity the shallow 2DEGs will be necessary for further work.
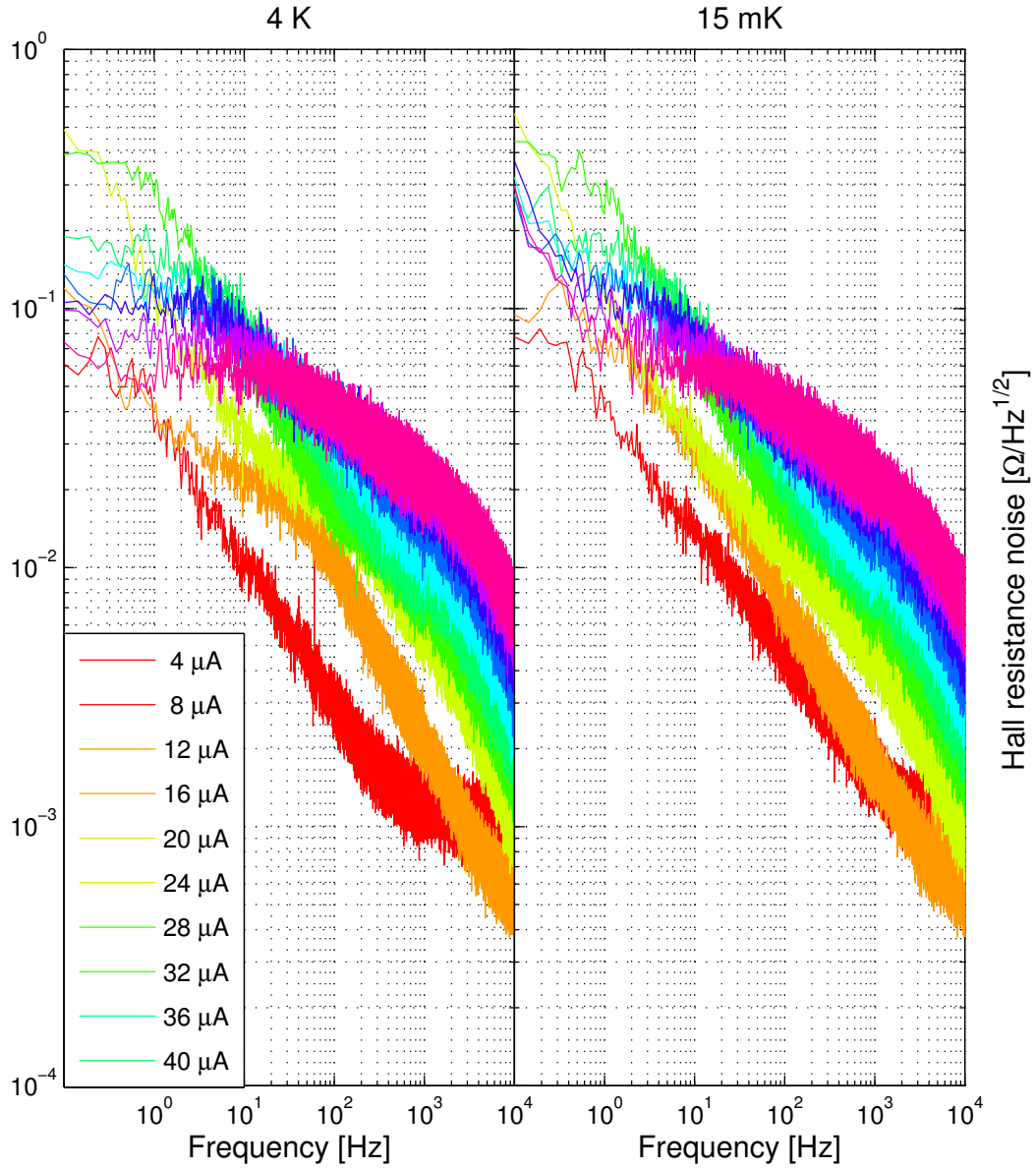
Figure 4.3: Comparison of noise measurements on a 0.39 μm Hall probe at 4 K and at 15 mK dilution refrigerator temperature. The noise level at the two temperatures is very similar. The only notable difference is that a two-level system with a characteristic frequency around 100 Hz appears to be triggered at lower currents in the 4 K measurement.
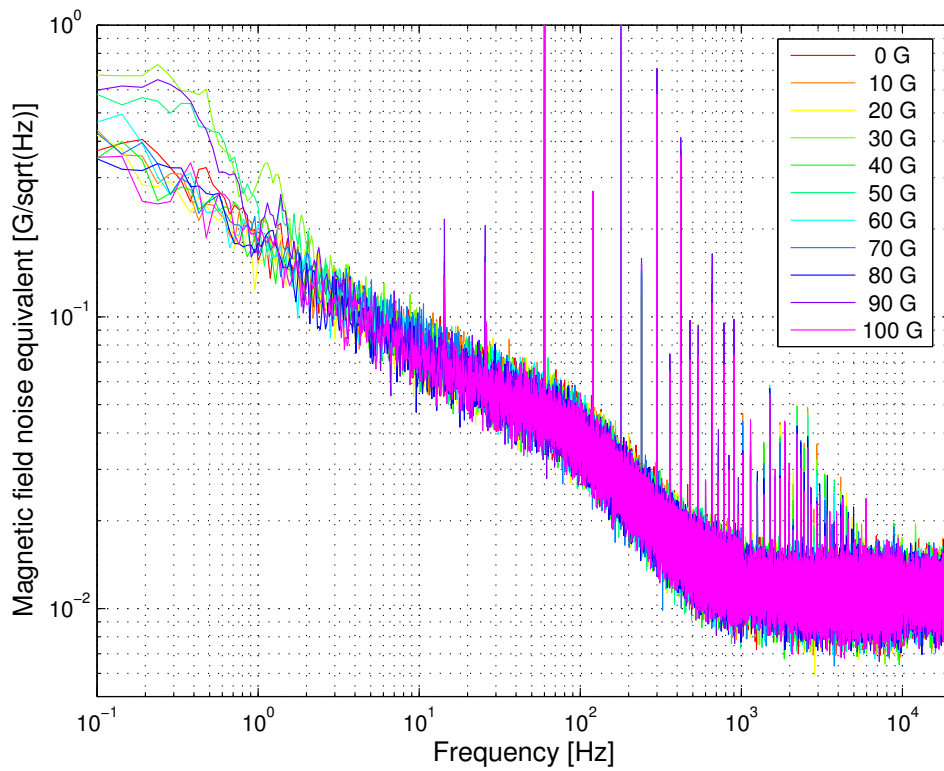
Figure 4.4: Comparison of noise measurements on a 0.39 μm Hall probe at 15 mK with a range of applied fields. There is no significant difference between the noise levels at different applied fields; the small difference seen at very low frequencies, which appears to vary randomly with the applied field, is likely due to a random variation in the number of discrete switching events.
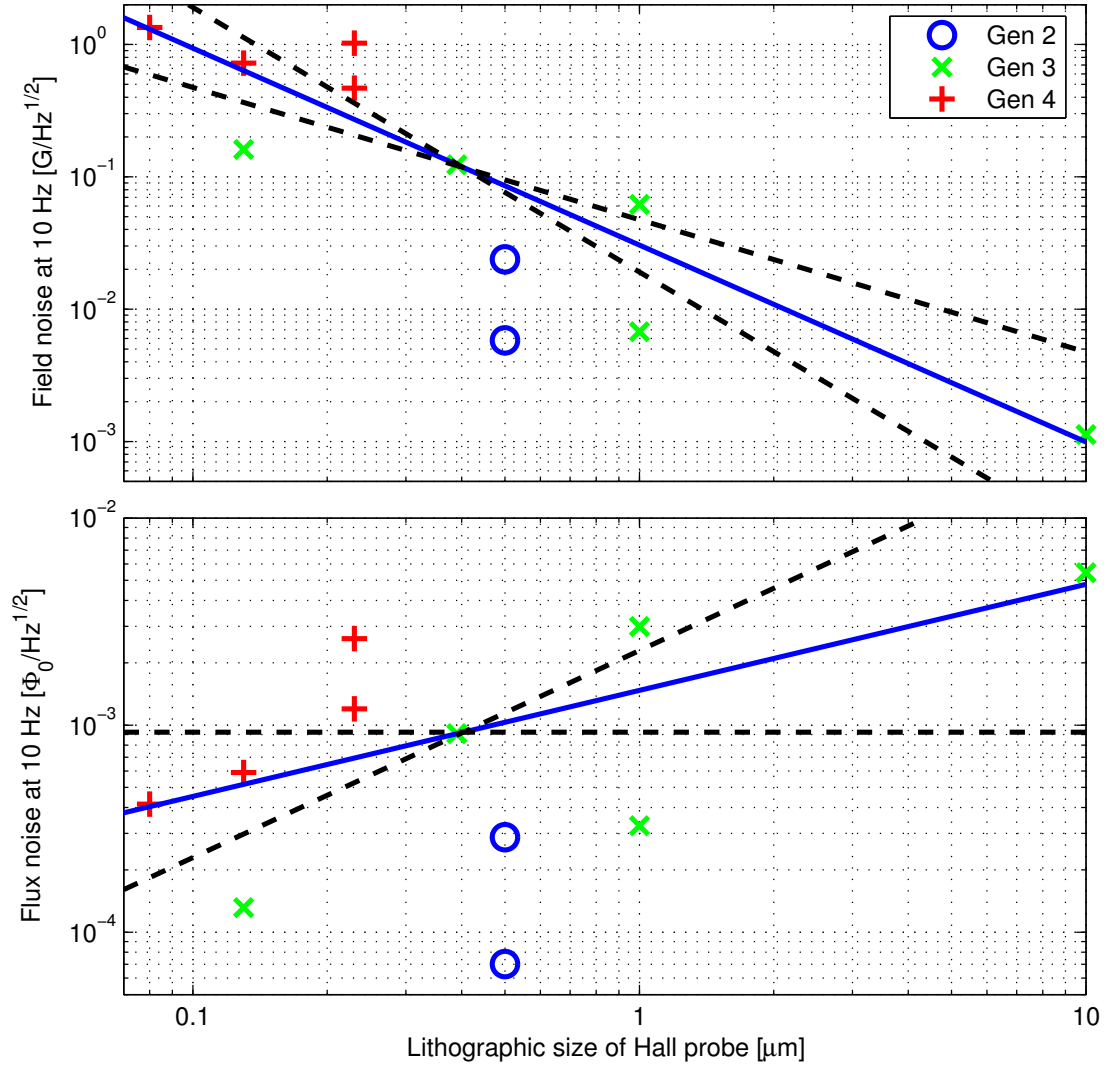
Figure 4.5: Noise level at 10 Hz for Hall probes used in the Moler lab, at the measured optimal current for each probe. Generations are explained in Table 4.1. The noise roughly appears to follow a power law. The fit is calculated using only the data for the Gen. 3 and 4 Hall probes, since the Gen. 2 probes were fabricated on a different 2DEG. The best fit for the field noise is $0.0305 \times s^{-1.48}$; fits with the exponent forced to -1 and -2 are represented by the dashed lines.

Chapter 5

Local Magnetic Measurements on Superconducting Thin Films

While the initial purpose of building the microscope described in this thesis was to do measurements primarily on mesoscopic systems and on exotic materials (such as Sr_2RuO_4, our measurements on which are described in Chapter 6), we have performed a series of measurements that are in some sense "simpler" while optimizing the instrument. These measurements have served both as a demonstration of the capabilities of the instrument and as scientific measurements in their own right. In this chapter I will describe some of these earlier measurements, their results and their implications.

5.1   Magnetic Susceptibility of Sn Disks

As an initial demonstration of the functionality of the scanner in a dilution refrigerator environment, we studied the magnetic susceptibility of 3 μm diameter Sn disks, fabricated in a square array with 30μm spacing, at temperatures down to 30mK. The sensors used in these measurements were the Generation 1 SQUIDs with 8 μm square pickup loops, as described in Chapter 3. A sketch of the measurement geometry - a dipole in a square pickup loop - is shown in Fig. 5.1. The same sample had previously been used for similar studies in another scanning SQUID susceptometer with a temperature range down to 1.2 K[Gardner *et al.*, 2001].

We applied a 200 Hz AC magnetic field by passing a 100 μA rms current throught the on-chip field coils, producing a magnetic field of about 50 mG at the pickup loop.
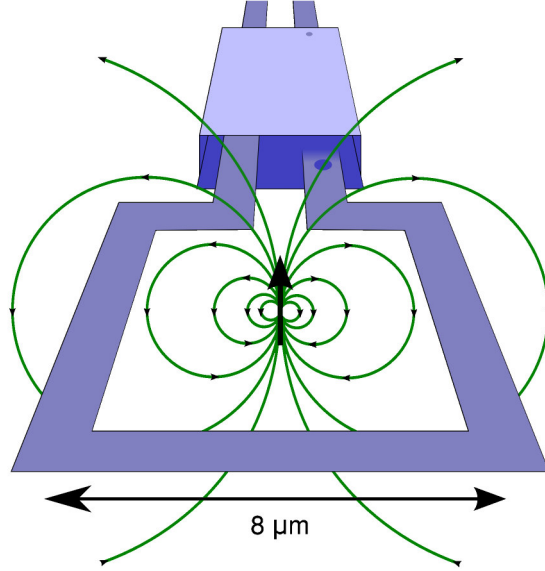
Figure 5.1: A dipole in the 8 μm pickup loop of one of our Generation 1 SQUIDs. The flux from the dipole through the SQUID must typically be calculated numerically when comparing measurement results to theoretical models.

The magnetic response was measured using a lock-in amplifier.

Modeling the superconducting disk as a dipole and the SQUID pickup loop as a square with a side of 8 μm, we could determine the scan height as well as the dipole moment of the dot. The fitting method used was to calculate the least-squares fit of the magnetic dipole moment at a given height.

The magnetic field from a dipole is

$$\mathbf{B(r)} = \frac{\mu_0}{4\pi r^3}(3(\mathbf{m} \cdot \hat{r})\hat{r} - \mathbf{m}) \tag{5.1}$$

as discussed e.g. by Jackson [1999]. Since a SQUID measures the flux threading the pickup loop, only the z component of the magnetic field will contribute to the measurement. The z component of the magnetic field from a dipole in the z direction is thus,

$$B_z = \frac{\mu_0 M}{4\pi r^3}\left(\frac{3z^2}{r^2} - 1\right). \tag{5.2}$$

The flux through a SQUID is the magnetic field integrated over the loop area. Since

dipole moment we are interested in is generated by the applied AC field, the relevant parameter is dm/dH_{az}. Thus the flux through the SQUID (modeled as a square with a side s) from the dot is

$$\Phi_s(\mathbf{r}_0) = \frac{\mu_0}{4\pi} \frac{dm_z}{dH_{az}} H_{az} \int_{-1/2s}^{1/2s} \int_{-1/2s}^{1/2s} \left(\frac{3z^2}{r^5} - \frac{1}{r^3} \right) dxdy \qquad (5.3)$$

where r_0 is the position of the center of the SQUID pickup loop relative to the dipole, and $\mathbf{r} = \sqrt{(x-x_0)^2 + (y-y_0)^2 + z^2}$. In general this integral must be computed numerically.

In this case, the pickup loop was modeled as a square with a side of 8 μm. The integral was computer numerically for a range of heights and the best-fit height was chosen by minimizing the total least-squares error. For the disk shown in the susceptibility obtained from the fit was $dm_z/dH_{az} = -5 \times 10^7 \mu_B/G$ and the best-fit height was 1.9 mum. The susceptibility number is consistent with the susceptibilities measured on disks on the same sample in previous experiments at around 2K; the measured values in that experiment ranged from -3.5×10^{-7} to $-5.5 \times 10^{-7} \mu_B/G$. A theoretical estimate using the London model in the limit of zero penetration depth gives a predicted value of the dipole moment of 7.9×10^{-7} [Gardner *et al.*, 2001]. The experimental results are in reasonable agreement with the theoretical estimates given the rather simple model. The moderate quantitative disagreement could be explained by a decreased response caused by granularity of the dot material.

Apart from demonstrating the functionality of the scanner and the feasibility of running it at low temperatures, these measurements demonstrate the power of the scanning susceptometry technique for quantitative magnetic measurements mesoscopic samples. This forms the basis on which experiments such as those proposed in Sec. 2.3.

5.2 Superconducting Transition in Tungsten Thin Films

In a second experiment, I have studied superconducting tungsten thin films using the scanning SQUID susceptometer. These samples have specific technological relevance: films identical to this one are normally used as photon detectors and energy sensors (Transition Edge Sensors) for astrophysics experiments [Cabrera *et al.*, 1998]. The sensors used here have a transition temperature as measured in transport measurements of
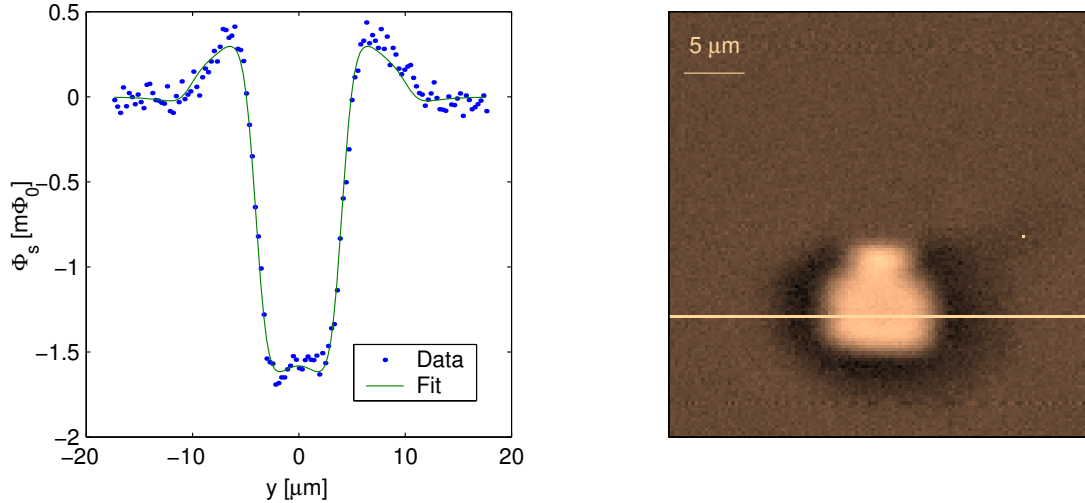
Figure 5.2: (a) Best fit of calculated SQUID response to data for a 3μm tin disk at 30mK, height=1.9μm. (b) The corresponding full image, with the cross section marked with a bright line.

146-148 mK, so by imaging this sample in the superconducting state we can demonstrate the operating capabilities of the instrument in the 100mK temperature range.

The section of the sample that was within the scan range had a large area of thin film W at the bottom. At the top of the images a set of Al rails, used for TES transport measurements, can be seen. The rails are separated by an area of bare silicon, and the top rail is comprised of two Al lines. At the very top of the images there is a small part of a second W area. A sketch of the part of the sample corresponding to out scan area is shown in Figure 5.3.

The Al current rails serve an important calibration purpose in the images. For these measurements we could calculate the height of the pickup loop above the sample by fitting the SQUID response to an applied background field with the tungsten in the normal state, since there are two Al rails (one single-wire, the other two-wire) at the top of the images. These are always superconducting in the temperature range of interest and will thus be detectable by their diamagnetic response in an applied background field.
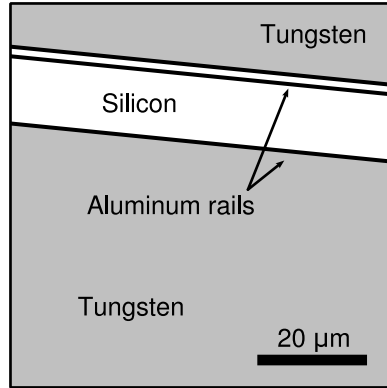
Figure 5.3: Sketch of the part of the W transition edge sensor visible in the scans.

5.2.1 Magnetometry: Vortex Imaging

The small remnant magnetic field in the dilution refrigerator, typically around 50 mG, led to the trapping of magnetic flux vortices in the tungsten film on the transition through Tc. I have imaged these vortices with magnetometry in order to study the dynamics of vortex motion in the sample. Two series of consecutive images, taken at 30 mK and 120 mK, are shown in Fig. 5.4. Each image took approximately 15 min to acquire; after one image was collected, the following scan was initiated immediately.

At 120mK the maximum flux from the vortices threading the pickup loop is only around 10 $m\Phi_0$, indicating that the vortices are extremely spread out. This indicates that the films are strongly in the thin-film limit, i.e. the penetration depth is much greater than the thickness of the W film (40 nm). At 30mK the apparent penetration depth is much smaller, as evidenced both by the greater contrast between the vortices and the background, and the increased sharpness of the vortices seen. However, the vortices are still broad and overlapping, making it very difficult to quantify the flux, and impossible to quantitatively determine the penetration depth.

Sequential images sometimes show relatively large variations in the number and placement of vortices. The vortices appear to be somewhat more likely to move at 100mK than at 30mK. However, even at the lowest temperatures reached the pinning of the vortices is weak; while there are clearly a few preferred sites for vortices, the vortices move quite freely between these sites, as indicated by the large changes between consecutive images.

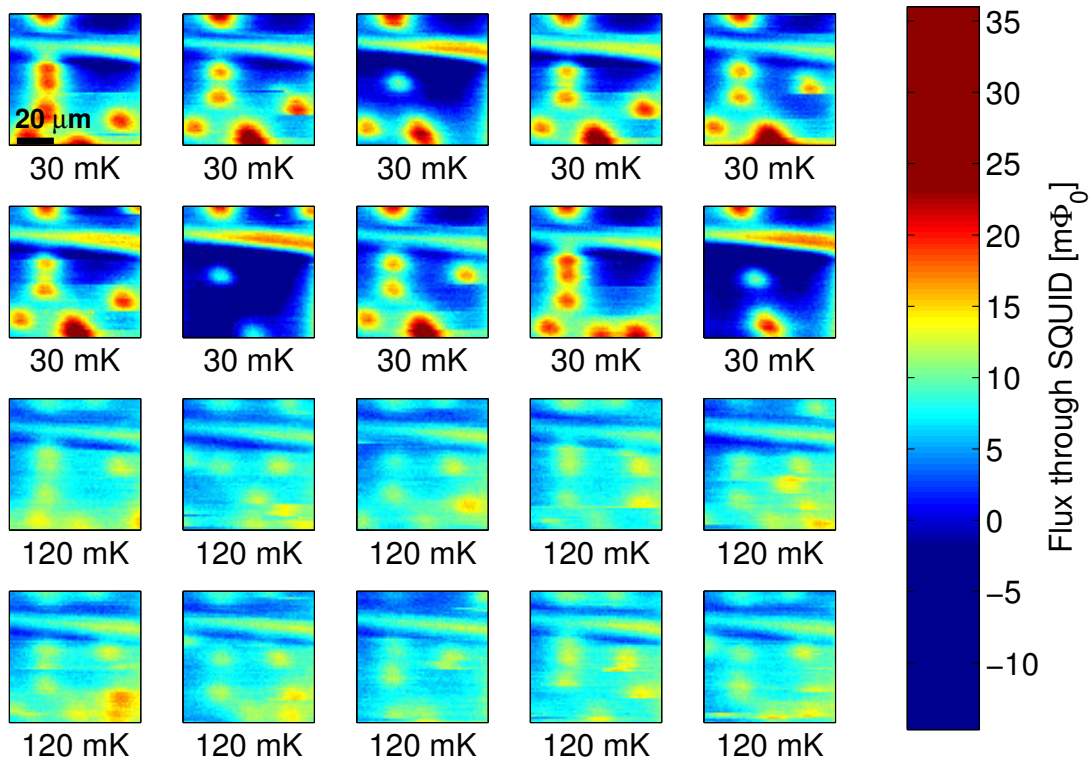Figure 5.4: Sequential magnetometry images of the TES sensor at 30 and 120 mK. The vortices are significantly more well-defined at 30 mK, indicating that λ is (as expected) much smaller at that temperature, but at both temperatures the pinning appears to be relatively weak since there are large changes between consecutive images. The sudden jumps in the figures are vortices moving during the scan.

5.2.2 Low-Field Susceptometry

In addition to the magnetometry, I have performed low-frequency, low-field susceptibility measurements on the sample in a nominal temperature range between 30mK and 150mK. The field was applied using a 50μA rms current through the field coils, giving a magnetic field of approximately 30 μG rms at the center of the pickup loop when no sample is present. The output signal from the SQUID controller is measured using a lock-in amplifier.

Up to 80mK there is no detectable decrease in the magnitude of the susceptibility of the thin films. As the temperature is increased above 100mK the sample appears quite inhomogeneous. The magnetic response of the sample decreases gradually until the sample is entirely in the normal state at 140mK. The striking width of this transition compared to transport T_c measurements on identical samples from the same wafer, which typically show a transition width of less than 2mK, can be explained by the fact that this measurement actually probes the penetration depth λ (or, essentially equivalently, the superfluid density ρ) while the transport measurements simply probe the initial formation of the superfluid condensate, at least in the low-current limit. Thus magnetic measurements are a more sensitive probe of the details of the development of the superfluid than transport measurements, while transport measurements are likely a more accurate gauge of the zero-field T_c.

The thermal contact between the sample and the mixing chamber appears to be good enough that the sample equilibrates at a given temperature as quickly as the mixing chamber does, at least at temperatures above 100mK where the temperature dependence of the susceptibility is obvious. This is demonstrated by the similarity of the images taken while ramping the temperature up and down; no hysteresis is noticeable to within less than 10 mK.

5.2.3 Susceptometry in a Background Field

In order to study the effect of a magnetic background field on the thin film we did susceptometry measurements similar to those described above but with DC offset current applied to the field coils in addition to the AC excitation current, thereby measuring $\lambda(H_{\text{background}})$. Images were taken in a range of different temperatures from 70 mK to 100 mK.
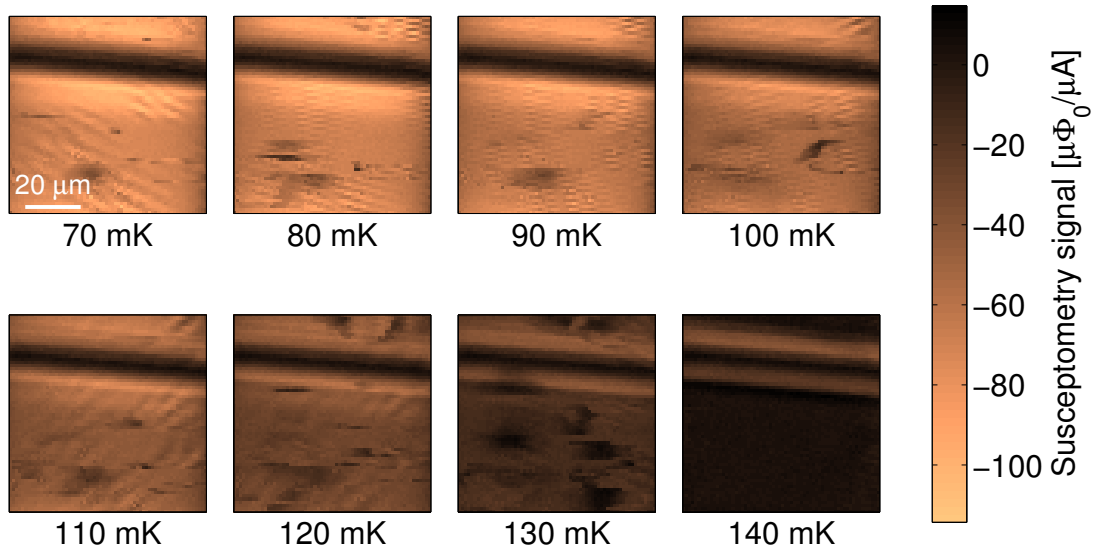
Figure 5.5: Susceptibility images the TES film. The small-length-scale variations in the susceptibility may be caused by the SQUID occasionally touching and locally heating the sample and may thus not be actual variations in the sample.
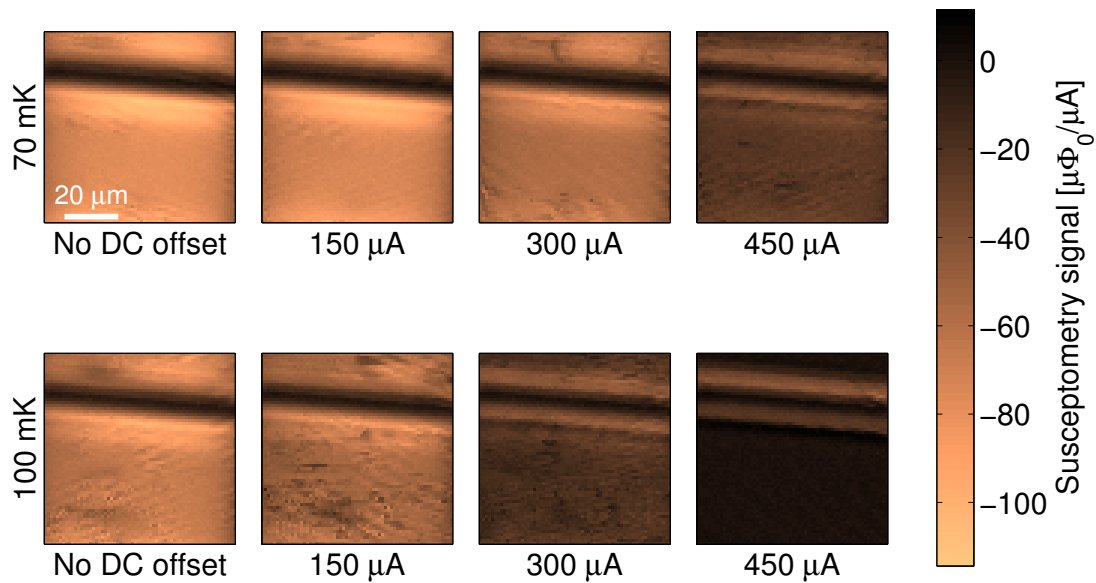

Figure 5.6: Susceptometry images with a background field applied using the field coils. The applied AC current for the susceptometry is $50\mu A$. The DC offset current though the field coil is indicated on each scan.

The effect of applying a DC background field appears similar to that of raising the temperature; there is no discernible difference between the images at 70mK in a background field caused by running 600μA through the field coils and the zero-background-field normal-state images at 140mK. There is very little difference in the behavior between 70mK and 80mK, but at 100 mK H_c is clearly lower as the superconductivity is suppressed completely already with an offset current of 400μA through the field coils. The behavior is consistent with the applied field suppressing the T_c of the superconductor. It would be useful to compare these results to T_c measurements using transport techniques in an applied background field; unfortunately we are not aware of any such measurements.

A simple conclusion that can be drawn from these experiments is that when using thin-film transition edge sensors it is very important to keep them in a magnetically well-shielded environment in order to minimize noise from flux motion. In order to quantify the effects it would be interesting to do simultaneous scanning magnetometry and transport measurements, to investigate whether the noise measured in transport can be related to vortex motion.

Chapter 6

Search for Spontaneous Time-Reversal Symmetry Breaking in Sr$_2$RuO$_4$

In this chapter I describe a major part of my experimental work: studying the properties of the superconductor Sr$_2$RuO$_4$, in particular searching for signs of time-reversal symmetry breaking (TRSB) using scanning SQUID and Hall probe microscopy.

These measurements have not resulted in any detection of magnetic signals that can be understood in terms of TRSB. This appears to stand in contrast to the theoretical estimates of the expected magnetic fields. However, there are still opportunities to explain the results even for a TRSB superconductor, and I will discuss how to tie up these loose ends with a combination of further theoretical and experimental work. A brief account of these measurements has been published in a previous paper [Björnsson et al., 2005].

6.1   Sr$_2$RuO$_4$: A spin triplet superconductor

Strontium ruthenate, Sr$_2$RuO$_4$, has been studied extensively since its superconducting properties were discovered in 1994 [Maeno et al., 1994]. Mackenzie and Maeno have recently reviewed the experimental situation [Mackenzie and Maeno, 2003].

The material was the first non-cuprate superconductor with a layered perovskite

structure to be discovered, eight years after the discovery of high-T_c in the cuprates. There has been great effort, both experimental and theoretical, to identify the structure of the energy gap [Mackenzie and Maeno, 2003].

Soon after the discovery of superconductivity in Sr_2RuO_4, it became clear that it had unconventional properties. In particular, several strong pieces of evidence are available for Sr_2RuO_4 being a spin-triplet superconductor, as opposed to the spin-singlet pairing in both s- and d-wave superconductors.

The strongest early evidence for triplet pairing came from NMR Knight shift measurements by Ishida *et al.* [Ishida *et al.*, 1998]. The Knight shift directly measures the spin susceptibility, which indicates the effective field at an atomic nucleus from the electrons, and these measurements showed that the Knight shift was unchanged across the superconducting transition. In an s-wave superconductor, the Knight shift is generally expected to vanish in the superconducting state. The reason for this is that the Knight shift is caused by spin polarization related to Zeeman splitting, and in a spin-singlet superconducting state the condensate consists of Cooper pairs with zero spin. (This is also related to one way a magnetic field can destroy superconductivity: when the energy gained by forming the condensate is smaller than the Zeeman splitting, the condensate is no longer energetically favored.) In contrast, a triplet pairing state where electrons with equal spins are paired can exhibit a net polarization, just as the normal state. Thus it is expected that for such a state the Knight shift will be unchanged when passing through the superconducting transition. This exactly matches the results of Ishida *et al.* and is in general inconsistent with a singlet order parameter. However, there are experimental counterexamples: Vanadium is an elemental s-wave superconductor which also shows no change in the Knight shift across the superconducting transition [Noer and Knight, 1964]. One possible reason other than a p-wave pairing symmetry for a constant Knight shift is strong spin-orbit coupling [Anderson, 1959].

More recently, further and possibly more direct evidence for an odd-parity wavefunction, which requires triplet pairing, has been presented in the form of phase-sensitive measurements by Nelson *et al.* [Nelson *et al.*, 2004] They have fabricated SQUIDS where they have connected opposite faces of Sr_2RuO_4 single crystals using the s-wave superconductor InAu to complete the loop. By studying the magnetic flux dependence of the SQUID, they have determined that the wavefunction undergoes a sign change between opposite sides of the crystal. This type of SQUID is also known as a "π

SQUID" since the loop includes a spontaneous π phase shift. This is very strong evidence for triplet pairing symmetry, since all singlet wavefunctions have the same sign under mirror inversion.

6.1.1   Time Reversal Symmetry Breaking

In addition to being a triplet superconductor, there is some evidence that the wave function is in fact a two-component time reversal symmetry breaking wavefunction. The main experimentally detectable signature of a time reversal symmetry breaking wavefunction is that there is a spontaneous current circulating around superconducting domains, causing local magnetism. The main evidence for this to date is the μSR (muon spin resonance) measurements by Luke *et al.* [Luke *et al.*, 1998] μSR effectively measures local magnetic fields in the sample, and they report a signal characteristic of "a broad distribution of fields arising from a dilute distribution of sources", concluding that these localized magnetic fields are evidence for TRSB.

Further supporting evidence for a two-component order parameter comes from the details of the flux lattice as observed by Kealey *et al.* with small-angle neutron scattering [Kealey *et al.*, 2000]. They find a square vortex lattice throughout the magnetic field range where there is a vortex lattice which is generally not compatible with a conventional superconductor, and the details of the magnetic field structure agree with the predictions of a two-component Ginzburg-Landau model.

6.1.2   An explanatory cartoon of TRSB

TRSB can arise in superconductors where each Cooper pair carries a finite angular momentum, and where the Cooper pairs are locked together with the same orientation, as illustrated conceptually in Fig. 6.1. There may be domains with opposite orientation of the angular momentum vectors, conceptually similar to magnetic domains in a traditional ferromagnet.

The magnetic moments are in this case caused by the orbital angular momentum of the Cooper pairs. Internally in a domain the motion of neighboring pairs cancel out and give no net current flow, but there is no such cancellation at the edge of a domain. This leads to a net current within a coherence length of a domain edge, since ξ defines the length scale of a Cooper pair.
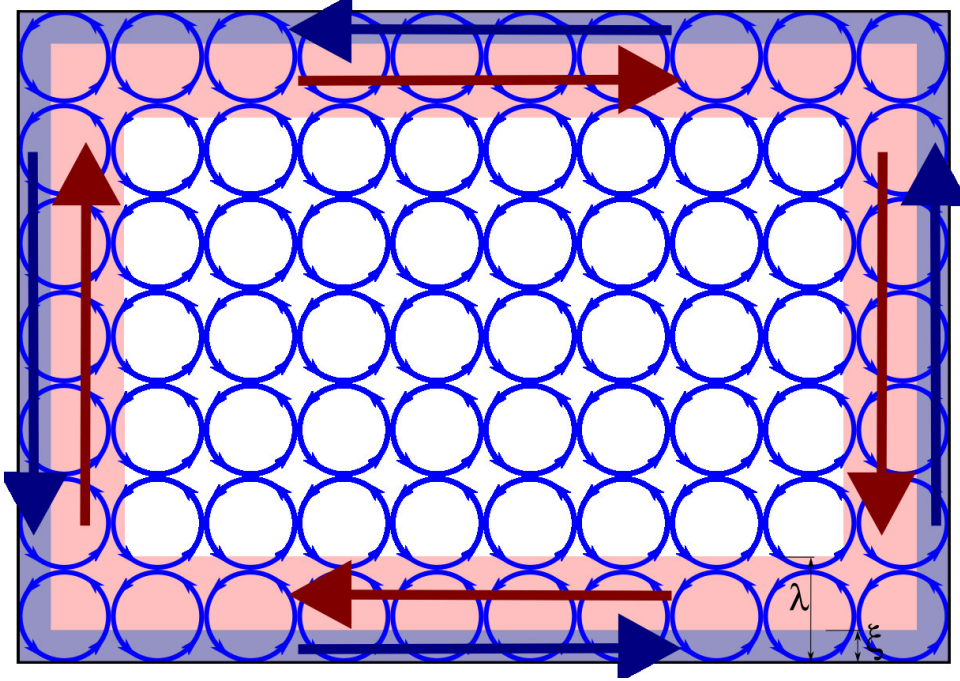
Figure 6.1: A cartoon for explaining the current flows and magnetic fields associated with TRSB in a superconductor with all electrons paired in L=1 Cooper pairs. Modeling the pairs as orbiting electrons, in the interior there is no net current since neighboring electron pairs cancel out; however, at an edge this cancellation is broken and there is a current within a distance ξ from the surface, flowing as indicated by the blue arrows. The magnetic field generated by this current is canceled by a counterflowing current on the length scale of λ because of the Meissner effect.

However, since this is a superconductor magnetic fields are screened out through the Meissner effect. The manifestation of the effect is that a screening supercurrent flows in a region limited by the penetration depth λ, such that the field in the interior of the domain is zero. This means that there are counterflowing currents on somewhat different length scales around every domain.

6.1.3   The Order Parameter

A precise determination of the gap structure in Sr_2RuO_4 is yet another important component in understanding the superconducting properties of the material. The issue has been the subject of significant controversy, since thermodynamic probes such as
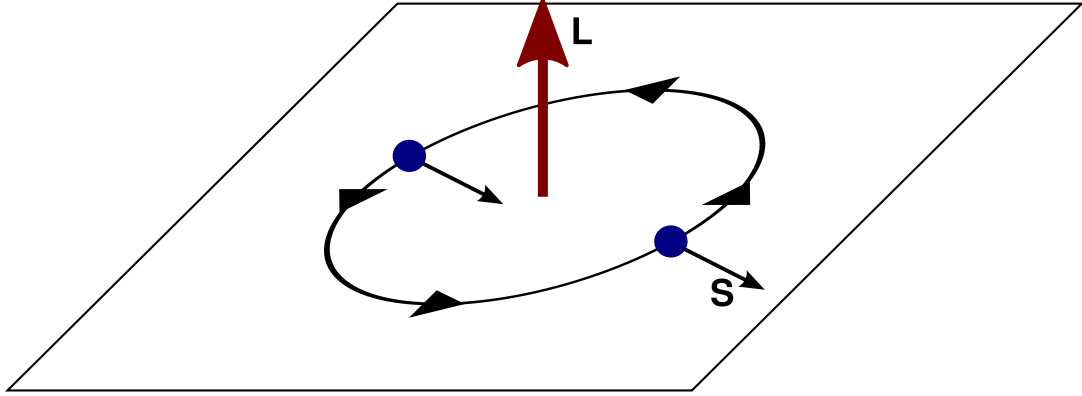
Figure 6.2: A real-space visualization of a $k_x + ik_y$ class order parameter. The blue dots are electrons. S indicates the electron spin and L indicates the orbital angular momentum of the Cooper pair.

specific heat [Nishizaki *et al.*, 1999] and thermal conductivity measurements [Tanatar *et al.*, 2001a] have revealed a power-law temperature dependence of the quasiparticle density, indicating that the gap has line nodes, while early measurements using directional probes such as magnetothermal conductivity [Tanatar *et al.*, 2001b; Izawa *et al.*, 2001] have not revealed any in-plane gap anisotropy. Also, the order parameter which is most readily compatible with the symmetry properties and TRSB as discussed above is described by the $\boldsymbol{d}$-vector representation $\boldsymbol{d}(\boldsymbol{k}) = \hat{z}\Delta_0(k_x + ik_y)$, which has a nodeless gap.

Recent work by Deguchi *et al.* using specific heat measurements varying the orientation of the applied magnetic field have significantly clarified the details of the gap structure [Deguchi *et al.*, 2004a,b]. These measurements, which extended the temperature range to much lower temperatures than the previous thermal conductivity measurements (120 mK *vs.* around 400 mK), show that there is indeed an in-plane anisotropy to the gap, with vertical line nodes in the β band in the [110] direction. The anisotropy was only clearly detectable at temperatures below 300 mK, which explains the discrepancy with the earlier measurements. The measured node orientation is consistent with the nodes being caused by antiferromagnetic interactions suppressing superconductivity. The γ band, which is the active superconducting band, has strong anisotropy (the gap is significantly reduced in the k_x and k_y directions) but no actual

nodes. The gap structure of the γ band can be explained by the TRSB order parameter described by $\boldsymbol{d}(\boldsymbol{k}) = \hat{z}\Delta_0(\sin(ak_x) + i\sin(ak_y))$. This gap structure, with nodes in the β band and a γ band gap belonging to the $k_x + ik_y$ class, is consistent with the full body of experimental data on the gap structure of Sr_2RuO_4.

A real-space visualization of a $k_x + ik_y$ class order parameter is shown in Fig. 6.2. The spins of the two electrons forming a pair are parallel and their orientation is locked to the ab plane of the material, with the orbital moment L of the pair aligned with the c axis.

6.2   Detecting TRSB Using Local Magnetic Measurements

One of the most dramatic consequences of the order parameter described above is its time-reversal symmetry breaking (TRSB) nature. This can be probed by measuring local magnetic fields in the sample. An experiment that can directly probe the spatial distribution of the expected spontaneously generated magnetic fields is one of the last missing pieces in the puzzle of the Sr_2RuO_4 wavefunction. We have sought to perform just such an experiment.

There are three magnetic signatures of TRSB that could be observable by local magnetic imaging:

Edge currents. In a single crystal with no domains (e.g., the order parameter throughout the crystal would be either $k_x + ik_y$ or $k_x - ik_y$), there should be an edge current within a coherence length of the edge, and a counter-circulating shielding current within a penetration depth [Sigrist and Ueda, 1991; Kwon *et al.*, 2003]. Kwon *et al.* argued that in Sr_2RuO_4, this effect would produce a net magnetic flux of 2.6 Gμm per unit length of the edge [Kwon *et al.*, 2003]. These calculations do not take the possibility of chiral domains into account; they assume a single chiral domain which is large compared to the measurement device. In order to make more accurate predictions, full Maxwell-London calculations taking the domain size into account may be necessary.

Currents at domain walls. Matsumoto and Sigrist argued that domains are energetically unfavorable, and are only found because of domain wall pinning [Matsumoto and Sigrist, 1999]. In principle the domain size may range from the sample size to the coherence length, $\xi_{ab} = 66$ nm. Very different patterns of current flow would result depending on whether the domains are smaller or larger than the penetration depth,

$\lambda_{ab} \approx 160$ nm. We are not aware of quantitative theoretical predictions on the expected magnetic signal from domain walls. Kwon *et al.* actually mention domain walls as a source of magnetic fields, but merely note that there should be no net flux from a domain wall, and thus they are not likely to be detectable using a SQUID because all current SQUIDs are large compared to the relevant length scales of field cancellation (λ and ξ).

Defects. Currents with counter-circulating shielding currents are also expected to flow around defects.

In previous work, Tamegai *et al.* studied local magnetization at the edge of a sample using a stationary $5 \times 5 \mu m^2$ Hall probe [Tamegai *et al.*, 2003]. They detected no spontaneous magnetic fields associated with edge currents, although they did report anomalies in the magnetization hysteresis loops that they suggest indicate the presence of chiral domains.

Simultaneously with the work reported in this thesis, Dolocan *et al.* has reported observing coalescing vortices forming flux domains. They suggest that this observation indicates the presence of topological defects such as domain walls resulting from unconventional chiral superconductivity [Dolocan *et al.*, 2004]. However, they did not detect, nor were they explicitly looking for, magnetization signals from edges and defects.

I have improved on the earlier experiments in the field primarily by improving the magnetic field sensitivity by using smaller and/or more sensitive probes, and by imaging a sample specifically patterned to provide a detectable signal.

6.2.1   Samples

The pure Sr_2RuO_4 samples used were single crystals, grown by the research group of Yoshi Maeno utilizing a floating-zone method [Mao *et al.*, 2000]. T_c as determined by bulk AC susceptibility measurements on pieces from the same crystal bar was 1.422 K (transition midpoint) with a transition width of 24 mK; this agrees with the less precise observations of T_c – close to 1.5 K – in our scanning measurements. The temperature measurement in the scanning experiments is more coarse-grained since I focused on imaging the sample at a set of different temperatures as opposed to carefully following the temperature dependence at a single point; since imaging the sample takes a significant amount of time, and the temperature must be stable during a scan (implying that the refrigerator must be stabilized at the temperature before the measurement is
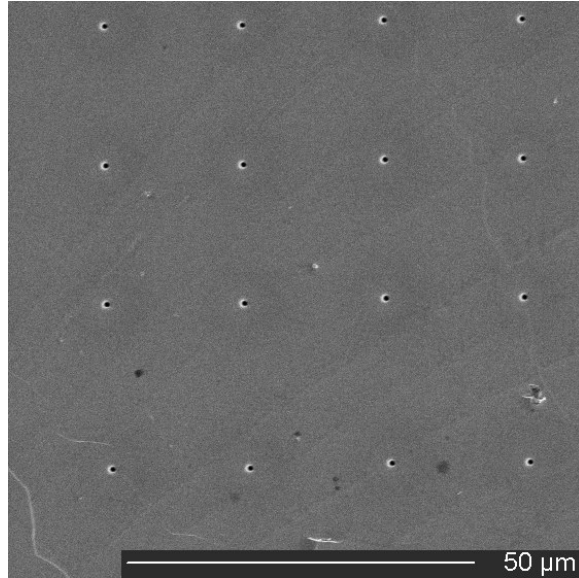
Figure 6.3: An SEM image of the Sr_2RuO_4 crystal used for the Hall probe imaging. An array of holes was milled in the sample using a FIB. The hole spacing is 20 μm.

started), it is not feasible – and generally not particularly interesting – to collect imaging data spaced as closely in temperature as would be typical for a bulk susceptibility measurement.

The first imaged sample was imaged as-cleaved without any further processing. It was scanned with a SQUID sensor with a 4 μm pickup loop. I prepared a second sample by patterning a cleaved crystal with an array of approximately 1 μm diameter pits with a spacing of 20 μm using a Focused Ion Beam (FIB) with 30 kV acceleration voltage of Ga^+ ions. The depth of the pits is estimated to be around 1 μm; however, for a precise measurement of the depth the sample would have to be sliced apart e.g. with an FIB. Since this would destroy the sample I have not done so at this point in time. An SEM image of this sample is shown in Figure 6.3. Each sample was mounted in silver epoxy and connected to the mixing chamber baseplate of the dilution refrigerator with a copper wire for thermal contact.
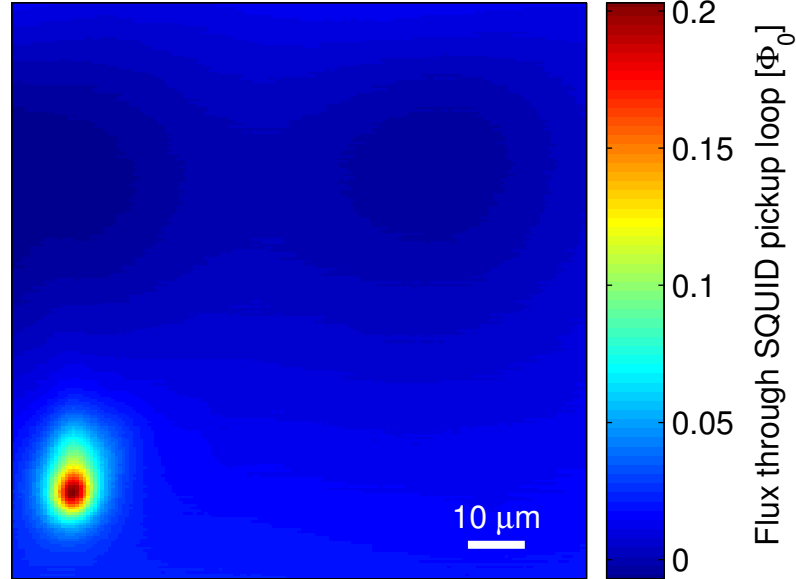
Figure 6.4: Scanning SQUID image of a single crystal of Sr_2RuO_4 with a single vortex within the field of view. The only other magnetic signals visible are a smoothly varying background.

6.2.2 SQUID Imaging of an As-Cleaved Crystal

SQUID images of an unpatterned sample were acquired at a height of approximately 2 μm above the sample surface. The most prominent feature in most images were magnetic vortices. These all appeared completely conventional, carrying 1 Φ_0 of magnetic flux to within calibration errors which may be on the order of 10%. An image with a single vortex is shown in Fig. 6.4.

In images where the background field was carefully compensated, so that there were no vortices in the field of view, shown in Fig. 6.5, we detected a smoothly varying background and a few dipole-like artifacts that were present even at 4 K and thus must be unrelated to the superconductivity of the Sr_2RuO_4 sample. The smooth background may be caused by pickup from a secondary pickup loop, which was extended over the edge of the sample. The total magnitude of the background variation is on the order of 50 mG, and the noise level in the measurements, measured as the rms difference between adjacent pixels with 0.6 μm spacing, is 0.45 mG (equivalent to approximately
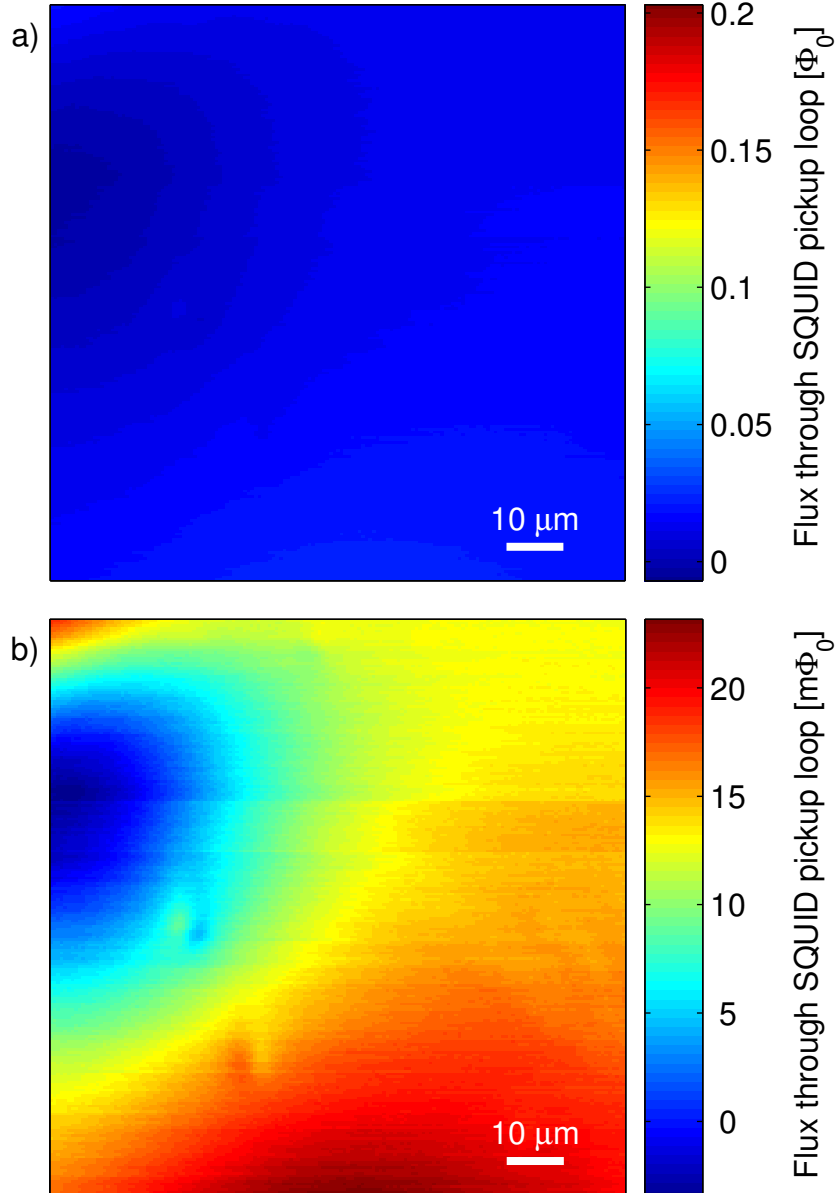
Figure 6.5: Scanning SQUID image of the same area of a Sr_2RuO_4 crystal as in Fig. 6.4 but with the background field compensated so that there are no vortices. In (a), the color scale is the same as for Fig. 6.4, while (b) is the same image with the color scale stretched to enhance detail. The only visible features apart from the smooth background (which may be caused by the secondary pickup loop hanging off the sample) are dipole-like structures that are visible both in the superconducting and normal state (measured at 4 K) and thus appear to be magnetic particles stuck on the surface.

0.4 mΦ_0 rms flux noise).

For a sensor of this size, the flux at an edge through the sensor predicted by Kwon *et al.* [Kwon *et al.*, 2003] is around 0.5 Φ_0. The scanned area did not include any sharp edges; however, there were shallow steps within the scan area which should to some extent be similar to edges. In order to make detailed predictions of the signal level, significantly more detailed calculations which take the geometry into account would be necessary.

6.2.3 Hall Probe Imaging of a Hole-Array Sample

The next experiment used a Hall probe with an active area of 0.5 μm$\times$0.5μm to image a crystal with FIB-milled holes (Figure 6.3). This experiment had three improvements that allow the data to be compared semi-quantitatively with theory. First, the FIB-milled holes provide edges throughout the imaged area. Second, the Hall probe has only a single active area and therefore does not suffer the same systematic background errors. Third, the Hall probe has a smaller active area than the SQUID and can be scanned at a lower height, providing higher spatial resolution.

A low-field Hall probe scan of the sample is shown in Figure 6.6. The image is completely free of features other than a few isolated trapped vortices, such as commonly appear in low-field, low-temperature magnetic scans of type-II superconductors. These vortices appear to be entirely conventional, carrying a magnetic flux of $\frac{h}{2e}$ within 10% error, as determined by integration of the measured local magnetic field. The apparent lateral extent and shape of the vortices is limited by the sensor scan height. Fits to these images of isolated individual vortices determine the probe height to be $1.2\pm0.2\mu$m above the surface. Thus our spatial resolution is limited by the height of the probe above the surface, not the probe size itself [Kirtley *et al.*, 1999].

The dominant noise source in these measurements is Hall probe $1/f$ noise. To minimize this noise, we used the standard scanning microscopy technique of scanning relatively quickly (2 s/scan line) and averaging multiple scans, subtracting the background level of each line and removing sudden jumps. For the image in Figure 6.6, 80 scans were averaged. The resulting background noise has an rms value of 35 mG, with no sign of the array of holes milled in the sample or any other features.
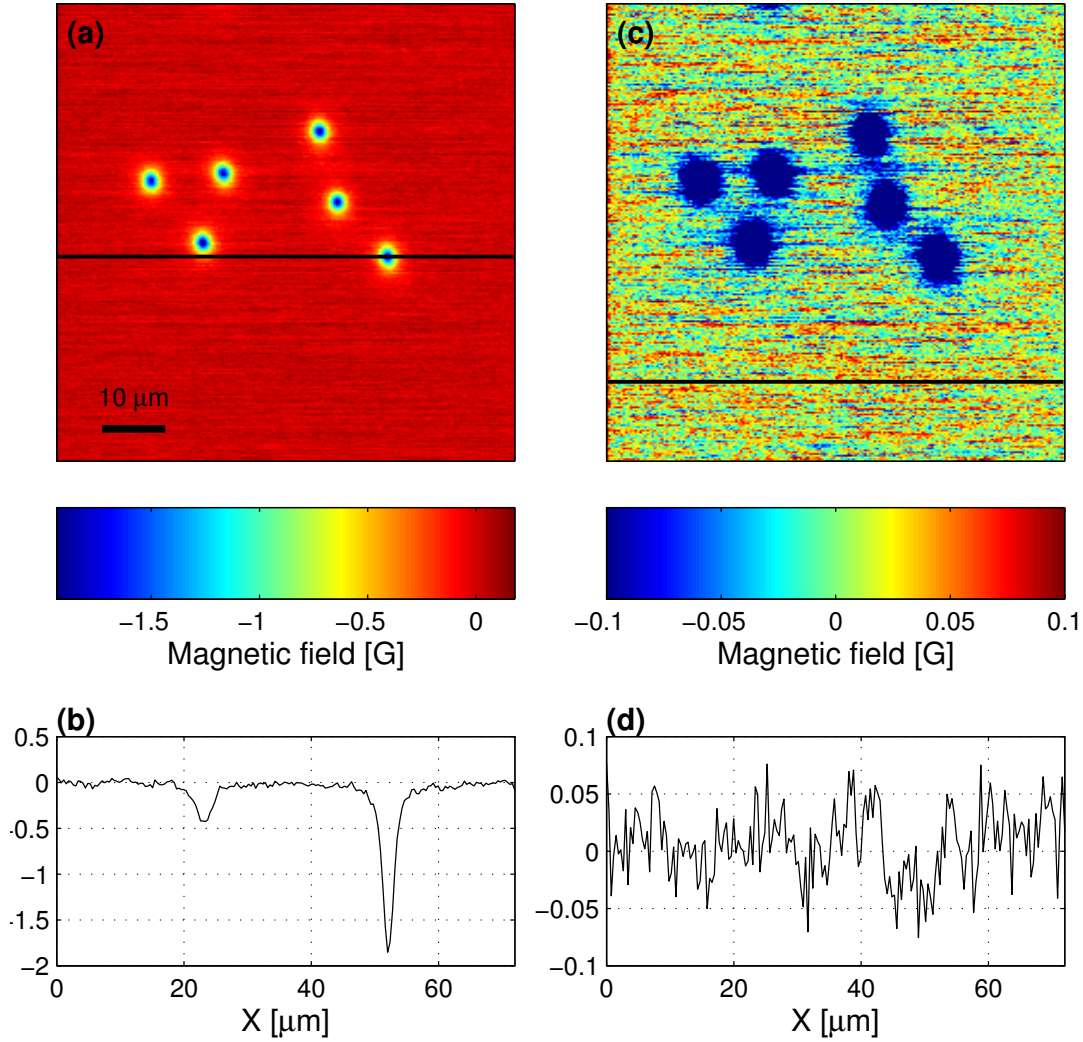
Figure 6.6: Scanning Hall probe image of the sample shown in figure 6.3, cooled in a background field of ∼25 mG. The background has been line normalized to remove $1/f$ noise. (a) Image with a color scale showing the full measured magnetic field range. Isolated trapped vortices dominate the image. (b) Cross section taken along the black line in (a). (c) Image with an expanded color scale, showing that there are no obvious features in the noise. (d) Cross section taken along the black line in (c).

Figure 6.7: Hall probe scans in varying magnetic fields. The vortices appear to form lines that are spaced much more closely than the FIB-milled hole pattern. There are also regions at the top and right-hand side of the imaged area in which the density of vortices is much lower than the average in the images.
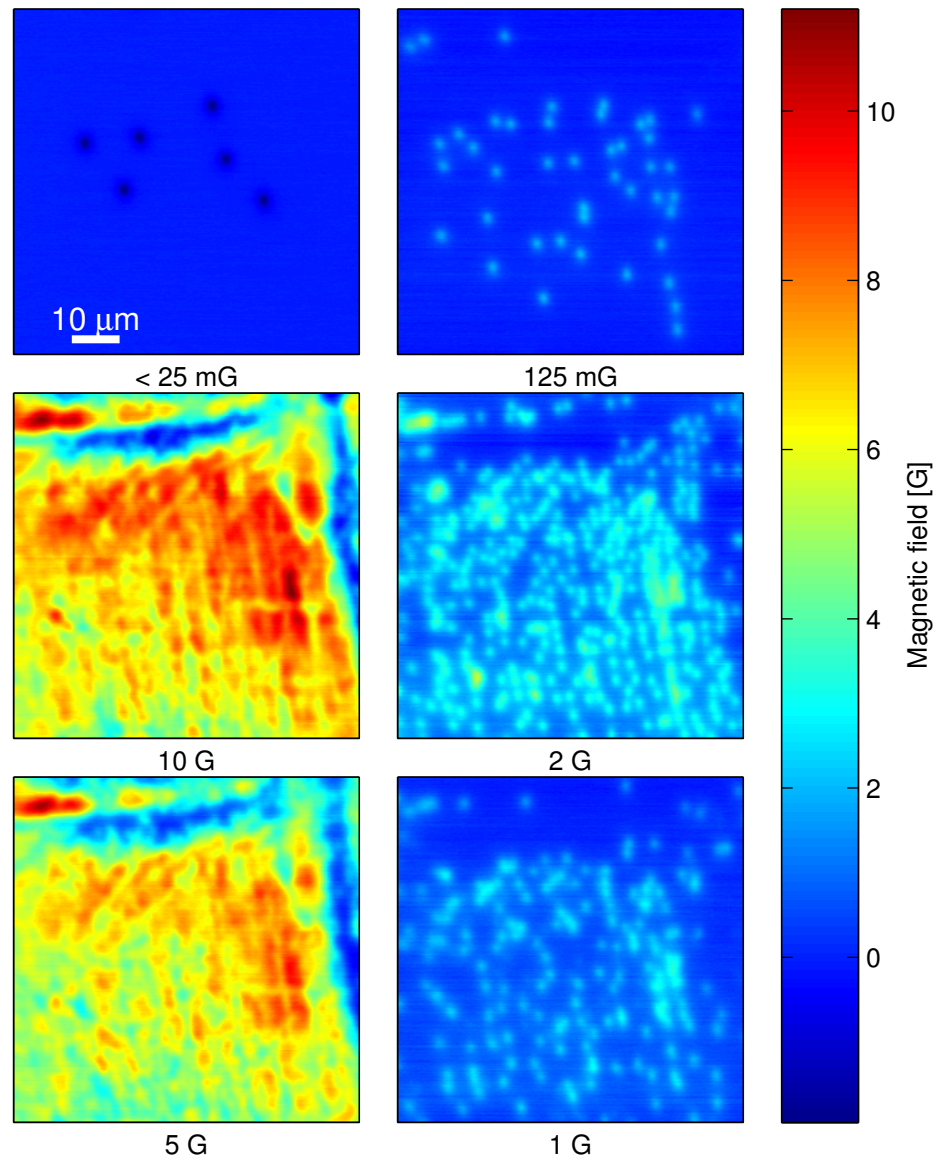
6.2.4   Hall probe data in applied background fields

Scanning Hall probe images were also made after cooling the sample through T_c in fields up to 10 G, staying well below H_{c1} (Fig. 6.7). In this field range, we would expect to see isolated trapped vortices. The most striking feature in the images is that the vortex distribution looks very inhomogeneous. In addition, in the densely populated areas, the vortices appear to form lines. We have not observed (optically or using SEM) any imperfections or structure in the crystal on length scales that correspond to these lines, although we can not entirely rule out some kind of damage, possibly from the FIB patterning; however, the length scale of the features does not appear to correspond to the hole array row and column spacing. As seen in figure 6.8, the vortices appear to be pinned in the same areas at different field levels, even though the sample was thermally cycled above T_c between the measurements. This indicates that the vortex pinning structure is related to some structural property of the sample, or at least some property that is preserved across thermal cycling through T_c.

The vortex structures that we detected in the measurements in moderate fields are similar to the structures seen by Dolocan *et al.* [Dolocan *et al.*, 2004] in that the vortices group already in small perpendicular fields. However, we find that the vortices order in lines without any applied in-plane field (other than any residual field in the magnetically shielded dewar or an in-plane field caused by the field inhomogeneity of our magnet, both of which are small compared to the applied perpendicular field; the in-plane field is estimated to be a few percent of the applied field, or a few tens of mG in nominal zero applied field) while Dolocan *et al.* see the vortex pattern evolving from irregularly shaped flux domains to a line-like structure with increasing applied in-plane fields. In order to get a line-like structure they need to apply in-plane fields which are much larger than the applied perpendicular field. There is a possibility that sample differences play a significant role; they report a T_c of 1.35 ± 0.05 K, which is lower than the T_c of the sample I have studied. This may be relevant, since the T_c of Sr$_2$RuO$_4$ is very sensitive to sample purity [Mackenzie and Maeno, 2003].

6.3   Comparison with Theoretical Predictions

Given that we have not detected any magnetic signatures of TRSB in our scanning measurements, it is important to compare the theoretical expectations of spontaneous
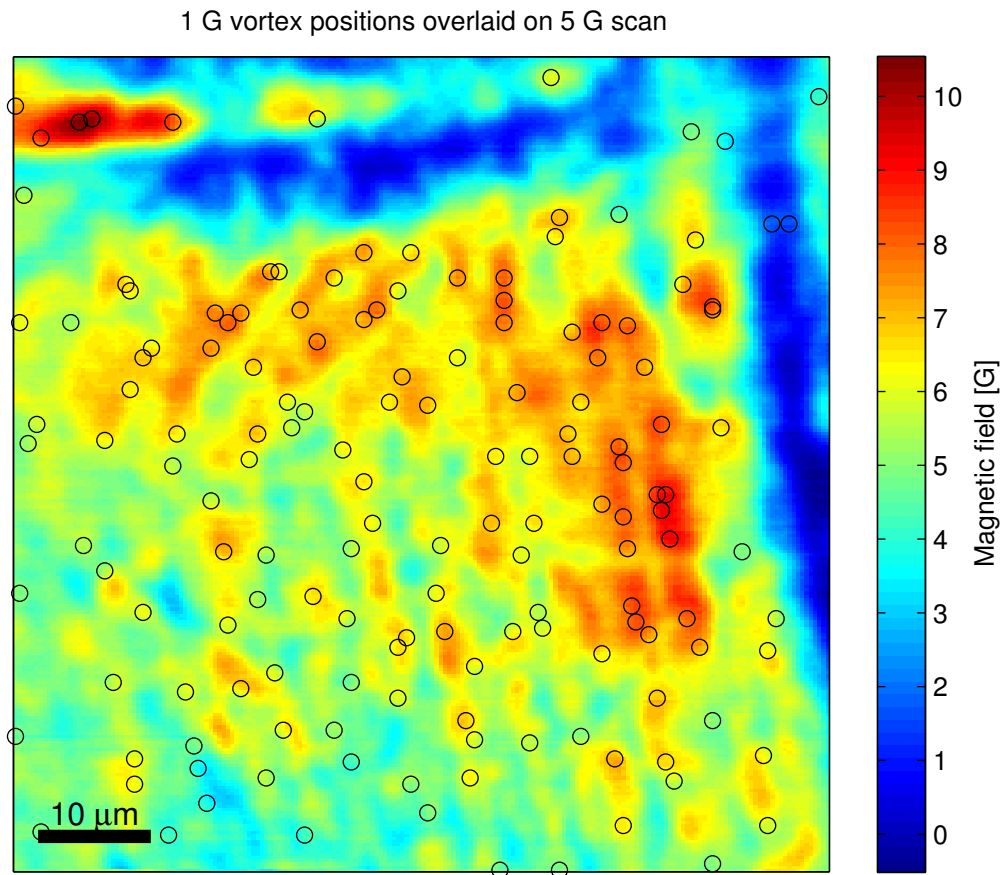
Figure 6.8: Overlay of the vortex positions in the 1 G scan on the 5 G scan data; the data is the same as in Fig. 6.7. The vortex positions in the 1 G scan are marked with circles. The vortices tend to line up in the same areas even though the sample has been thermal cycled above T_C between the measurements.

currents with the limits set by our measurements.

One way to quantify the non-detection of edge currents is to consider the field generated by a current loop. A circulating current around a 1 μm diameter hole would give a measured signal of approximately 1 mG/μA at our measurement height. Thus the measurements set a limit on net circulating currents of less than 35 μA. The total edge current and counter-circulating shielding current could each be considerably larger.

We can also compare our non-observation of edge currents at micro-holes to the calculation by Kwon, Yakovenko, and Sengupta for magnetic flux resulting from edge currents [Kwon *et al.*, 2003]. Naïvely, the predicted magnetic flux of 2.6 Gμm per unit length of edge should fall off like the inverse of the height, leading to a magnetic field of slightly under 1 G at a height of 1 μm. Although a self-consistent calculation including Meissner effects in three dimensions for our specific geometry is necessary to make truly quantitative comparisons, this naïve estimate for TRSB is well above our noise level of 35 mG.

Our non-observation of edge currents could be explained in three ways: either the preceding estimate for TRSB edge currents is insufficient; or there are multiple chiral domains, on the length scale of the micro-holes; or the material is not TRSB. It is therefore important to understand the possible structure and magnetic signature of chiral domains.

If the size of the domains is much larger than λ_{ab}, the magnetic moment should be shielded in the interior of the domains and the only measurable signal should come from domain walls. Both the shielding currents and the neighboring domains would lead to a cancellation of the signal when measured at a height which is large compared to ξ_{ab} and λ_{ab}, but setting quantitative limits on currents at domain walls requires a specific theoretical model.

If the size of the domains is on the order of λ_{ab} or smaller, the magnetic moment will not be fully shielded in the interior of the domain. Signals of opposite sign from neighboring domains will cancel out rapidly with sensor height or size. The signal at a given height from many domains can be estimated as follows. If the magnetic field at the sample surface is Fourier transformed into its spectral components $B_z(\vec{k}, z = 0)$, where $\vec{k}$ is the spatial wavevector in the plane of the sample surface, then the amplitude of each spectral component at the height z above the surface will be decreased by a factor of e^{-kz} [Roth *et al.*, 1989]. The actual measurable field would be strongly dependent on

the distribution of domain sizes: a perfect checkerboard pattern with identically-sized domains would give extremely rapid cancellation, but a distribution with some spread in the domain size distribution would have lower-frequency components which would propagate further in the z direction. The actual expected field is thus strongly model-dependent, primarily influenced by the average and standard deviation of the domain sizes: lacking a model that predicts these parameters, it is impossible to make strong predictions for the generated magnetic field.

It is important to note that there is no obvious *a priori* reason to expect chiral domains to be small. As noted by Matsumoto and Sigrist, domain walls are not energetically favorable: they are a non-equilibrium phenomenon stabilized only by pinning [Matsumoto and Sigrist, 1999], and it is not clear why the domain walls should be pinned on a small length scale in a clean crystal. The suggestion of a small domain size is at this point simply a possibility to consider in analyzing the data presented in this thesis, not a prediction based on any external data or theoretical predictions.

6.4 Conclusions and Outlook

I have studied Sr_2RuO_4 single crystals using scanning SQUID and Hall probe microscopy. The measurements strive to determine the local magnetic properties that would be characteristic of a TRSB wavefunction. At this point the measurements have not uncovered any sign of magnetic fields caused by spontaneous currents in Sr_2RuO_4. However, the currently available data is still not necessarily incompatible with TRSB: it is e.g. still possible that the fields generated are simply too localized to be detectable with our current probes. Nevertheless, the data presented in this thesis appears to be in direct contradiction with published estimates of the magnetic field that should be seen. This implies that both further theoretical and experimental investigation would be valuable.

It appears that the most promising geometry for further investigations of the possibility of TRSB in Sr_2RuO_4 involves crystal edges. An important focus for further theoretical work would be to clarify and make quantitative predictions for the magnetic fields at such edges: since holes may be significantly easier to work with experimentally (especially in terms of engineering the sample) it would be very useful to have predictions of the expected field profile, especially in the presence of domains of various

sizes.

In terms of experimental work, there appear to be two important avenues to improve the measurements: improving the spatial resolution and the optimizing the samples for maximum signal and ease of modeling.

Making measurements which truly probe the magnetic fields on the length scale set by the coherence length ξ would provide much stronger evidence on the subject of TRSB than the current measurements, since ξ sets a lower bound on sizes of chiral domains. This should be possible with new Hall probes with spatial resolution as fine as 100 nm, which are currently being tested.

On the sample side, the samples I have used for the measurements reported here had dimples as edges. It is significantly clearer and simpler to model the expected effects of through holes or outside edges of a crystal. Of these sample geometries, through holes are likely to be significantly easier to fabricate: a polished thin slice of crystal can be penetrated using FIB milling. In terms of measurements, using small grains or islands makes it more difficult to separate fringe effects of small environmental fields from spontaneous fields from the sample. Thus it appears that high-resolution imaging of a sample with through holes may be the best route forward to finally settle the issue of possible TRSB in Sr$_2$RuO$_4$ experimentally using scanning microscopy.

Chapter 7

Local Susceptibility of The 3K Phase of Sr_2RuO_4

In this chapter I discuss local SQUID susceptibility measurements on the "3 K phase" of Sr_2RuO_4, which contains inclusions of metallic Ru. This is a phase of the material in which there are signs of superconductivity already at around 3 K. This is one of the interesting properties of Sr_2RuO_4 beyond the possibility of a TRSB wavefunction; in fact at this point it is not clear if there is any relationship between the wavefunction symmetry and related properties and the apparently locally enhanced T_c in these samples with embedded metal grains.

I will first present a brief overview of what is known about the 3 K phase, and then continue with my observations and conclusions that can be drawn from them.

7.1 The 3 K Phase: Sr_2RuO_4 with Embedded Ruthenium

In certain samples of Sr_2RuO_4, the superconducting transition can be much broader than in the pure samples and reach up to 3 K. Because of this property, this material phase is often called the "3 K phase". The nature of this phase was first reported by Maeno *et al.* in 1998 [Maeno *et al.*, 1998], and it was found to be present in samples containing inclusions of pure metallic Ru. This commonly happens in parts of Sr_2RuO_4 crystals as a consequence of the growth process.

The higher T_c of the 3 K phase cannot be explained by the Ru inclusions going superconducting since bulk Ru is superconducting only below about 0.5 K. Maeno *et al.*

also report an anisotropy in H_{c2} that is consistent with superconductivity in the layered Sr_2RuO_4 structure, not in the relatively symmetric Ru grains [Maeno *et al.*, 1998]. Mao *et al.* have performed tunneling measurements and have observed signs of Andreev bound states which they interpret as a sign of localized non-*s*-wave superconductivity in the 3 K phase, which likely undergoes a phase transition close to the bulk Sr_2RuO_4 T_c into a phase which is similar to the bulk superconducting phase, leading to an essentially homogeneous superconductor below the bulk T_c [Mao *et al.*, 2001].

7.2   Experiments

I have studied a polished sample of the 3 K phase, prepared by Karl Nelson and Ying Liu at The Pennsylvania State University, down to temperatures well below the bulk Ru T_c. The sample we used had been studied earlier by John Kirtley in a scanning microscope in a ^{3}He refrigerator at temperatures down to slightly below 300 mK.

In our setup we could only perform measurements below the bulk Sr_2RuO_4 T_c, using 4K measurements as zero-level reference; the temperature stability of the refrigerator between 1.5 K and 4 K is too poor to do scanning microscopy. A series of scans at decreasing temperature is shown in Fig. 7.2.

In the upper part of the temperature range, between approximately 500 mK and 1.5 K, we found that the sample as expected had a fairly homogeneous diamagnetic susceptibility. Since the thickness of the Ru lamella, which appears to be on the order of 1 μm, is much smaller than the size of the field coil of the susceptometer SQUID, a weaker diamagnetic response from the inclusions than the bulk would likely not be detectable; only an enhancement compared to the bulk value should give a detectable signal. Thus, unless the superfluid density in the inclusions is higher than that of the bulk Sr_2RuO_4, this signal is expected to be completely dominated by the bulk Sr_2RuO_4 response. This matches our susceptibility images above 500 mK very well.

At temperatures below 500 mK, a striking inhomogeneity develops in the susceptibility response of the sample. The pattern of patches with enhanced diamagnetic response are within the range expected for the density of Ru inclusions seen in the sample using optical microscopy. Since the microscope has no coarse-motion capabilities and there is thus no way to determine the measurement area precisely, the spatially varying density of inclusions in the sample make it impossible to determine the expected
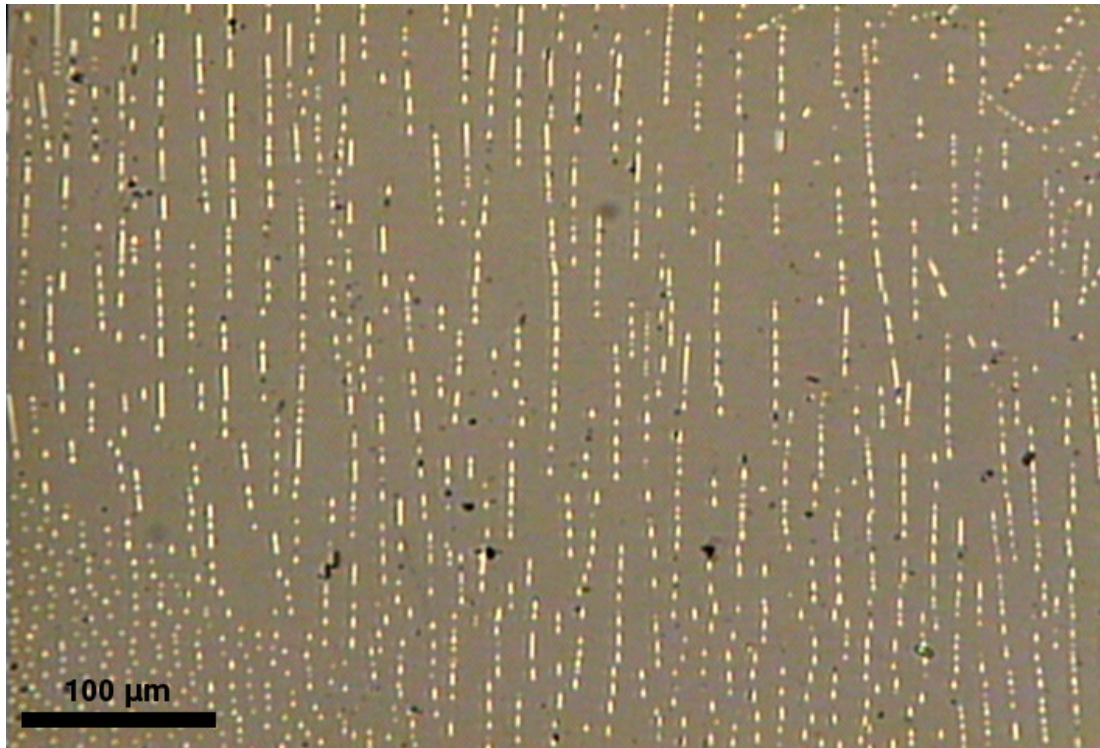
Figure 7.1: Micrograph of the 3K phase sample studied. The Ru inclusions in the sample are visible as bright spots. The inclusions are distributed unevenly in the sample. We attempted to scan an area where the inclusions could be seen individually with our scanning SQUID resolution.
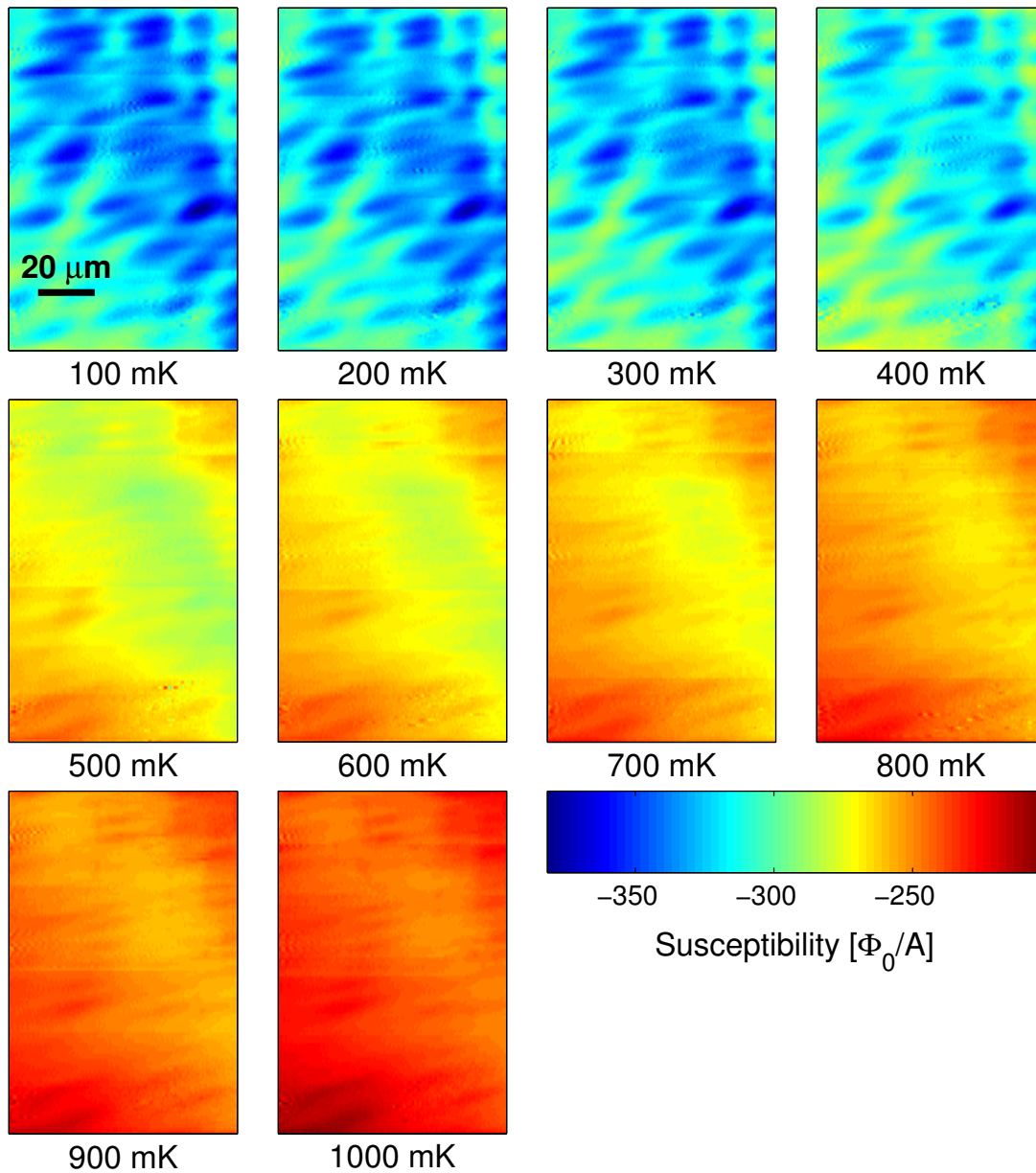
Figure 7.2: Scans of the 3K phase sample at temperatures up to 1K. The susceptibility is relatively uniform above the bulk Ru T_c, but becomes strikingly inhomogeneous below that temperature.

density of Ru inclusions in the scanned region. Nevertheless, from optical micrographs such as that shown in Fig. 7.1 typical distances between inclusions appear to be in the $10 - 30$ μm range. The centers of the areas with enhanced diamagnetic susceptibility in Fig. 7.2 generally fall within this range. Thus the most likely source of the enhanced inhomogeneous response is that the Ru inclusions develop superconductivity separately from the Sr_2RuO_4 matrix.

In order to investigate the temperature dependence of the susceptibility of the 3 K phase sample, we measured the susceptibility while slowly adjusting the temperature at two nearby points within the scan range, one at a response maximum and one at a minimum point. The data is summarized in Fig. 7.3. The enhanced response turns on at 0.47 K and the response increases smoothly in a fashion consistent with the superfluid density increasing with decreasing temperature. The response does strengthen even at the "low-response" point; however, this can be due to some pickup of signal from the inclusions even in the areas between them due to the limited spatial resolution of the SQUID probe.

7.3   Conclusions

One important conclusion of this experiment is that in order to study the intrinsic properties of Sr_2RuO_4 it is very important that the samples do not contain any Ru inclusions, since these inclusions appear to have properties that differ significantly from the bulk. Our measurements do not provide any direct information about the symmetry properties of the superconducting wavefunction in the inclusions; however, given that the temperature at which the enhanced diamagnetic susceptibility is seen matches the T_c of bulk Ru, a starting hypothesis could be that the inclusions behave just like bulk Ru, thus exhibiting s-wave superconductivity.

The measurements presented here do not affect any conclusions about the higher-temperature behavior of the phase; however, they do strengthen strengthen the hypothesis that the superconductivity above the bulk T_c of Sr_2RuO_4 is an effect that is caused by the Ru/Sr_2RuO_4 interface, not something that happens inside the Ru inclusions, and that this effect may not be related to the wavefunction symmetry inside the inclusions.

In the 3 K phase, I have demonstrated that there is a significant increase in the local diamagnetic susceptibility at temperatures below the T_c of metallic Ru. This

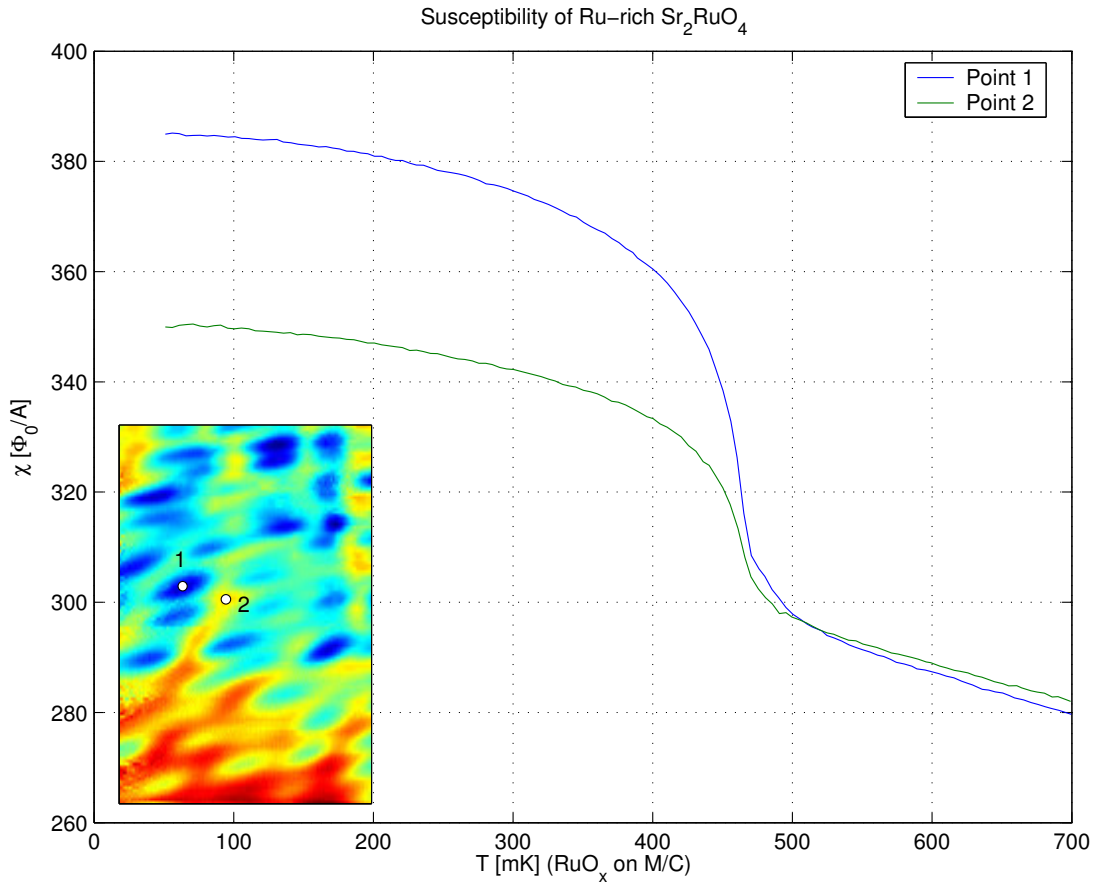Figure 7.3: Temperature dependence of the local susceptibility of a 3K phase. The blue curve corresponds to a pint with strong additional susceptibility response below 0.45 K (Point 1 in the inset figure), while the green curve is the response at a nearby low-response point (Point 2). Inset: Scan of the sample at 100 mK, where the Ru inclusions show up as areas with strong susceptibility response.

indicates that the inclusions either become superconducting at this temperature, or that the character of the superconductivity changes locally in the material, likely in the Ru inclusions.

Bibliography

P. W. Anderson. Knight shift in superconductors. *Phys. Rev. Lett.*, 3:325 – 326, 1959.

G. Binnig and H. Rohrer. Scanning tunnelling microscopy. *Helvetica Physica Acta*, 55 (6):726 – 735, 1982.

G. Binnig, C. F. Quate, and C. Gerber. Atomic force microscope. *Phys. Rev. Lett.*, 56: 930 – 933, 1986.

Per G. Björnsson, Brian W. Gardner, John R. Kirtley, and Kathryn A. Moler. Scanning superconducting quantum interference device microscope in a dilution refrigerator. *Rev. Sci. Instr.*, 72:4153 – 4158, 2001.

Per G. Björnsson, Martin E. Huber, and Kathryn A. Moler. A scanning squid microscope in a dilution refrigerator. *Physica B*, 329 – 333:1491 – 1492, 2003.

Per G. Björnsson, Yoshiteru Maeno, Martin E. Huber, and Kathryn A. Moler. Scanning magnetic imaging of Sr_2RuO_4. *Phys. Rev. B.*, 72:012504, 2005.

M. Büttiker, Y. Imry, and R. Landauer. Josephson behavior in small normal one-dimensional rings. *Phys. Lett.*, 96A:365 – 367, 1983.

B. Cabrera, R.M. Clarke, P. Colling, A.J. Miller, S. Nam, and R. W. Romani. Detection of single infrared, optical, and ultraviolet photons using superconducting transition edge sensors. *Applied Physics Letters*, 73:735 – 737, 1998.

V. Chandrasekhar, R. A. Webb, M. J. Brady, M. B. Ketchen, W. J. Gallagher, and A. Kleinsasser. Magnetic response of a single, isolated gold loop. *Phys. Rev. Lett.*, 67:3578 – 3581, 1991.

A. M. Chang, H. D. Hallen, L. Harriott, H. F. Hess, H. L. Kao, J. Kwo, R. E. Miller, R. Wolfe, J. Vanderziel, and T. Y. Chang. Scanning Hall probe microscopy. *Appl. Phys. Lett.*, 61:1974 – 1976, 1992.

K. Deguchi, Z. Q. Mao, H. Yaguchi, and Y. Maeno. Gap structure of the spin-triplet superconductor Sr_2RuO_4 determined from the field-orientation dependence of the specific heat. *Phys. Rev. Lett.*, 92:047002, 2004a.

K. Deguchi, Z.Q. Mao, and Y. Maeno. Determination of the superconducting gap structure in all bands of the spin-triplet superconductor Sr_2RuO_4. *Journ. Phys. Soc. Jpn.*, 73:1313 – 1323, 2004b.

V. O. Dolocan, C. Veauvy, Y. Liu, F. Servant, P. Lejay, D. Mailly, and K. Hasselbach. Observation of vortex coalescence in the anisotropic spin-triplet superconductor Sr_2RuO_4. cond-mat/0406195, 2004.

B.W. Gardner, J.C. Wynn, P.G. Björnsson, E.W.J. Straver, J.R. Kirtley, M.B. Ketchen, and K.A. Moler. Scanning superconducting quantum interference device susceptometry. *Review of Scientific Instruments*, 72:2361 – 2364, 2001.

P.E. Goa, H. Hauglin, M. Baziljevich, E. Il'yashenko, P. L. Gammel, and T. H. Johansen. Real-time magneto-optical imaging of vortices in superconducting $NbSe_2$. *Superconductor Science & Technology*, 14:729 – 731, 2001.

Janice Wynn Guikema. *Scanning Hall Probe Microscopy of Magnetic Vortices in Very Underdoped Yttrium-Barium-Copper-Oxide*. PhD thesis, Stanford university, 2004.

Hans-Ulrich Habermeier. Paing the way for the success of magneto-optics. In Tom H. Johansen and Daniel V. Shantsev, editors, *Magneto-Optical Imaging*, NATO Science Series, pages 1 – 10. Kluwer Academic Publishers, 2004.

K. Hasselbach, C. Veauvy, and D. Mailly. MicroSQUID magnetometry and magnetic imaging. *Physica C*, 332:140 –147, 2000.

Martin E. Huber, Bethel G. Abraham, Leonard J. Archuleta, Tommy Azua, Anthony J. Caravella, Son Duong, Sean T. Halloran, Erik A. Lucero, James T. B. Snodgrass, Per G. Björnsson, Brian W. Gardner, and Kathryn A. Moler. Well-shielded, high-symmetery scanning squid susceptometer. (in preparation.).

Martin E. Huber, Patricia A. Neil, Robert G. Benson, Deborah A. Burns, Alan M. Corey, Christopher S . Flynn, Yevgeniya Kitaygorodskaya, Omid Massihzadeh, John M. Martinis, and G. C. I-Iilton. DC SQUID series array amplifiers with 120 MHz bandwidth. *IEEE Trans. Appl. Supercond.*, 11:1251 – 1256, 2001.

Hypres, Inc. Design rules, As available online in June 2005. URL http://www.hypres.com/pages/download/designrules/rules.pdf.

K. Ishida, H. Mukuda, Y. Kitaoka, K. Asayama, Z. Q. Mao, Y. Mori, and Y. Maeno. Spin-triplet superconductivity in Sr_2RuO_4 identified by O-17 knight shift. *Nature*, 396:658 – 660, 1998.

K. Izawa, H. Takahashi, H. Yamaguchi, Yuji Matsuda, M. Suzuki, T. Sasaki, T. Fukase, Y. Yoshida, R. Settai, and Y. Onuki. Superconducting gap structure of spin-triplet superconductor Sr_2RuO_4 studied by thermal conductivity. *Phys. Rev. Lett.*, 86(12): 2653 – 2656, 2001.

John David Jackson. *Classical Electrodynamics*. John Wiley and Sons, Inc., third edition edition, 1999.

E. M. Q. Jariwala, P. Mohanty, M. B. Ketchen, and R. A. Webb. Diamagnetic persistent current in diffusive normal-metal rings. *Phys. Rev. Lett.*, 86:1594 – 1597, 2001.

Mark Johnson and John Clarke. Spin-polarized scanning tunneling microscope: Concept, design and preliminary results from a prototype operated in air. *J. Appl. Phys.*, 67:6141 – 6152, 1990.

B. D. Josephson. Possible new effects in superconductive tunneling. *Phys. Lett.*, 1:251 – 253, 1962.

P. G. Kealey, T. M. Riseman, E. M. Forgan, L. M. Galvin, A. P. Mackenzie, S. L. Lee, D. M. Paul, R. Cubitt, D. F. Agterberg, R. Heeb, Z. Q. Mao, and Y. Maeno. Reconstruction from small-angle neutron scattering measurements of the real space magnetic field distribution in the mixed state of Sr_2RuO_4. *Phys. Rev. Lett.*, 84(26): 6094 – 6097, 2000.

M. B. Ketchen and J. R. Kirtley. Design and performance aspects of pickup loop

structures for miniature squid magnetometry. *IEEE Trans. Appl. Supercond.*, 5:2133 – 2136, 1995.

M. B. Ketchen, D. D. Awschalom, W. J. Gallagher, A. W. Kleinsasser, R. L. Sandstrom, J. R. Rosen, and B. Bumble. Design, fabrication, and performance of integrated miniature squid susceptometers. *IEEE Trans. Mag.*, 25:1212 – 1215, 1989.

M. B. Ketchen, M. Bushan, S. B. Kaplan, and W. J. Gallagher. Low-noise dc SQUIDs fabricated in Nb-Al$_2$O$_3$-Nb trilayer technology. *IEEE Trans. Mag.*, 27:3005, 1991.

Mark B. Ketchen, T. Kopley, and H. Ling. Miniature squid susceptometer. *Appl. Phys. Lett.*, 44:1008, 1984.

J. R. Kirtley, M. B. Ketchen, C. C. Tsuei, J. Z. Sun, W. J. Gallagher, Lock See Yu-Jahnes, A. Gupta, and K. G. Stawiaszand S. J. Wind. Design and applications of a scanning squid microscope. *IBM Journal of Research and Development*, 39:655 – 668, 1995.

J. R. Kirtley, V. G. Kogan, J. R. Clem, and K. A. Moler. Magnetic field of an in-plane vortex outside a layered superconductor. *Phys. Rev. B*, 59:4343 – 4348, 1999.

H. J. Kwon, V. M. Yakovenko, and K. Sengupta. How to detect edge electron states in (tmtsf)(2)x and Sr$_2$RuO$_4$ experimentally. *Synthetic Metals*, 133:27 – 31, 2003.

L. P. Levy, G. Dolan, J. Dunsmuir, and H. Bouchiat. Magnetization of copper rings: Evidence for persistent currents. *Phys. Rev. Lett.*, 64:2074 – 2077, 1990.

G. M. Luke, Y. Fudamoto, K. M. Kojima, M. I. Larkin, J. Merrin, B. Nachumi, Y. J. Uemura, Y. Maeno, Z. Q. Mao, Y. Mori, H. Nakamura, and M. Sigrist. Time-reversal symmetry-breaking superconductivity in Sr$_2$RuO$_4$. *Nature*, 394:558 – 561, 1998.

A. P. Mackenzie and Y. Maeno. The superconductivity of Sr$_2$RuO$_4$ and the physics of spin-triplet pairing. *Rev. Mod. Phys.*, 75:657, 2003.

Y. Maeno, H. Hashimoto, K. Yoshida, S. Nishizaki, T. Fujita, J. G. Bednorz, and F. Lichtenberg. Superconductivity in a layered perovskite without copper. *Nature*, 372:532 – 534, 1994.

Y. Maeno, T. Ando, Y. Mori, E. Ohmichi, S. Ikeda, S. NishiZaki, and S. Nakatsuji. Enhancement of superconductivity of Sr_2RuO_4 to 3 k by embedded metallic microdomains. *Phys. Rev. Lett.*, 81:3765 – 3768, 1998.

D. Mailly, C. Chapelier, and A. Benoit. Experimental observation of persistent currents in a gaas-algaas single loop. *Phys. Rev. Lett.*, 70:2020 – 2023, 1993.

Z. Q. Mao, Y. Maeno, and H. Fukazawa. Crystal growth of Sr_2RuO_4. *Mater. Res. Bull.*, 35:1813, 2000.

Z. Q. Mao, K. D. Nelson, R. Jin, and Y. Liu. Observation of andreev surface bound states in the 3-k phase region of Sr_2RuO_4. *Phys. Rev. Lett.*, 87:037003, 2001.

Masashige Matsumoto and Manfred Sigrist. Quasiparticle states near the surface and the domain wall in a $p_x \pm ip_y$-wave superconductor. *Jornal of the Physical Society of Japan*, 68:994 – 1007, 1999.

K. D. Nelson, Z. Q. Mao, Y. Maeno, and Y. Liu. Odd-parity superconductivity in Sr_2RuO_4. *Science*, 306:1151 – 1154, 2004.

S. Nishizaki, Y. Maeno, and Z. Q. Mao. Effect of impurities on the specific heat of the spin-triplet superconductor Sr_2RuO_4. *J. Low Temp. Phys.*, 117:1581, 1999.

R. J. Noer and W. D. Knight. Nuclear magnetic resonance and relaxation in superconducting vanadium. *Rev. Mod. Phys.*, 36:177 – 185, 1964.

A. Oral, S. J. Bending, and M M. Henini. Real-time scanning Hall probe microscopy. *Appl. Phys. Lett.*, 69:1324 – 1326, 1996.

Bradley J. Roth, Nestor G. Sepulveda, and Jr. John P. Wickswo. Using a magnetometer to image a two-dimensional current distribution. *J. Appl. Phys.*, 65:361 – 372, 1989.

A. L. Schawlow. Structure of the intermediate state in superconductors. *Phys. Rev.*, 101:573 – 579, 1956.

J. Siegel, J. Witt, N. Venturi, and S. Field. Compact large-range cryogenic scanner. *Rev. Sci. Instr.*, 66:2520 – 2523, 1995.

Manfred Sigrist and Kazuo Ueda. Phenomenological theory of unconventional superconductivity. *Reviews of Modern Physics*, 63:239 – 308, 1991.

T. D. Stowe, K. Yasumura, T. W. Kenny, D. Botkin, K. Wago, and D. Rugar. Attonewton force detection using ultrathin silicon cantilevers. *Appl. Phys. Lett.*, 71:288 – 290, 1997.

Eric W J Straver. *Cantilever-based measurements on nanomagnets and superconductors.* PhD thesis, Stanford University, 2004.

T. Tamegai, K. Yamazaki, M. Tokunaga, Z. Mao, and Y. Maeno. Search for spontaneous magnetization in Sr_2RuO_4. *Physica C*, 388 – 389:499 – 500, 2003.

M. A. Tanatar, S. Nagai, Z. Q. Mao, Y. Maeno, and T. Ishiguro. Thermal conductivity of superconducting Sr_2RuO_4 in oriented magnetic fields. *Phys. Rev. B*, 63:064505, 2001a.

M. A. Tanatar, M. Suzuki, S. Nagai, Z. Q. Mao, Y. Maeno, and T. Ishiguro. Anisotropy of magnetothermal conductivity in Sr_2RuO_4. *Phys. Rev. Lett.*, 86(12):2649 – 2652, 2001b.

C. D. Tesche and J. Clarke. DC SQUID: noise and optimization. *Journal of Low Temperature Physics*, 29:301 – 331, 1977.

Michael Tinkham. *Introduction to Superconductivity.* McGraw-Hill, 2 edition, 1996.

A. Tonomura, H. Kasai, O. Kamimura, T. Matsuda, K. Harada, Y. Nakayama, J. Shimoyama, K. Kishio, T. Hanaguri, K. Kitazawa, M. Sasasek, and S. Okayasuk. Observation of individual vortices trapped along columnar defects in high-temperature superconductors. *Nature*, 412:620 – 622, 2001.

Akira Tonomura. Electron phase microscopy and its applications to the observation of vortex dynamics. *Jpn. J. Appl. Phys.*, 34:2951 – 2964, 1995.

M. J. Uren, D. J. Day, and M. J. Kirton. $1/f$ and random telegraph noise in silicon metal-oxide-semiconductor field-effect transistors. *Appl. Phys. Lett.*, 47:1195 – 1197, 1985.

Theodore Van Duzer and Charles W. Turner. *Principles of Superconductive Devices and Circuits.* Prentice Hall, 2 edition, 1998.

R. P. Welty and J. M. Martinis. A series array of dc squids. *IEEE Trans. Mag.*, 27: 2924 – 2926, 1991.